Proton and Pion Distributions from Au+Au Collisions at 10.8A GeV/c

A Dissertation Presented

by

Timothy William Piazza

to

The Graduate School

in Partial Fulfillment of the Requirements

for the Degree of

Doctor of Philosophy

in

Physics

State University of New York
at
Stony Brook

May 1997

Copyright © by
Timothy William Piazza
1997

State University of New York
at Stony Brook

The Graduate School

Timothy William Piazza

We, the dissertation committee for the above candidate for the Doctor of Philosophy degree, hereby recommend acceptance of the dissertation.

Thomas K. Hemmick
Professor of Physics

Robert McGrath
Professor of Physics

Madappa Prakash
Professor of Physics

Craig L. Woody
Physicist, Brookhaven National Laboratory

This dissertation is accepted by the Graduate School.

Graduate School

Abstract of the Dissertation

Proton and Pion Distributions from Au+Au Collisions at 10.8A GeV/c

by

Timothy William Piazza

Doctor of Philosophy

in

Physics

State University of New York at Stony Brook

1997

Measured inclusive double differential multiplicities $d^2N/dydm_t$ and related quantities for charged pions and protons in Au+Au collisions at 10.8 A·GeV/c are presented as a function of centrality. Systematic differences between the low p_t behavior of π^+ and π^- are examined in the light of baryonic decay. Pion spectral shapes are interpreted in light of the Δ feeding model resulting in the Δ to Nucleon ratio at freezout. Rapidity density of each particle specie is presented as a function of centrality. Proton rapidity spectra show an increased amount of stopping with respect to the lighter symmetric Si+Al system. Results are compared to the models RQMD

(version 2.3).

Friends are those into whose souls you've looked, and therein glimpsed a oneness with yourself. They are a part of you, and you are a part of them. They own a piece of you.

– The Harlan Ellison Hornbook, Installment#21,
the Los Angeles Free Press, 1973

I would like to dedicate this work to those in my life who have made it possible, to my family and to my wife; to my mother and my father Ruth and William, brother, sister, Jeff and Kim, sister-in-law Evie, uncles and aunts, Charlie and Clothilda, Ange and Hellen. But especially to my wife Tammy. She has sacrificed for this every bit as much as I have. I love you all dearly.

Contents

List of Figures

List of Tables

Acknowledgements

Now you are mine. *You* turned to the acknowledgments. You have no one to blame but yourself. This is the only part of this document where I can rant and rave to my heart's content. And I intend to do so. It's been a long five years, and I have a lot to get off my chest. I suppose that some of it has been bad, but I am afraid I am plagued by a horribly optimistic memory, and you'll be lucky to get a flavor of that here. Instead I hope to draw for you a pleasant picture, for this is the thing that I carry away with me. I realize that I'm really not that old but, with that caveat, I would like to say that this has been one of the better things that I have done in this life. I mean this, of course, in the most selfish of senses. I, personally, am better for it. I don't imagine that I have at all furthered the cause of mankind, perhaps this is something for the people that I leave behind. I'm not qualified to comment on the effect that I have had on the people around me, I hope that it has been positive. Indeed I am quite certain that I have been the cause of undo stress to my family and friends. So what is this document all about anyway? This is, quite simply, an attempt to justify the last five years of my life. This thesis will survive, perhaps, a few years as an interesting document regarding heavy ion physics

at moderate energy. The thing that I hope survives even longer is the memory of the lives that have touched me, and the lives that I have touched. In that light, this may be the most important part of this document...

The thank you's.

This is perhaps the most difficult part of this thesis. I have spent the last five years working on the rest of this document, this section I am much less prepared for. Let me start by saying that these pages are much too few, and my memory is much too poor to have included all those who deserve thanks. As for those deserving souls who are not mentioned here, I plead momentary exhaustion. You are no less appreciated, only momentarily neglected.

Thank you.

First and foremost I must thank my family. They have always given me something quite invaluable. Center. I know that with them I can always find my center. This is a non-trivial thing as the world gets bigger and badder, and they have never let me down. And perspective. It's easy to take oneself too seriously, especially when one devotes so much time and effort to a single goal. (While Jeff is around I know I'll never get too big for my own britches, he can always pull you right back down to earth, where you belong.) Thank you for the confidence and peace that came with the knowledge that there was always a warm and welcome door open for me, anytime. Thank you Mom, Dad, Jeff, Evie and Kim. To my extended family, the Kovels. Thank you for accepting me as a son. Tammy, you make the race worth running, thank you for the happiness you let me find in you.

You are all the most precious things that I have in this world.

Thank you.

To Stephen Johnson, I love to bust your balls, and also to discuss (sic argue) anything with you, be it physics, the nature of religion, consciousness, politics, or the human condition. You always have an interesting viewpoint, and even though you were *always* wrong (especially over politics), I enjoyed and grew from our discussions. Thongbay Vongpasueth, you often laughed at my stupid jokes. Thanks for humoring me. I will count your friendship as one of the treasures I take away with me from Stony Brook. Wen Chen Chang. What a guy. I have to say this fellow is perhaps the single nicest human being that I know. He has the patience of Job, an unending generosity with that most precious of commodities, his time, and all the enthusiasm of a Mexican jumping bean. And even though I am quite sure I do not deserve it, I am sure he has prayed for me. It is no exaggeration to say he has been at times an inspiration. Sergey Panitkin, you dry humored son-of-a-bitch, you made me roll on the ground during group meetings, and other inopportune times, on more than one occasion. And you always had some relevant insight. Thanks. Mark (got milk ?) Pollack, our time together was rather short, but I have profited from and enjoyed your friendship. On the computer you are Alpha Geek. Youngil Kwon, you are a man of great intellect and of equally great heart, I wish you peace and the best of luck in all of your endeavors. Rich Hutter, you're rough and gruff on the outside, and inside you are a big, soft, warm fuzzy. Thank you for remembering us at Christmas, it was a gesture that was always appreciated. And thank you for your behind the scenes efforts, they always made the difference. There are others...many others, I will list a few. Walt

Thernau, Dave Forsberg, Doug Tobias, Crissy Payne, Mike Pilato, Ling Chen, Robert Caputo, Socorro Delquaglio, Pat Peiliker Martin Trzaska , Johannes Wessels , Dariusz Miskowiec, Rich Bersch, Jimmy Dee, Vlad Pantuev, Robert Pisani, Sergey Sedykh, Bernd Surrow, Byungsik Hong, Yingchao Zhang, Nu Xu, and Chuan-Ming Zou. Also the the secretarial staff, Pat Peiliker, Soccorro Delquaglio, Diane Seagal, Francine Schultz, Elaine Larson, Pam Burris, and Penny Scholl, thank you. I have benefited from these people, both professionally and personally. I hope I have, in some small measure, given in like to them.

Thank you to all of the members of the E877 experiment. Experimental physics is a team sport, and it was my pleasure to be a part of this team.

I must thank Peter Braun-Munzinger and Johanna Stachel for their input and guidance. Their cumulative experience was a tremendous resource that was sorely missed after their departure. I have found them to be both to be patient teachers. And they throw a great after run party.

Thank you.

Now for the Big Guy. I met Dr. Hemmick at the end of my second semester here. He taught a mandatory graduate course, and he seduced me. It wasn't love at first sight, mind you. In academia I don't believe in such things. Any time a student has a new professor self preservation demands an attitude of caution; how much of a teacher is he(she), and how much of a ball buster is he(she)? Typically less of the former, and much more of the latter. And so it was with trepidation that I attended his mandatory office hour.

He immediately quit what he was doing, gave his full attention to me, and insisted that I call him Tom. We talked about my topic for a while and then, in closing, I offhandedly asked about his line of research. There were about 15 minutes left in my hour. Forty five minutes later he had given me a grand tour of high energy nuclear physics. With arms waving, hands gesticulating, he would go to the blackboard, then back to his desk, back to the blackboard and then back to his desk. He drew color ropes, phase diagrams, and potentials for mesons to climb out of. He would illustrate the pancaked (i.e. Lorenz contracted) Au nuclei as they collided, with the complete retinue of chiral symmetry restoration, mass shifts and the deconfined 'quark gluon plasma'. Every bit of it with sound effects, to boot.

This guy was serious. He wasn't just regurgitating his last grant proposal from rote. This guy was serious. No shit. I left that room grinnin' like a little kid. Here I was a second year physics grad student, and I have to be honest, I was approaching the end of my rope. The magic was quickly waning. The three previous semesters had served only to make physics a grind. In that short forty five minutes this man was able, through the sheer power of his enthusiasm, to rekindle the excitement, that magic that I had once known. It felt good, I felt that fire again. By the end of the semester I was on the experimental floor of Brookhaven National Lab testing a Ring Imaging Cherenkov (RICH) detector with Tom. It was the same excitement I had seen in his office, there in the trenches. Subsequently I asked Tom to be my advisor, and he accepted. A testament to *his* eternal optimism. He came to bat for me many times, and I came to bat for him when I could. In the years since our mutual decision there have been ups and downs, such is any relationship.

He is my first Ph.D. advisor, I am his first Ph.D. student. I know that what I have received from him is in no way proportional to the little which I have given. He is unique in that respect. From the bottom of my heart...

I thank *you* Tom Hemmick.

Chapter 1

Background

It is wrong to think that the task of physics is to find out how Nature is. Physics concerns what we can say about Nature.

–Niels Bohr

1.1 Introduction

Atom, from the Greek 'atomos' the indivisible, was once thought to be the ultimate constituent of matter. It is, perhaps, one of the great discoveries of this century that this is not the case. Indeed we have found something of an onion skin aspect to nature. The atom has given up its secret structure, it is composed of a small dense nucleus, surrounded by a cloud of electrons. At last, true constituents ... until the nucleus' structure was discovered, it is composed of protons and neutrons, and there is an apparent zoo of accompanying 'elementary' particles, the baryons and mesons. Have we finally glimpsed the heart of 'the matter'? No way. It has become apparent that the baryons and mesons are composed of even more basic constituents, the quarks. Quarks appear to be truly constituent (at least at scales of $\sim 10^{-16}$ (that is a decimal followed by 15 zeros and a one)) cm [1]. They are a rather social animal, always found in groups of two(mesons) or three(baryons). Observation of a free quark has never been verified in spite of many searches [37].

How have we come by this wealth of information regarding the microscopic? Much of it is the result of scattering experiments, whether it is Rutherford scattering from the charged nucleus, or deep inelastic scattering off partons in the nucleus.

1.1.1 The Approach

An interesting analogy regarding scattering experiments puts a fine Swiss watch in the hands of a physicist. Desiring to understand the inner workings of a Swiss watch the physicist proceeds to collide two such watches with each other. In the first such collision, out falls a spring. This spring is carefully cataloged. The physicist then begins a program of smashing Swiss watches into each other as often as he can. Each time he catalogues the nature and frequency of any piece that falls out, be it a gear, a spring, a hand, etc. It is a way to probe the guts of a Swiss watch. Within a finite number of collisions, every piece will have been liberated and examined at least once and now it is the job of the physicist to, with only his description of parts, uncover the dynamics of Swiss watch operation(the moral of the story is, of course, keep your fine Swiss watches out of the hands of physicists).

In the last few decades physicists have uncovered many of the 'constituent' building blocks of nature and have assembled a rather extensive understanding of their interactions.

1.1.2 Forces in Nature

All known interactions can be boiled down to four fundamental forces. In order of their strength they are:

- Strong force
- Electromagnetic force
- Weak force
- Gravitational force

All of the forces are mediated by some auxiliary particle. The strong force is responsible for holding nuclei together and is mediated by the gluon. Since the nucleus has a net positive charge it wants to fly apart, it doesn't and thats why it is a 'strong' force. Electromagnetism is that interaction between charges, its exchange particle is the photon. The weak force is responsible for some forms of radioactive decay and is mediated by the massive Z^0, W^+, and W^-. Gravity is that mutual attraction that any two bodies in the universe feel for each other and is thought to be mediated by the graviton.

Those are the interactions, the actual players are the elementary particles who interact via one or some of the four forces. One group of these particles are known by the name of leptons. Leptons, of apparent point size, do not interact via the strong force and have been found in six different types, whimsically

Name	Symbol	Charge	Bare Mass
down	d	$-\frac{1}{3}$	$7.5\ MeV/c^2$
up	u	$\frac{2}{3}$	$4.2\ MeV/c^2$
strange	s	$-\frac{1}{3}$	$150\ MeV/c^2$
charm	c	$\frac{2}{3}$	$1100\ MeV/c^2$
bottom	b	$-\frac{1}{3}$	$4200\ MeV/c^2$
top	t	$\frac{2}{3}$	$180000\ MeV/c^2$

Table 1.1: Properties of the quarks.

called flavors. Three of the leptons carry an identical electrical charge of -1, and in increasing mass are the electron, the muon, and the tau. The other three are the neutrinos and are electrically neutral. For each lepton there is, of course, a corresponding anti-lepton. Particle physics attributes all know hadron species to combinations of the next group of six particles, the quarks. Six distinct quarks, also known as flavors, have been identified to date. A review of some quark properties can be found in Table 1.1. Quarks carry a fraction of the electron charge. This cannot be the entire story, as quarks are, like leptons, particles of half integer spin and as such must obey the Pauliexclusion principle. The observation of baryons such as the Δ^{++}, which is composed of *uuu* and has a spin of 3/2, require the introduction of yet another degree of freedom, other than spin and charge, fancifully called color. It is on color charge that the strong force acts (thus the strong forces' proper name, quantum chromodynamics, QCD). Each flavor of quark (and gluon) can carry one of three kinds of color, red, green or blue subject to the condition that hadrons are always white or color neutral. This condition, experimentally confirmed to date, is known as confinement and is consistent with the fact that a bare quark has never been seen in isolation. Most of this story comes directly from lepton-lepton, lepton-proton, and proton/antiproton-proton scattering.

The casual reader may ask 'why is heavy ion physics an interesting endeavor to pursue?' Ultimately the quest is for new and interesting physics, in this case the essential question being asked: is the collision of a nucleon traveling *with* other nucleons in a nucleus-nucleus collision different in anyway from the collision of a bare nucleon with another nucleon or nucleus [4]? If there are differences, can they be explained based upon know properties of hadron-hadron collisions? Indeed the realm of binary high energy hadron collisions has been explored for decades, and the the center of mass energies probed there are routinely orders of magnitude higher than those that interest this analysis. Clearly, what we are *not* exploring is the high energy frontier of hadron collisions. Instead it is another frontier which we wish to explore, we wish to push the high density high entropy envelope. It is the creation of super dense and hot nuclear matter over large volumes and long times that drives this program. Can matter, so called Quark Matter, in which the quark degrees of freedom are important be created and studied in the laboratory ? Nuclear matter, under conditions of extreme temperature and density, may undergo a phase transition out of normal hadronic nuclear matter and into a 'deconfined' phase in which quarks would no longer be confined to individual hadrons. In this phase, the so called *Quark-Gluon Plasma*, quarks would be free to move over an extended volume [5, 6, 8, 7].

Experimentally, the high energy heavy ion collision program is rather young; starting in 1986 with the acceleration of oxygen and silicon to 14.6 $A \cdot GeV/c$ at the AGS, and oxygen and sulfur to 60 and 200 $A \cdot GeV/c$ at the CERN SPS. With p-A collisions these systems provided important information regarding the evolution of hadron collisions from p-p to A-A [2, 3, 9], but the highest achievable energy and baryon densities would await acceleration of the first truly heavy ions. This would come in short order, a testament to the excitement generated by this new field, in 1992 when the BNL-AGS accelerated Au ions to 11.7 $A \cdot GeV/c$. Model predictions indicated that baryon densities between 7-9$\cdot\rho_0$ [10] could be achieved in these reactions. At the AGS, where the production of nucleon/anti-nucleon pairs is small [11, 12], an accessible probe of the realized densities is the amount of stopping, as measured in the proton distributions, achieved in these collisions. In the reaction Si+Al [16, 34, 35, 38] there was observed strong evidence of large in medium nuclear cross sections, and that participants undergo several collisions. A review of the results for the lighter system can be instructive.

1.2 Si + Al

Data from heavy ion collisions at slightly higher energy, but much smaller projectile mass has been extensively analyzed [35, 50, 14]. In experiment E814, for Si+Al as well as the Si+Pb system, it was seen that within statistics the proton transverse mass spectra were well described by both Boltzmann and m_t exponential parameterizations. Near beam rapidity and $m_t = 0$, for Si+Al, a steep component in the m_t spectrum was observed. This component was associated with "punch through" protons [35, 38] which interact at most elastically with the target nucleons. Values of the slope parameter T_B, as a function of rapidity, showed a mild centrality dependence for Si+Pb, increasing with higher centrality well after full overlap of projectile and target. The slope parameter was observed to increase systematically with the mass of the ejectile, implying emission from a transversely expanding system [46, 47, 48]. A hydrodynamical picture is characterized by a particle flow, *i.e.* superimposed upon their thermal motion all particles move with a constant velocity component. This fact means that any particle's kinetic energy will be proportional to that species' mass, and as the temperature parameter is a measure of a particle's kinetic energy it will sample both the thermal and any collective components. An independent measure of the system temperature was obtained via the population of the nucleon resonances [39, 40] and was found to be $T = 140 \pm 20 MeV$. With the temperature no longer a free parameter the mass dependence of the slope parameter can be described by an average transverse expansion velocity of $0.33 - 0.39c$ [49]. It should be noted that an isotropic

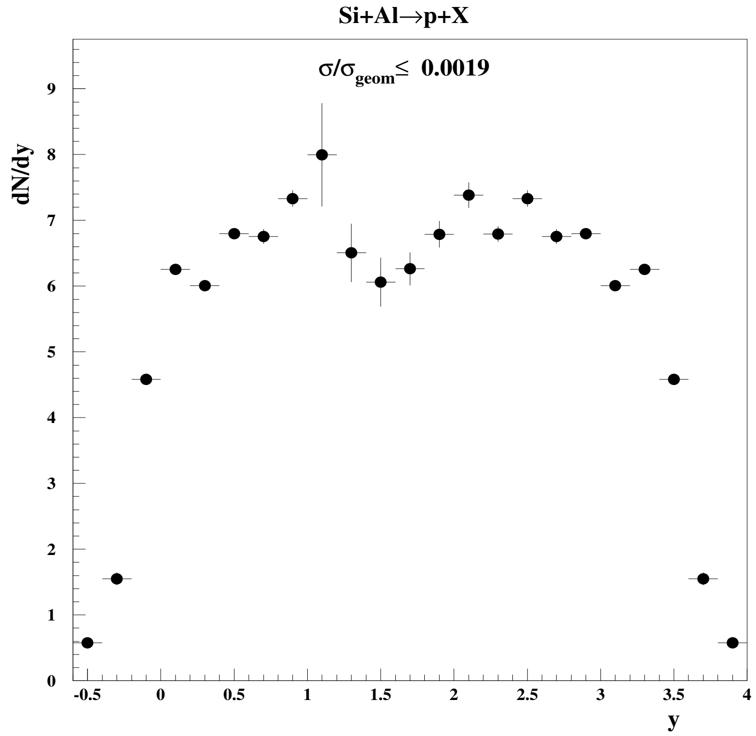

Figure 1.1: Rapidity density of protons for Si+Al at a centrality of $\sigma/\sigma_{geom} = 0.0019$.

---

thermal model fit to the proton slopes yield a temperature $T \approx 225 MeV$ in variance with data on nucleon resonance populations and the slopes of pion transverse momentum spectra [40, 50].

Construction of rapidity density, dN/dy, was accomplished by integrating measured proton spectra where available, and extracting Boltzmann slope parameters for extrapolation elsewhere. The E814 acceptance allowed for the measurement of the intercept of the spectra past mid rapidity. In that analysis no statistically significant difference was found to exist between a Boltzmann or an m_t exponential fit. From the region where there was sufficient transverse coverage to measure a slope, the slope around mid rapidity was extrapolated and used, in conjunction with the measured amplitude, to estimate dN/dy. For the most central Si+Al collisions, corresponding to $\sigma/\sigma_{geom} = 0.19\%$, the rapidity spectrum is flat over three units of rapidity,fig 1.1, and shows no sign of a beam rapidity peak. These observations indicate no significant transparency in this symmetric system. The large width of the proton rapidity distribution could indicate significant longitudinal expansion, and indeed the distribution is well reproduced by a source expanding longitudinally with a mean velocity of $\approx 0.52c$ [49].

The advent of Au beam at the BNL-AGS, starting in the fall of 1992, at last made it possible to probe the highest baryon densities perhaps accessible in the laboratory. This thesis concerns the analysis of Au beam data, collected in the fall of 1993 by the E877 experiment, with particular emphasis on the proton and pion distributions resulting from these collisions.

Chapter 2

The Apparatus

Experiment E877 is designed to study collisions of large nuclei at energies which we hope will briefly produce the extremely high temperatures and densities necessary for phase transition of condensed hadronic matter into Quark-Gluon Plasma. For the experiment discussed here, we have analyzed central collisions of Au ion projectiles at 10.8 A·GeV/c momentum on various nuclear targets. The following is a brief introduction to the accelerator facility and the detector systems that constitute E877.

2.1 Accelerator Complex

The data presented were collected by experiment E877 at the Alternating Gradient Synchrotron (AGS) at Brookhaven National Laboratory (BNL) in the fall of 1993 . The heavy ion facility is composed of the tandem accelerator, the heavy-ion transfer line (HITL), the AGS Booster, and finally the AGS itself. A high intensity negative heavy ion beam is produced at the Tandem

Accelerator Facility by a Middleton style 'Widow-Maker' ion source which is located inside the terminal (high voltage center) of the first of two tandem accelerators. Inside the ion source, a beam of positive cesium ions are focused onto an Au sputter target by a potential of 25 kV.Negative Au ions leave the target and are extracted through the same 25 kV potential. These are subsequently repelled by the negative potential of the terminal itself and to ground at the exit of the first tandem. The beam enters the second tandem and accelerates toward the positive high voltage terminal of this machine. While traversing the terminal, the negative ions pass through a thin carbon foil which strips them to a positive charge state. They are subsequently repelled by the positive terminal toward the exit of the second tandem, and fed into the HITL.. At this stage of acceleration the Au ions have a kinetic energy of 1.2 $A \cdot$ MeV. The Au ions are subsequently transported by the HITL to the AGS Booster, where they are accelerated to an energy of $\sim$ 200A$\cdot$ MeV. At the end of this acceleration the Au beam passes through one final foil to obtain complete stripping and is then injected into the AGS (Fig. 2.1)where it is accelerated to a final momentum of 11.1 A$\cdot$ GeV/c. Beam is slow extracted and transported (with some degradation in energy) to experiment E877 via beam line C5. Beam on target was typically $\sim 10^4$ particles per spill. The AGS had a repetition rate of 3.6 sec and a spill duration of one second [22, 23].

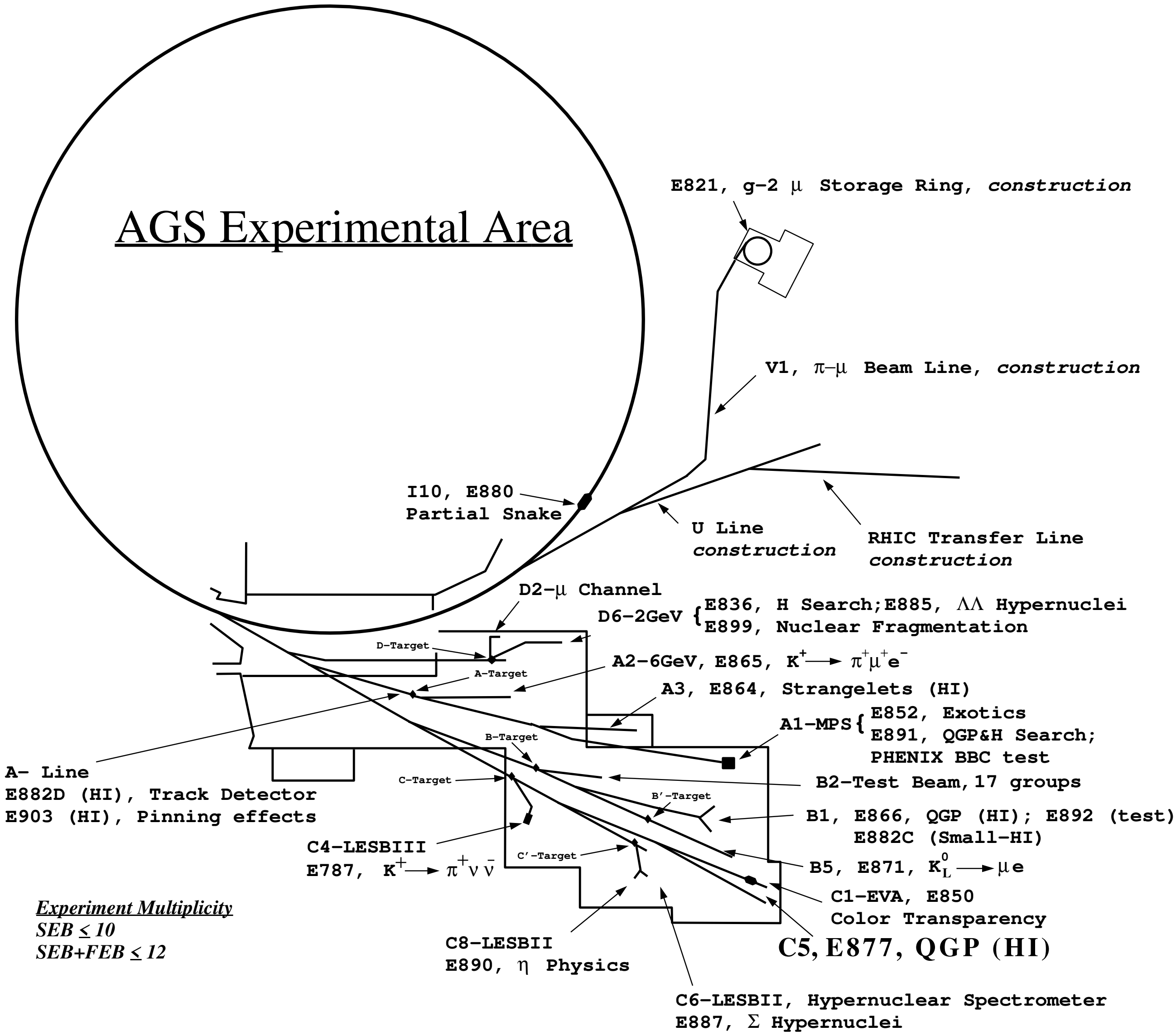

Figure 2.1: Layout of the Alternating Gradient Synchrotron experimental area for the fall 1993 heavy ion run.

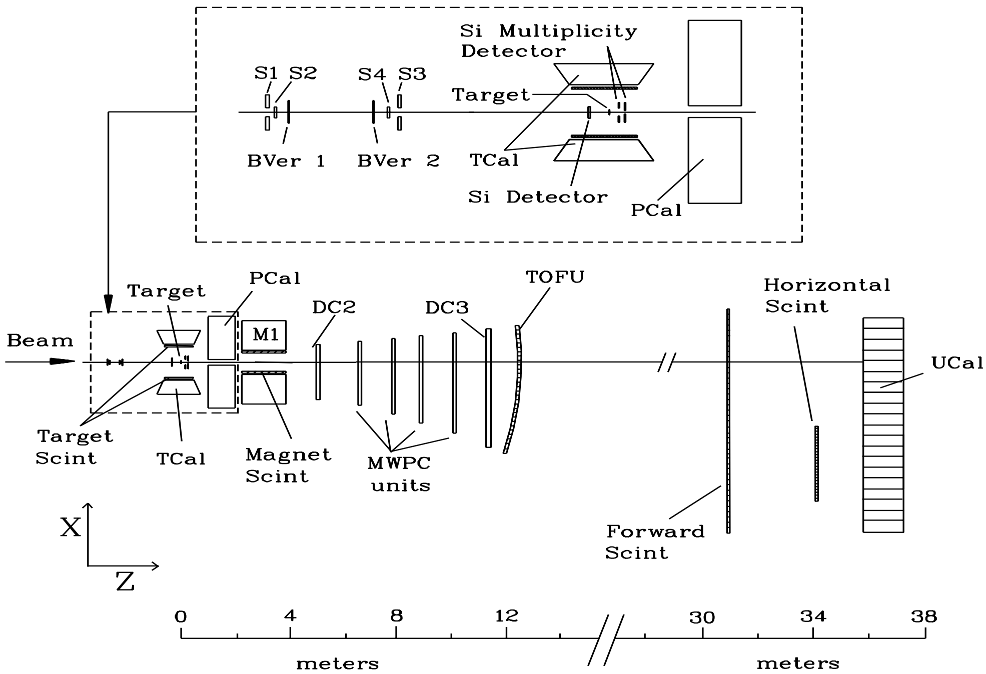

Figure 2.2: The E877 experimental configuration for the fall 1993 heavy ion Au run. The experiment is characterized by 1) beam definition devices; 2) detectors for event characterization; 3) forward spectrometer. Au beam is incident from the left.

2.2 The E877 Experiment

The following sections give a brief description of the apparatus of the E877 experiment which is shown in figure 2.2. The experiment consists of three independent major components. The beam definition section is used to measure the characteristics of each beam particle prior to interaction. The event characterization section measures the integrated energy and charged particle production of each collision with very large acceptance. The forward spectrometer determines the identity and measures the vector momentum of charged particles within a limited aperture surrounding the incident beam direction. Throughout the discussion we employ a right handed coordinate system whose origin is located at the nominal point of intersection of the beam and target, whose z axis is oriented along the nominal incident beam direction, and whose y axis is vertically upward.

2.2.1 Beam Definition

Although the beam that is extracted from the AGS is quite pure (improper charge states, energies, or massed will not form a stable orbit in the ring), some impurities may be introduced during the transport of the beam from the extraction point to the target by interaction of the beam particles during said transport. Although the beam line optics act to a large degree as a filter to reject such contamination, it is still necessary to verify the beam species (Z,A) and momentum (trajectory) prior to collision with the target. Such selections are made coarsely as part of the trigger definition and at a fine level in the offline analysis. Finally, since the spectrometer uses a velocity based particle identification, the time of the interaction must be precisely measured. Several detector systems participate in the beam definition and are described below.

Beam Scintillators(BSCI): Since the C5 beam line is in essence a spectrometer for magnetic rigidity (p/Z), some contamination can be identified and eliminated by selecting only those particles with a particular trajectory. At lower energies, collimation by absorber can be used to effectively limit the trajectories of beam particles on target. Here, such devices would simply provide a new source of background. Rather that preventing particles with improper trajectories (momenta) from reaching the target, we simply choose to record only those interactions induced by beam particles with proper trajectories. The set of four thin "Beam Scintillator" counters labeled S1,S2,S3,S4, in figure 2.2 serve to loosely define the incident beam trajectory. Particles with proper trajectories strike both S2 and S4, and pass through the central holes in S1 and S3. "Good beam" is thus defined as $\overline{S1} \cdot S2 \cdot \overline{S3} \cdot S4$ and is required for an event to be recorded to magnetic tape. The holes in S1 and S3 are slightly smaller that the areas covered by S2 and S4 to eliminate "cracks" in the beam definition. Fast rise time photo tubes are used on S4 so that this counter additionally provides a high precision ($\sigma = 40psec$) measurement of the interaction time [13].

Beam Vertex Detector(BVer): Although the BSCI detectors provide sufficient beam trajectory selection at the trigger level, a much higher precision is required in the offline analysis. For this measurement we use a pair of Si microstrip detectors located between S2 and S4. Each of these detectors measures the beams x-location to an accuracy of 50 μm (the pitch of the strips). The effective resolution of the system is limited by multiple scattering in the detectors themselves (300 μm) to 40 μrad in the incident beam angle [14] and 300 μm in the x coordinate of the beam at the target. These detectors also eliminate events in which two particles strike the target simultaneously.

Upstream Silicon (SILI): The nuclear charge (Z) of the projectile is measured by a thin Si detector placed just upstream of the target. This detector has unit charge resolution (much higher than the BSCI) at Z=79 and is used to eliminate projectiles which have lost a proton (most likely due to Coulomb excitation during beam transport).

The detectors described above define the charge, momentum, and time of each incident beam particle. No detector system verifies the mass(A) of the projectile. However, since the measurement shows that the Z<79 contamination is less than one percent, we can safely assume that the A<197 contamination remaining after cuts is of a similarly low level.

2.2.2 Event Characterization Detectors

Full overlap (b=0) collisions have the largest number of participating nucleons, largest interaction volume, greatest probability of secondary re-interactions, probably provide the highest energy density, and are the subject of this thesis. However, it is impossible to direct the projectile with sufficient precision so as to select the impact parameter on an event by event basis. Fortunately, a variety of final state observables are correlated with the impact parameter and thereby allow a limited precision impact parameter determination ex post facto. One such variable is the transverse energy, E_t. It is certainly true that total energy leaving the collision zone is the same in every event, even non-overlap collisions. In the latter case all energy is directed along the incident beam direction. The transverse energy parameter is formed by summing the energies of all ejectiles weighted with the polar angle of their emission as:

$$E_t = \sum_{allparticles} E_i \sin\theta_i \tag{2.1}$$

E_t is in essence a "poor man's p_t". Naively one would expect that the conversion of energy directed along the beam axis to that perpendicular to the beam axis would be correlated with impact parameter. Indeed, as shown in figure 2.3, a not so naive cascade model such as RQMD(version 2.2) predicts a narrow correlation between impact parameter (b) and transverse energy (E_t). Several detectors in E877 measure "global variables" such as E_t and are used for the selection of central collisions.

<u>Target Calorimeter(TCal):</u> Calorimetric measurement of E_t in the backward direction is accomplished by the TCal. The TCal consists of four walls of electromagnetic calorimetry which surround the target completely in the azimuthal direction and cover polar angles in the range $48^o < \theta < 135^o$ corresponding to a pseudorapidity coverage of $-0.5 < \eta < 0.8$. The device is composed of 832 NaI scintillating crystals, arranged in a projective geometry with 16 azimuthal and 13 polar segments. Each crystal is only six radiation lengths deep, and thus contains only a fraction of the energy directed toward it. A more detailed description of the device can be found in reference [15].

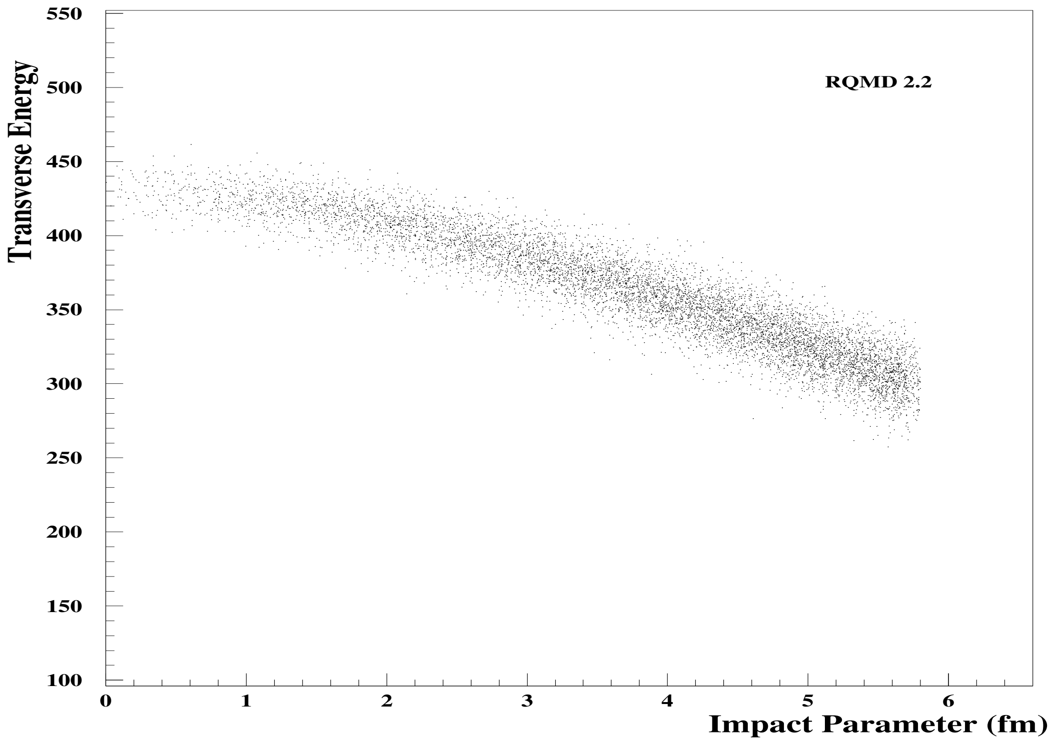

Figure 2.3: The dependence of produced transverse energy, E_t, upon impact parameter in the cascade model RQMD version 2.2.

Participant Calorimeter(PCal): Calorimetry in the forward direction is effected by the PCal. PCal is a lead/iron/scintillator sampling calorimeter which is four interaction lengths deep. It is segmented into 16 azimuthal, 8 polar and four depth segments. It covers polar angles in the range $1^o < \theta < 47^o$ corresponding to $0.83 < \eta < 4.7$. Although it has considerably fewer segments than the TCal, the PCal serves as the primary centrality detector thanks to it's larger pseudorapidity coverage (which includes mid-pseudorapidity) and better shower containment [19, 20].

Employing both the TCal and the PCal, the E877 experiment can perform exceptional global event characterization. Both our centrality tag and determination of the azimuthal orientation of the reaction plane are derived from the transverse energy measurements made with this calorimetry. Experimentally transverse energy is defined as

$$E_t = \sum_{allcells} E_\nu \sin\theta_\nu \tag{2.2}$$

where the sum is performed over all calorimeter cells, not all ejecta. Here the angles θ_ν locate the center of each tower rather than the locus of each particles trajectory.

Centrality can be determined by taking a simple geometric model. Neglecting fluctuations one can obtain the impact parameter for each event via

$$\pi b^2 = \sigma_{overlap} = \int_{E_t}^{\infty} \frac{d\sigma}{dE_t'} dE_t' \tag{2.3}$$

with

$$\frac{d\sigma}{dE_t} = \frac{s}{n_t \cdot B} \frac{dN}{dE_t} \tag{2.4}$$

where s is the down-scaling factor for this trigger, n_t is the number of target atoms per unit cross sectional area, and B is the number of incident beam particles. These relations yields impact parameter b as a function of E_t. A detailed discussion on the effects of fluctuations on this correlation can be found in [21]. Although this approach is useful for providing an intuitive grasp of the collision overlap, it is not necessarily correct. For this reason, all centrality definitions will be defined by the fraction of the $d\sigma/dE_t$ they represent than by the impact parameter.

An additional parameter which is of interest in characterizing the collision geometry is the orientation of the reaction plane(the plane which contains both the projectile velocity vector and the vector connecting the target and projectile). The reaction plane can be determined event by event by performing a Fourier analysis on the transverse energy deposited in a fixed pseudorapidity window [21]. The Fourier coefficients of the expansion are given by

$$a_n = \frac{\sum_\nu \epsilon_\nu cos(n\phi_\nu)}{\sum_\nu \epsilon_\nu}, \qquad b_n = \frac{\sum_\nu \epsilon_\nu sin(n\phi_\nu)}{\sum_\nu \epsilon_\nu} \tag{2.5}$$

where ϕ_ν is the azimuthal angle of the detector cell. The n=1 Fourier coefficients hold the information regarding the azimuthal orientation of the energy flow in the collision. We measure the azimuthal angle of the reaction plane as

$$\psi_{reac} = tan^{-1}\left(\frac{b_1}{a_1}\right) \tag{2.6}$$

Although we will endeavor to make a complete analysis of charged particle spectra with respect to event centrality, a detailed analysis of particle spectra with respect to reaction plane is outside the scope of this thesis.

Multiplicity Detector(Mult): In addition to transverse energy, charge particle multiplicity in the final state is a useful measure of collision violence, and/or centrality. Just downstream of the target is located the silicon multiplicity detector. The multiplicity detector consists of two identical silicon disks. Each disk is segmented into eight concentric rings of 64 pads each (1024 channels). These disks and their segmentation were designed and optimized for Si + Pb collisions. There, a single pad had a less than 10% chance of being struck by a charged particle. Thus, the device was readout by a simple descriminator circuit as a "hit pattern". For central Au+Au collision the multiplicity leads to an occupancy higher than 50% in many pads. For this reason, the detectors were outfitted with new readout electronics which would record the energy deposit to aid in distinguishing hits with multiple particles in a single pad. Although the energy deposit measurement was able to determine, with high precision, the mean number of charged particles into each pad for any class of collisions, it did not have sufficient resolution to uniquely determine multiplicity on an event by event basis, and was thus not used in this analysis [16, 17].

2.2.3 Forward Spectrometer

Although the E877 calorimetry provides precision measurements of energy flow over a large solid angle, it does not measure the characteristics of individual particles. In our calorimeters several particles hit each cell and each single particle showers energy over several cells. Additionally, the array is incapable of identifying the specie of the particles which deposit the energy. Such measurements are the task of the E877 forward spectrometer. The spectrometer uses a combination of magnetic analysis and velocity measurement to uniquely identify individual particle species and determine their vector momentum. As its measurements are more detailed, its instrumentation is more varied and its acceptance is smaller than the calorimeter array.

The principle of operation of a magnetic spectrometer is that when a particle of mass m and charge Ze moves in a uniform static magnetic field $\vec{B}$, with momentum $\vec{p}$, the equations of motion are [18]:

$$\frac{d\vec{p}}{dt} = Ze\vec{\beta} \times \vec{B}, \qquad \frac{dE}{dt} = 0 \tag{2.7}$$

where $\vec{\beta}$ is the particle's velocity, and E is the particles energy. Since the energy is a constant of motion, the magnitude of the velocity, and thus $\gamma = 1/\sqrt{1-\beta^2}$, is also a constant. The first part of Equation 2.7 can be written as:

$$\frac{d\vec{\beta}}{dt} = \vec{\beta} \times \vec{\omega}, \qquad \vec{\omega} = \frac{e\vec{B}}{\gamma m} \tag{2.8}$$

The motion described by Eq. 2.8 has two components, one circular in the plane perpendicular to $\vec{B}$ and one of uniform translation parallel to $\vec{B}$. The solution for the velocity is:

$$\vec{v}(t) = v_{||}\hat{\epsilon}_3 + \omega a(\cos(wt)\hat{\epsilon}_1 - \sin(wt)\hat{\epsilon}_{2)} \tag{2.9}$$

with $\hat{\epsilon}_3$ a unit vector parallel to the field and $\hat{\epsilon}_1$ and $\hat{\epsilon}_2$ the unit vectors perpendicular to the field, and a is the radius of gyration . From Eq. 2.8 and 2.9 we find that

$$p_\perp = ZeBa \tag{2.10}$$

or in more convenient units

$$p_{\perp}(MeV/c) = 3.00 \times 10^{-4} ZBa(gauss - cm) \tag{2.11}$$

Thus a detailed measurement of a particles trajectory in a known magnetic field, as well as knowledge of its charge state, is sufficient to identify its vector momentum and charge sign. More detail of the momentum measurement is given in section 4.3.

Particle species are identified via a reconstruction of a particles mass. This is accomplished by coupling the momentum measurement with a measurement of velocity and using the relation:

$$|\vec{p}| = m\gamma \left|\vec{\beta}\right| \Rightarrow m = \frac{|\vec{p}|}{\left|\vec{\beta}\right|}\sqrt{1 - \left|\vec{\beta}\right|^2} \tag{2.12}$$

Shown in figure 2.4 is the E877 event display which highlights the forward spectrometer. Those charged particles which pass through a small collimator (inserted into the PCal) pass through a dipole magnetic field. Following this field, they intersect six tracking detectors (DC2, MWPC1, MWPC2, MWPC3, MWPC4, DC3) which record the position of the particles prior to passing through the Upstream Time-Of-Flight wall (TOFU) which records their time of passage. Each of these systems is discussed below.

Collimator: I have commented that an absorption collimator is inappropriate for defining beam trajectory since it provides a source of background. The same is not true for selecting reaction product trajectories. The interior walls of a magnet aperture will always act as a production source of secondary particles. Since secondaries are always lower in energy than their parents, they

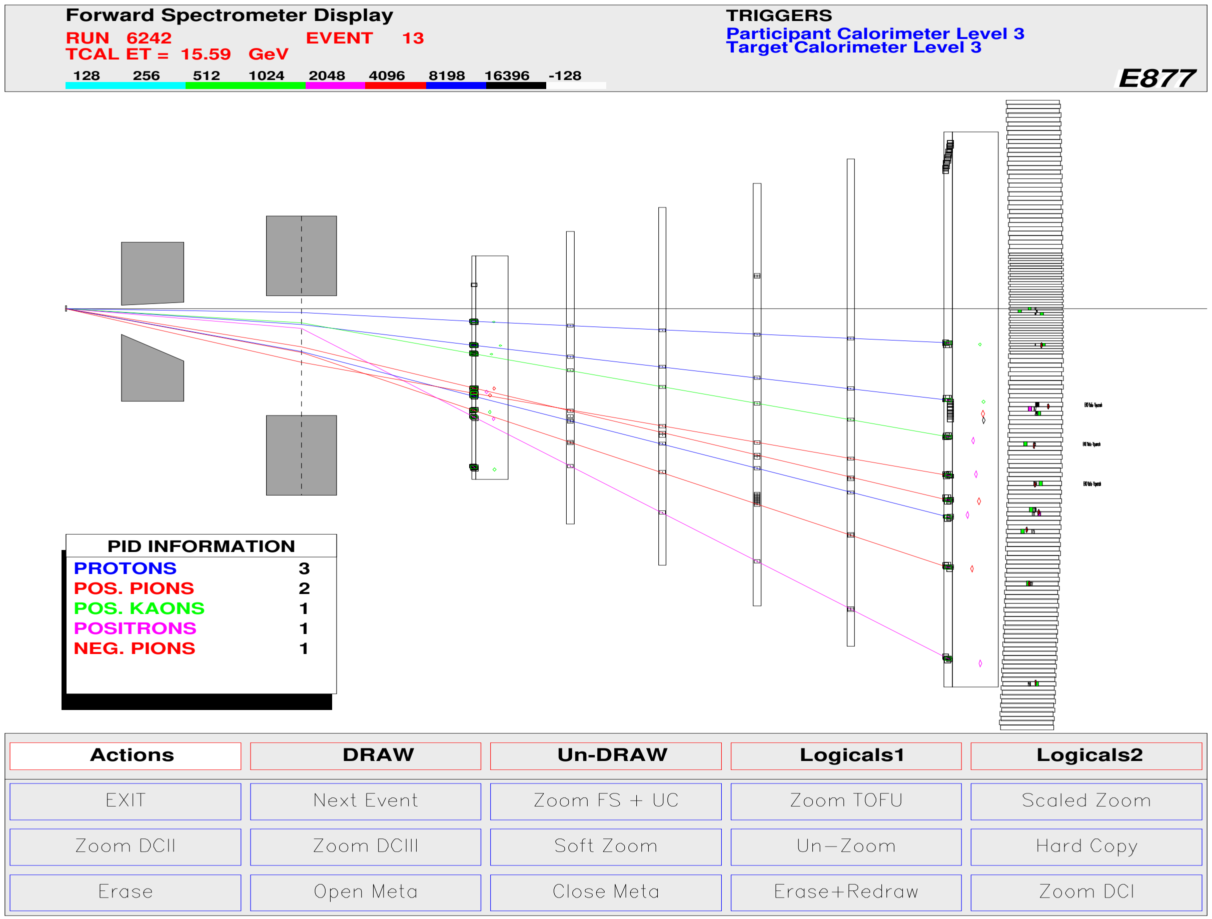

Figure 2.4: Event display for a typical Au+Au collision.

often cannot escape the magnetic field. However secondaries produced near the exit aperture of the magnet will usually escape. The use of a collimator forces all secondaries to be produced prior to the field and thus results in the least possible background in the spectrometer itself.

The opening of the collimator is set to be smaller than the projective opening of the magnet aperture and has an angular acceptance (view from the nominal collision point) of $-134 < \theta_x < 16$ mrad and $-11 < \theta_y < 1$ mrad in the lab frame.

Analyzing Magnet: At the AGS dipole magnet field polarities are specified as either A or B, with A fields bending positive a beam in the same sense as the AGS rotation(+x in the E877 spectrometer). The field in the analyzing magnet was run in *both* A and B polarities with an $\int B \cdot dl = 0.2739 T \cdot m$.

Drift Chamber(DRCH): The two drift chambers DC2 and DC3, which bracket the set of tracking detectors, provide the precision measurement of particle trajectories. Each chamber is a hybrid drift and pad detector. Multiple thin ($18\mu m$ diameter) anode wires are strung vertically in each chamber. The view from above, of a single wire cell, is shown in figure 2.5. The anode wires are run at ground potential and dc coupled into the preamplifier. The electric field is imposed by conducting planes (aluminized mylar foils) upstream and downstream of each wire and by "field wires" placed between the anodes. The foils and field wires are run at high voltage negative. Each wire is instrumented with a fast amplifier (10 nsec rise time), descriminator, and TDC which measures the time of arrival of an avalanche with two nanosecond resolution.

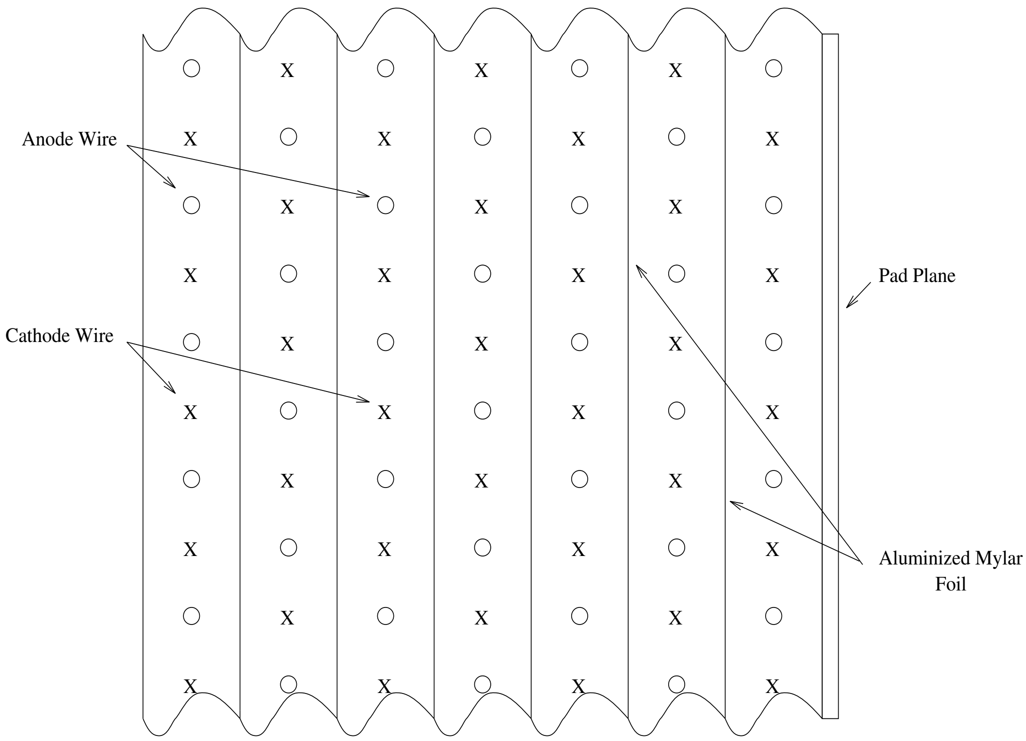

Figure 2.5: Physical layout of drift chamber and pad plane.

Following the passage of a charged particle, an ionization trail drifts toward, and avalanches at, the anode wire. The time of arrival of the avalanche is proportional to the distance between the anode wire and the primary track and yields a position resolution of roughly $300\mu m$. Each chamber contains six drift planes in sequence with anode wires arranged in a "staggered" geometry, fig. 2.5. This staggered pattern is necessary to resolve the left-right ambiguity(whether a particle was located to the left or right of a given anode wire) and provides enough redundancy that the drift chambers are essentially 100 % efficient.

The seventh plane of wires, in each chamber, is arranged similarly to each of the drift planes. However, in this case, the anode wires are run at high voltage positive, while the field wires and cathode planes are run at ground potential. Although the front cathode plane is an ordinary sheet of aluminized mylar, the back plane is made from a thin printed circuit card segmented into a series of chevron-shaped pads running along the anode wires. The relative image charge deposited on a pair of neighboring pads is used to measure the location of a particle track along the anode wire. Typical resolution of this technique is a few percent of the pad size, yielding 2.3-15 mm in DC2 and 4.3-36 mm in DC3, depending upon the pad size.

A more comprehensive description of the construction and characteristic features of the DRCH system can be found in [27, 28, 29].

<u>Multiwire Proportional Chamber(MWPC):</u> The DRCH system provides more than sufficient position resolution for the momentum measurement. However, in the presence of multiple particles per event some ambiguity can arise in con-

necting track stubs between DC2 and DC3. The MWPC system provides a series of low resolution position measurements which aid in determining the correct connections between DC2 and DC3. Each detector consists of a series of vertical anode wires with a spacing of 5.08 mm. Each wire is instrumented with a simple descriminator circuit so that only the hit pattern is recorded.

Time of Flight Upstream(TOFU): A high resolution Upstream Time-Of-Flight hodoscope consisting of 160 plastic scintillator slats (BC404), running along the y direction, was positioned just after DC3. Fast photo-tubes are attached to both ends of each slat. The system measures flight time with a resolution of 85 psec and vertical position with a resolution of 1 cm.

Other "legacy" detectors located further downstream than the TOFU were not used in this analysis.

Chapter 3

Data Reduction

The measurement of the final phase space distribution of collision products is the method by which we probe the dynamics of any subatomic collision. For this the momentum and energy, or equivalently the momentum and velocity must be measured. Specifically, We will present measurements of double differential multiplicities $1/m_t^2 d^2N/dm_t dy$ and rapidity densities dN/dy of protons and charged pions as a function of event centrality. The construction of such spectra require numerous analysis stages, cuts, and corrections. In this chapter we present in great detail the steps necessary to formulate these spectra in a single centrality bin. In Chapter 4 results from other centrality bins,comparisons between bins, and comparisons to complex and simplistic models will be presented without further discussion of the steps necessary to form a singles spectrum. We present only the analysis steps required by the forward spectrometer data. The reader is referred elsewhere [21, 43] for a detailed discussion of calorimeter and beam definition detector analysis.

3.1 Track Reconstruction

The magnetic spectrometer measures the trajectory and velocity of charged particles exiting the analyzing magnet and infers from this information the vector momentum and type of each particle as it left the collision zone. The creation of the list of momenta and species measured in an event from the raw times and pulse heights is called track reconstruction. This step is the most critical and CPU intensive of all steps in the data analysis and is described below. Track reconstruction takes place in four steps. In the first step, calibration, raw data from a single detector are calibrated to produce physically meaningful quantities such as positions and time in standard units. In the second step, pattern recognition, the numerous hits from the spectrometer are formed into a set of lists each of which applies to a single particle. Momentum at the target(prior to magnetic analysis) is determined by analyzing the trajectory measured downstream and assuming the particle originated at the target. Finally, in the particle identification step, the measured momentum and velocity are used to determine the mass, and thereby specie, of each particle.

The majority of these steps are accomplished in a single subroutine called "QUANAH"[1]. QUANAH is run *once* on each event as a part of the STEP1

[1]Quanah Parker was born in Cedar Lakes, Texas around 1845. Son of the Comanche chief Peta Nocone and Cynthia Ann Parker, a white captive since the age of nine, Quanah became the leader of a Kwahadi band of Comanches. His name means 'fragrance' (sweet smell). An excellent *tracker*, he was equally renown for his cruelty and bravery. [31]

stage of analysis. The lists of reconstructed tracks as well as transverse energy, etc, for each event are stored in a specialized format (NTUPLE) and scanned many times prior to the formulation of spectra. More details on Quanah and the step1 routine can be found in [34, 35].

3.1.1 Calibration

The downstream detectors, which require calibration, include TOFU and DRCH detectors. Each of these calibration steps is discussed below:

3.1.2 TOFU Calibration

The TOFU is composed of 160 vertical slats of plastic scintillator equipped with a photomultiplier tube at each end. All calibrations of the TOFU are performed by examination of the recorded data.

Time and pulse height from each tube are recorded for each event. Each of these quantities depends upon the position at which the particle deposited energy. For an energy Q deposited in a scintillator of length l at a vertical position y one finds, to first order, that the times and pulse heights are given by:

$$t_{top} = t_{particle} + \frac{l/2 - y}{v}; \quad t_{bottom} = t_{particle} + \frac{l/2 + y}{v} \tag{3.1}$$

and

$$PH_{top} \propto Qexp^{-\lambda(l/2-y)}; \quad PH_{bottom} \propto Qexp^{-\lambda(l/2+y)} \tag{3.2}$$

where $t_{particle}$ is the time of the particle's incidence, v is the velocity of signal propagation along the scintillator, and λ is the attenuation constant of the scintillator. The position dependences in the time and pulse height can be removed by taking the arithmetic and geometric means respectively:

$$t_{mean} = \frac{t_{top} + t_{bottom}}{2} = t_{particle} + \frac{1}{v} \cdot \frac{l}{2} \tag{3.3}$$

$$PH_{mean} = \sqrt{PH_{top} \cdot PH_{bottom}} \propto Q \tag{3.4}$$

The mean pulse height spectrum is directly proportional to the deposited energy. The proportionality constant is fixed slat by slat by requiring the peak of the energy deposit spectrum to land at 1.0. An example of the result of this calibration is shown in Figure 3.1.

From Eq. 3.3 we see that the mean time spectrum contains a physical offset. During signal transportation, discrimination, and digitization more offsets are accumulated. The overall offset is determined by examining the times recorded for negative tracks. Each negative track (of known momentum) is assumed to be a negative pion and thereby serves to predict the mean time measurement of the slat. The spectrum of differences between this predicted time and that actually recorded by each slat is accumulated and shows a distinct peak corresponding to actual pions. Time offsets are then adjusted slat by slat, and run by run to maintain this peak to within 50 psec of zero.

One second order effect is worth noting. Photomultiplier tubes have finite rise-times. The proper time of a pulse is that time at which the pulse reaches some fixed fraction of its peak height. Our electronics does not record this time. Instead we record that time at which the PMT pulse passes a fixed absolute height. As a result, large signals record times which are too soon and small signals record times which are too late. This effect is known as slewing.

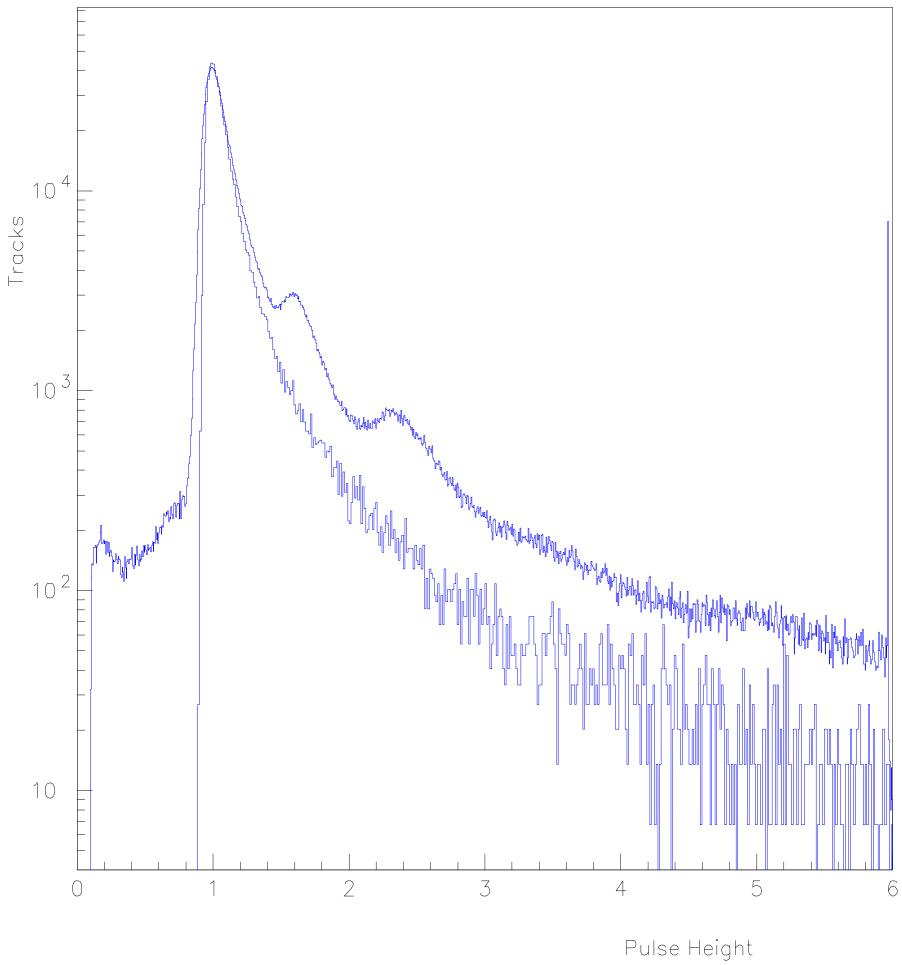

Figure 3.1: TOFU pulse height spectrum and simulated landau charge = 1 distribution.

To good approximation, over the dynamic range in pulse height of our signals, this timing error is inversely proportional to the pulse height. Thus from a single slat the additive correction factor can be written:

$$\delta t_{slew} = \frac{\alpha}{PH_{top}} + \frac{\beta}{PH_{bottom}} \tag{3.5}$$

The parameters α and β are determined slat by slat by trying a grid of possible values and selecting that pair (α, β) which minimizes the width of the peak in the spectrum. Fortunately these constants are quite stable and the calibration need only be performed once for the entire data set.

Finally, the vertical location, y, of the track can be determined from the time difference:

$$t_{bottom} - t_{top} = \frac{2y}{v} \tag{3.6}$$

Although the pulse height equations can also be solved for the vertical position, the time difference determines y with 1 cm precision, roughly 10$\times$ better that that achieved using the pulse height.

3.1.3 Drift Chamber Time Calibration

The DRCH drift sections measure the position at which a charged particle passes by measuring the time at which an avalanche is induced on the anode wire. This time is related to the distance between the ionization trail and the anode wire. Several steps are necessary to deduce the position from the measured time. In a similar manner as done for the TOFU, the calibrations are deduced directly from the measured data.

First, due to cable delays, descriminator thresholds, and digitization effects, there is an unknown time offset for each channel. The relative offsets are determined from the mean measured time in each channel(which should be the same for all channels). Time offsets are adjusted so that the mean time for each channel is the same.

Position is usually determined by assuming that the drift velocity is constant. This is not true near the wire, nor at the far limits of the drift cell. For this analysis, we have developed a new and simple procedure which automatically accounts for the non-linearity of chamber response. Since ionization trails drift in from both sides of each wire, and the chamber occupancy varies slowly compared to the wire spacing, the true spectrum of absolute distances to the nearest wire, integrated over all tracks, should be identically flat. If the chamber response were ideal, one would then expect that the spectrum of drift times would also be identically flat. In this case, the spectrum of times recorded by the chamber would be a square function with sharp corners. The actual spectrum of times bears some similarity to this presumption (Figure 3.2), however the response for both short and long dimes is decidedly non-linear, as expected. If we assume that the efficiency of a single wire cell is uniform over its sensitive area (an excellent assumption for such short drift distances) and that the drift time varies monotonically with increasing absolute distance to the wire, we can take the record of drift times as a direct measurement of the non-linear drift characteristic of the wire chamber. We construct the mapping from measured

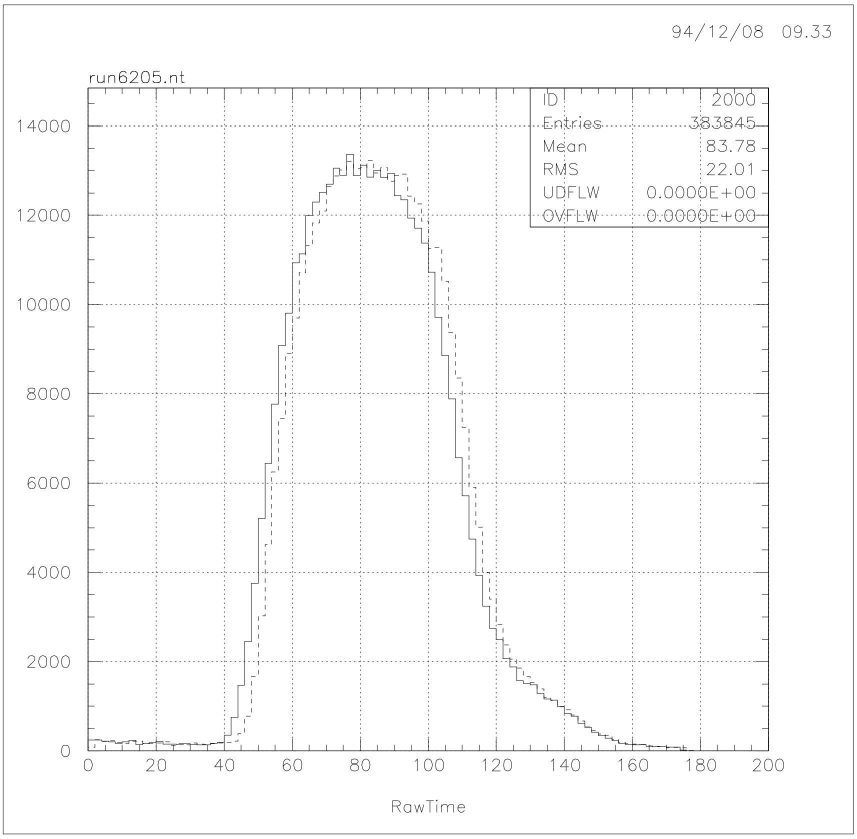

Figure 3.2: Measured time spectrum from the drift chambers.

time,$t_{measured}$, into distance, d, directly from the time spectrum, dN/dt, as:

$$d = f(t_{meas}) = D \cdot \frac{\int_0^{t_{meas}} \frac{dN}{dt'} dt'}{\int_0^{t_{max}} \frac{dN}{dt'} dt'} \tag{3.7}$$

where t_{max} is the largest measured time and D is the largest possible distance (full size of a drift cell). Analysis of this new mapping has shown that it results in a 30% improvement in position resolution at a cells center, two time near the wire, and eliminates "wire structure" from the overall reconstructed position spectrum. The measured resolution is 300μm at DC2 and 600μm at DC3.

3.1.4 Pad Chamber Calibration

The seventh digitization in each DRCH is via the segmented cathode pad chamber. Two stages of calibration of the signals from this device are necessary. First is the pad-by-pad gain calibration. Signals from each cathode pad are amplified prior to digitization. Although in principle the circuitry on each pad is identical, in practice the gains of the amplifiers vary from pad to pad. For this reason, a test pulser system was used to calibrate the gain of each channel. Under computer control, each channel was pulsed with a programmable test pulse capacitively coupled into the pre-amplifier input. Twenty test pulses were fired for each of ten pulser amplitudes. The response at the ADC was recorded and fit to a straight line for amplifier gain. The test pulser system was run prior to the collection of physics data.

If the chevron shapes on the cathode were ideal, the position of a track could be calculated directly from the charge-weighted sum of pad positions as:

$$y = \frac{\sum_{struckpads} q_i y_i}{\sum_{struckpads} q_i} \tag{3.8}$$

where q_i is the charge deposit on the pad located at y_i. As with the drift sections, the pad chamber response is not found to be ideal. In a previous thesis, calculations of charge deposit were used to correct the pads for linearity with reasonable success [14]. However, we have found that better results can be achieved simply by using the integrated position spectrum as a measurement of the chamber characteristic and linearizing following a procedure identical to that applied to the drift times. It should be noted that this procedure was first applied to the y position spectrum in the pad chambers, and has now been applied to measurements as diverse as the reaction plane determination.

3.1.5 Pattern Recognition

Following the calibration step, information from the spectrometer consists of a set of x positions in each drift section, (x, y)'s in each pad chamber, x's in each MWPC, (x, y, charge, time)'s in the TOFU. Since the spectrometer typically registers 7-8 charged particles in each event, there are typically 7-8 wires fired per drift section and MWPC chamber, 7-8 TOFU slats, and 7-8 pairs or triplets of struck pads. This information is ordered detector by detector and in increasing x. Pattern recognition is the process of reordering the information as a list of hits all belonging to the same primary particle rather than the same detector station. This association takes place in several stages, each of which is described only briefly below. Many of the codes run are “legacy” subroutines from the QUANAH version originally written in 1989 and are essentially unchanged. Great detail on the algorithms and data structures involved can be found elsewhere [14, 29]. Here we give only a brief overview.

The first stage of pattern recognition is the creation of a set of lists of drift chamber hits, each of which belong to the same track, called elements. No two elements may share more than a single wire hit in common. This fact reduces the efficiency of reconstructing a track in the presence of a close neighbor. The efficiency loss due to this cut will be discussed in great detail below. “Clusters” are formed from sets of pad hits which share image charge from the same primary track. Pairs of elements and clusters are formed into the “mates” structure. All of these steps are identical to those originally followed in the Si beam experiments.

In the original version of QUANAH (E814, Si beam), pairs of mates were combined with downstream scintillator hits (FSCI) to form track segments. The downstream FSCI hodoscope was located 31 meters away from DC3 and was essential to selecting proper DC2-DC3 associations in the presence of multiple tracks. In E877 the FSCI hodoscope was not used. The TOFU detector is located too close to DC3 to provide rejection for false associations. For this reason the four MWPC detectors were added between DC2 and DC3. Track segments were formed between DC2-DC3 mates if 3 or 4 MWPC wires laying along the line connecting them fired. Due to the high efficiency of each MWPC (> 98), this matching procedure has nearly 100% efficiency.

Subsequent tracking followed exactly the criteria set in the original QUANAH. Segments which satisfied a loose collimator cut graduate to candidates.

Candidates are considered "compatible" if they do not share DC2 or DC3 elements or clusters. The set of maximum compatibles form an ordered list of tracks, each of which references all hits believed to belong to a single particle. Finally, the appropriate TOFU slat is selected by projecting the track to the TOFU z location.

3.1.6 Momentum Reconstruction

Subsequent to the pattern recognition stage, the trajectory of each particle exiting the magnetic field is known. Reconstruction of momentum requires additionally that one assume each track originated from the target and followed a circular trajectory in the analyzing magnet.

The magnetic field has considerable non-uniformities near the pole tips and the coils, our collimation of the reaction products ensures that all good trajectories are analyzed by the magnets "sweet spot". The magnet is thus modeled as a region of uniform magnetic field directed vertically. The effective length of the magnet is set appropriately longer than the poles to account for the integral effects of the fringe fields at the magnet entrance and exit [24].

From Fig. 3.3 and some elementary geometry, we see:

$$R(sin\theta' - sin\theta) = -l \tag{3.9}$$

$$x = ztan\theta \tag{3.10}$$

$$x' - x = R(cos\theta' - cos\theta) \tag{3.11}$$

where R is the radius of curvature in the bend plane, $(x - z)$, of the magnetic field, and x and x' are measured with respect to the interaction x position.

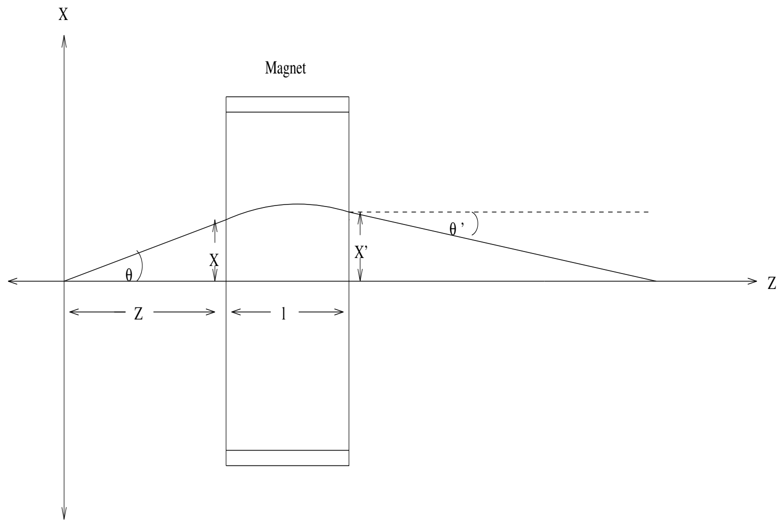

Figure 3.3: Bend plane geometry for a track in the E877 spectrometer

---

The rigidity, p_{xz}/Z of a particle is related to its radius of curvature via:

$$\frac{p_{xz}}{Z} = ReB \tag{3.12}$$

with $p_{xz} = \sqrt{p_x^2 + p_z^2}$ the momentum perpendicular to the magnetic field, e the unit charge, Z the particles charge number, and B the magnitude of the magnetic field.

The trajectory yields a measurement for x' and θ'. The desired quantities are p_{xz}/Z and θ. The equations listed above are not trivially invertible, so a successive approximation procedure is used to determine p_{xz}/Z. A seed value for θ is chosen using a single bend model approximation to the effect of the magnetic field. Using this and the measured θ', one can calculate the seed value for rigidity. Propagation of the seed, tracked forward, results in a discrepancy with the measured x'. θ is then iterated until the x' discrepancy is below $1\mu m$. Convergence is generally achieved in fewer than three iterations.

Once the horizontal component of the momentum, p_{xz}, is known the vertical component, p_y, follows quickly from the relation:

$$\frac{p_y}{p_{xz}} = \frac{y}{s} \tag{3.13}$$

where y is the vertical position of the track at the TOFU and s is the accumulated horizontal path length from the target to the TOFU.

3.2 Particle Identification(PID)

> *Kindly enter them into your notebook. And ,in order to refer to them conveniently, lets call them A,B, and Z.*
>
> –The tortoise in Lewis Carrolls's
> What the Tortoise Said to Achilles

Following the analysis steps listed above, the spectrometer data have been reduced to a collection of tracks which list, for each reconstructed particle, its momentum, $\vec{p}$, and velocity, β. Using these two quantities we are able to reconstruct the particles mass via:

$$m = \frac{p}{\beta\gamma} = p\left(\frac{\sqrt{1-\beta^2}}{\beta}\right), \qquad \gamma = \frac{1}{\sqrt{1-\beta^2}} \tag{3.14}$$

Indeed, mass is that property which serves to uniquely determine a particles identity. It is the equivalent of a subatomic fingerprint. PID is effected by defining gates for each particle specie in some suitable space. Definition of these gates relies upon a detailed understanding of the spectrometer resolutions.

3.2.1 Momentum Resolution

The relativistic Achille's heal of any velocity based particle identification is the fact that velocity, β, saturates at a value of 1. Understanding of finite momentum and timing resolution are critical. Propagation of these resolutions into the PID variable, in this case the mass squared, determines a devices' dynamic range.

Mass squared can be constructed from direct observables in the following manner. The track reconstruction yields momentum and path length (l) which, with the measured time of flight, determines the velocity β. Given β and momentum one can calculate the squared mass associated with each track via the relation:

$$m^2 = p^2 \left(\frac{1}{\beta^2} - 1 \right) = p^2 \left(\frac{TOF^2}{l^2} - 1 \right). \tag{3.15}$$

m^2 is the variable used for particle identification as it does not suffer the divergence that m suffers when the finite resolution of the TOF causes γ to go imaginary. Fig. 3.4 shows a plot of mass squared as a function of momentum for particles eventually identified as pions and protons.

The m^2 resolution depends upon the the momentum resolution of the tracking system and the timing resolution of the TOFU. From 3.15 the contribution

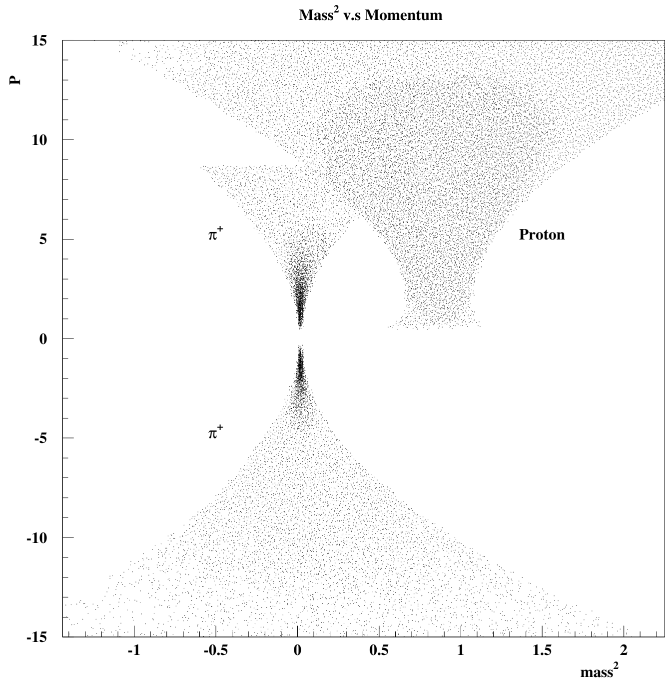

Figure 3.4: The particle identification capability of the E877 spectrometer. Included are the Proton, π^+, and π^- coverage.

to the mass resolution from TOF is given by:

$$\delta(m^2)_{TOF} = p^2\delta\left(\frac{1}{\beta^2} - 1\right) = -p^2\left(\frac{2}{\beta^3}\right)\delta\beta \tag{3.16}$$

$$= \frac{2p^2}{\beta}\left(\frac{\delta(TOF)}{l}\right) \tag{3.17}$$

Similarly the momentum resolution's contribution is

$$\delta(m^2)_p = 2p\left(\frac{1}{\beta^2} - 1\right)\delta p = 2m^2\left(\frac{\delta p}{p}\right). \tag{3.18}$$

The mass resolution is found by adding 3.17 and 3.17 in quadrature;

$$(\delta(m^2))^2 = (\delta(m^2)_{TOF})^2 + (\delta(m^2)_{mom})^2 \tag{3.19}$$

$$= \frac{4p^4}{\beta^2}\left(\frac{\delta(TOF)}{l}\right)^2 + 4m^4\left(\frac{\delta p}{p}\right)^2. \tag{3.20}$$

Momentum resolution itself can be broken down into two components, that arising from the finite angular resolution of the spectrometer, and that coming from multiple scattering. Using the small angle approximation momentum is measured in our spectrometer by (Fig. 3.3)

$$p = \frac{0.3\int Bdl}{\theta_1 - \theta_2} \tag{3.21}$$

thus

$$\delta(p)_\theta = 0.3\int Bdl\ \delta\left(\frac{1}{\theta_1 - \theta_2}\right) \tag{3.22}$$

$$= \frac{0.3\int Bdl}{(\theta_1 - \theta_2)^2}\delta\theta = \frac{p^2}{0.3\int Bdl}\delta\theta. \tag{3.23}$$

Coulombic multiple scattering is characterized, in the Gaussian approximation [37] , by a width

$$\delta(\theta)_{ms} = \frac{0.0136Z}{\beta p}\sqrt{\frac{x}{X_o}}\left(1 + 0.038\ln\left(\frac{x}{X_o}\right)\right) \tag{3.24}$$

Z $\equiv$ charge of the particle in units of e

$x/X_o \equiv$ amount of material in units of radiation length

Using equation 3.23 we find

$$\delta(p)_{ms} = \frac{pC_3}{\beta} \tag{3.25}$$

with

$$C_3 = \frac{0.0136Z}{0.3\int Bdl}\sqrt{\frac{x}{X_o}}\left(1 + 0.038\ln\left(\frac{x}{X_o}\right)\right) \tag{3.26}$$

The total momentum resolution is found by adding each component in quadrature, thus

$$\left(\frac{\delta p}{p}\right)^2 = \left(\frac{\delta p_\theta}{p}\right)^2 + \left(\frac{\delta p_{ms}}{p}\right)^2 \tag{3.27}$$

From 3.20 we find

$$(\delta(m^2))^2 = \frac{4p^4}{\beta^2}C_1^2 + 4m^4p^2C_2^2 + \frac{4m^4}{\beta^2}C_3^2. \tag{3.28}$$

$$C_1 = \frac{\delta(TOF)}{l}$$

$$C_2 = \frac{\delta\theta}{0.3\int Bdl}$$

Finally, with $\beta^2 = p^2/(p^2 + m^2)$, we see that

$$(\delta(m^2))^2 = 4p^2(m^2 + p^2)C_1^2 + 4m^4p^2C_2^2 + 4m^4\left(1 + \frac{m^2}{p^2}\right)C_3^2 \tag{3.29}$$

Figure 3.5 shows the experimental resolution of the squared mass as a function of momentum. Also plotted are the results of fitting this resolution to Eq 3.29, letting C1, C2, and C3 vary as free parameters. These values and the experimental resolution they imply are found in Tables 3.1 and 3.2. The resolutions stated in table 3.2 are, for protons, consistent with calculated values [41]. The differences in the values of C1, C3, and C3 can be attributed

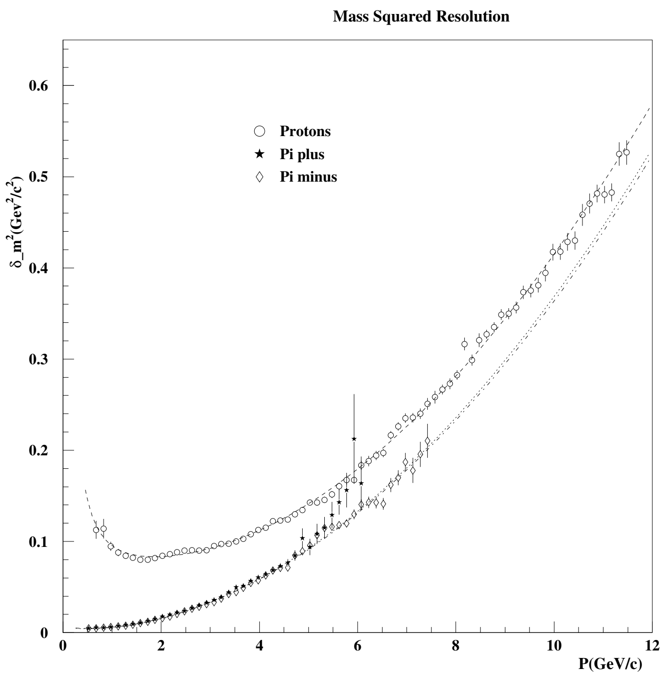

Figure 3.5: Squared mass resolution as a function of momentum for protons, π^+, and π^-.

Specie	C1	C2	C3
π	0.00183 $\pm$ 0.00001	0.0611 $\pm$ 0.0048	0.1093 $\pm$ 0.0014
Proton	0.00189 $\pm$ 0.00002	0.00870 $\pm$ 0.00045	0.03898 $\pm$ 0.00045

Table 3.1: Coefficents of eq 3.29, the squared mass resolution as a function of momentum. These coefficients are related to experimental resolutions as discussed in the text.

---

to a broadening of the width of the pion mass resolution, especially at low momentum, due to hyperon decay. This will be discussed in more detail in Chapter 4. For pion PID we use the values stated in the table, as these are the values that best fit the pion widths, and choose to later quantify lambda contribution to the spectra.

For the purposes of this thesis, particle identification only extends to the ID of protons and charged pions. For negative particles, we assign the particle ID as negative pion if the measured mass of the particle falls within $\pm 2.5\sigma$ of the true pion mass squared. For positive particles the situation is somewhat more complex. At sufficiently high momentum the positive pion and proton band merge due to insufficient mass resolution. Since the proton abundance at high momentum is many times that of the pion, we suffer less than 2% contamination by tagging all particles within $\pm 2.5\sigma$ of the proton band up to a momentum of 15 GeV/c. Positive tracks that are not identified as protons

Specie	σ**(TOF)(ps)**	$\sigma\theta$**(rad)**	x/X_o**(rad length)**
π	75.85 $\pm$ 0.41	0.00500 $\pm$ 0.00039	0.470 $\pm$ 0.002
Proton	77.49 $\pm$ 0.82	0.00071 $\pm$ 0.00004	0.069 $\pm$ 0.001

Table 3.2: Measured resolutions as well as radiation thickness of the spectrometer.

---

are labeled pions if they fall within $\pm 2.5\sigma$ of the pion mass squared and have a momenta below 8.7 GeV/c.

At this stage, the spectrometer analysis is complete and supplies vector momenta of identified charged pions and protons for further analysis.

3.3 Cuts and Efficiencies

A variety of cuts are applied during the analysis of data. It is essential that the efficiency and effectiveness of each cut be understood so that the measurements may be corrected and presented on an absolute scale. Cuts are applied to all three of the major E877 detector systems. Spectra in the form d^2N/dm_Tdy and dN/dy are normalized to the number of events analyzed. As such, cuts which reduce the number of events analyzed without bias do not effect the data. All cuts on the beam definition detectors (pulse height in S2 and S4; pulse height in SILI; single track in BVer) do not effect the normalization of data and can be quite tight. Cuts on the event characterization detectors are used to select event classes within which spectral data are to be analyzed. As such they do not have an effect upon the overall normalization.

Cuts on the detectors in the spectrometer do have a direct influence on the spectral data. These cuts fall into two classes: momentum dependent and momentum independent. We will deal with these two classes separately.

3.3.1 Momentum Independent Spectrometer Cuts

Four terms contribute to the momentum independent spectrometer efficiency:

$$\epsilon_{spectrometer} = \epsilon_{chamber} \cdot \epsilon_{TOFU} \cdot \epsilon_{pattern} \cdot \epsilon_{PID} \tag{3.30}$$

where

$\epsilon_{chamber} \equiv$ Mate finding efficiency

$\epsilon_{TOFU} \equiv$ TOFU pulse height and firing efficiency

$\epsilon_{pattern} \equiv$ Singles track segment finding

$\epsilon_{PID} \equiv$ PID cut efficiency

In the present discussion we are considering the single track efficiency only. Clearly in the presence of multiple tracks, some confusion (and hence inefficiency) may occur during pattern recognition. Since the probability of being thus confused depends upon the local particle density at the chamber, it is a momentum dependent correction and will be discussed below.

The mate structure makes associations between the drift and pad sections in DC2 and DC3. Long ago, it was realized that the pad chamber section was considerably less reliable than the drift section in that a single dead pad results in zero local efficiency for reconstructing a properly measured cluster. For that reason a mate is formed for every element regardless of whether a matching cluster is found or not. Thus, the main efficiency is equal to the wire section efficiency.

The wire section efficiency, for a single track, is quite high owing to the high level of redundancy in the measurement. Although each track has the opportunity to be digitized six times by the drift section, only three measurements are required for reconstruction. We determine the probability of such failure by examining the distribution of wires fired per track, shown in Figure 3.6. The overall number of wires firing per chamber per track obeys a binomial distribution whose average is 5.2 for DC2 and 5.05 for DC3. We thus deduce efficiencies of 0.997 and 0.996 for DC2 and DC3 respectively and therefore deduce $\epsilon_{chamber} = 0.993$.

The TOFU detector is constructed so as to maximize the efficiency for detecting particles. Slats are arranged to have overlap so that no particle can "slip through the cracks", since there are no cracks. The efficiency for particle detection was measured by the McGill group [43] and found to be better than 0.99. We assume this efficiency to be 1.0. A more severe inefficiency is imposed by the pulse height cut. Shown in Figure 3.1 is the distribution of measured pulse heights in the TOFU. Clear peaks are visible for charge one particles, two particles with charge one, and charge two particles. To eliminate tracks which share the same scintillator (and thus have mis-measured times) we place a pulse height cut from 0.7 to 1.4 mips. This cut removes isolated tracks whose energy deposit falls in the high end tail of the Landau distribution. The survival probability for an isolated track is measured by fitting a Landau to the observed distribution and is found to be $\epsilon_{TOFU} = 0.89 \pm 0.03$. The probability of falling prey to a second track is position and thus momentum dependent and is dealt with below.

The overall number of wires firing per chamber per track obeys a binomial distribution whose average is 5.2 for DC2 and 5.05 for DC3. The pattern recognition code, Quanah, requires three of the six planes in each chamber to fire to consider a track, and the overall efficiency of each chamber is then 0.997 and 0.996 for DC2 and DC3 respectively(Fig. 3.6). TOFU pulse height cuts, applied to ensure exclusion of two singly charged particles, were placed at 0.7 mip (minimum ionizing particle) and 1.5 mip. TOFU efficiency was estimated by fitting the observed pulse height distribution to a Landau distribution, and then evaluating the fractional area of the curve within our cuts, this gives us a pulse height efficiency of 0.89 $\pm$ 0.03. Particle identification efficiency was evaluated in a similar manner as the TOFU cut. The measured mass squared distribution was fit to a Gaussian and the fractional area of the curve within our cuts was evaluated. The pid efficiency is 0.99.

The segment finding probability concerns the probability of finding sufficiently many MWPC hits to form a track. The singles probability of an MWPC was measured to be better than 0.99. The pattern recognition requires only three of the four chambers to fire. We thus set the firing probability to 1.0. The cut width was set rather wide. In a GEANT simulation, no tracks failed to

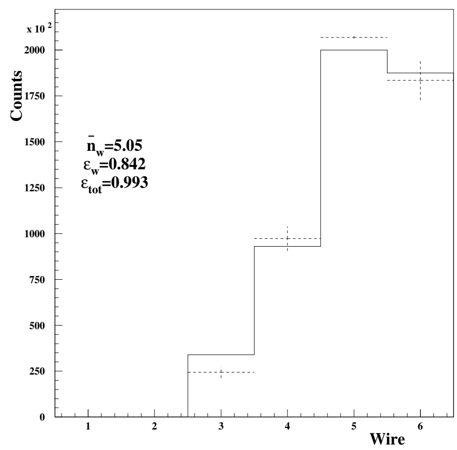

Figure 3.6: The distribution of the number of wires per element in DCIII. The mean is 5.05, the dashed points are a binomial distribution with the same mean.

reconstruct due to problems in the MWPC algorithm. We take $\epsilon_{TOFU} = 1.0$. Finally we use a Gaussian assumption and estimate the PID cut efficiency to be 0.99.

Overall the single track efficiency is taken to be 0.875 ± 0.030. A detailed GEANT simulation of the tracking system was used to verify this number . There, in the absence of the tofu pulse height cut, the efficiency for tracking single tracks in the spectrometer was found to be essentially 1.0, consistent with the above analysis.

3.3.2 Momentum Dependent Efficiencies

There are two sources of momentum dependent efficiencies in our analysis. The first source comes from the particle ID routine. As shown in Figure 3.4, above a momentum of 6.0 GeV/c there is overlap of the proton and pion tails. In the overlap region, all particles are assumed to be protons. Due to the relative rarity of pions in this momentum range, this adds a background of at most 2% to the proton spectrum and is ignored. However, there is a considerable loss to the pion signal. Since we have effectively parameterized the pion width, we can estimate the momentum dependent loss of signal and correct. We dare to correct only as much as a factor of two which places an upper limit of 8.7 GeV/c to the positive pion measurements.

The second source of a momentum dependent correction is that due to tracking inefficiencies created by particle overlap. This correction is estimated and applied concurrently with the acceptance calculation. As such, we will only discuss it in the context of the acceptance correction.

3.4 Acceptance

If God has made the world a perfect mechanism, He has at least conceded so much to our imperfect intellect that in order to predict little parts of it, we need not solve innumerable differential equations, but can use dice with fair success.

–Max Born

Following the particle ID step, we have a list of identified particles each of which is of a known vector momentum. The construction of a spectrum is, in principle, the process of counting the number of times a particular species is found to have a transverse mass m_t within an interval dm_t and a rapidity y within an interval dy, or $1/m_t^2 \times d^2N/dm_t dy$. Due to the small size of the spectrometer opening, we only capture a fraction of the particles produced in each such bin. The acceptance calculation is simply the determination of that fraction for every examined bin in m_t and y.

We measure this fractional probability following a Monte Carlo procedure by generating test particles with a physically reasonable distribution, 'tracking' them through a software model of the spectrometer itself, and applying the same cuts to the test track as are applied to real tracks. The number of such software particles 'measured' divided by the number generated in each m_t and y bin is the acceptance function.

It is at this stage of analysis that we correct for momentum dependent efficiencies. This correction is implemented by calculating, for each test particle, its survival probability in the presence of other tracks which threaten to confuse the pattern recognition program.

3.4.1 Test Particle Generator

If the acceptance in a single bin were the same for all m_t within dm_t and all y within dy, the spectrum with which the Monte Carlo particles were generated would be entirely irrelevant. Indeed this is the case for those bins which do not border the edges of the acceptance. At the edge, however, the acceptance function determination can vary significantly with different assumptions of the generator. Our test particle generator allowed the user to input the desired width of a Gaussian rapidity distribution and the Boltzmann temperature as a function of rapidity. These were initially taken as a guess, and then iteratively adjusted to match the data in regions where the spectral shape is irrelevant.

The physical limitations of detection (such as collimator edges and detector active areas) are fixed in lab position space. However, particle characteristics, such as m_t and y, are measured relative to the incident beam particle. To account for this subtle difference, the 'beam coordinate system' (origin at target and Z along incident Au nucleus trajectory) was randomly generated to match that of the actual data set. Shown in Figure 3.7 is the measured spectrum of beam location and inclination at the target(lab system). This spectrum, integrated over the entire data set, was used as an input to the test particle generator's software beam trajectory.

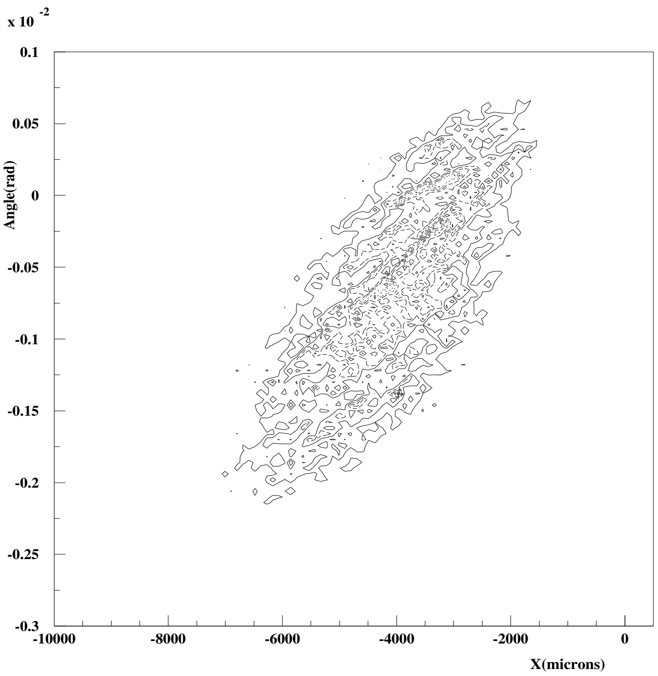

Figure 3.7: The measured beam x position versus angle.

3.4.2 Software Model of Spectrometer

Software modeling of curved trajectories in the spectrometer magnet uses identically the same routine as described in section 4.1.6 (momentum reconstruction). Charged particles are assumed to follow a helical trajectory through a uniform magnetic field and straight lines in free space. The software model determines the x and y coordinates at which the particle passes the collimator and each active detector. Cuts are applied to ensure that the particle always landed in the active region.

Often, the performance of a detector near its physical edges can be marginal. Additionally, small errors in alignment of each detector could effectively misalign the software and hardware edges of any detector. For this reason we cut both physical tracks and software tracks on a 'fiducial' region smaller than the active area or opening of each defining aperture. Great care must be taken to ensure that the cuts applied to real and software tracks are identical. Starting with this thesis, software and hardware tracks were cut using the *same* subroutine. A summary of the geometric cuts used for this analysis is shown in Table 3.3. Following the application of these cuts, each test particle had an acceptance of either 1 or 0.

In the case of pion tracks, there is some probability that the pion will decay prior to reaching TOFU. This effect is modeled by calculating the probability, $\epsilon_{nodecay}$, that each accepted particle would have decayed. The number of accepted particles is then incremented by $\epsilon_{nodecay}$ instead of 1 to account for decay losses.

Device	**Z position**	**X cut**	**y Cut**
Collimator	1604900	-82000 - 1480	-5000 - 7500
DCII	5400000	-600000 - 150000	–
PCI	6632600	-79000 - 20000	–
PCII	7840600	-88000 - 30000	–
PCIII	9086900	-97000 - 41000	–
PCVI	10317200	-94000 - 48000	–
DCIII	11545875	-1350000 - 607000	–

Table 3.3: Geometry of the E877 spectrometer and fiducial cuts used in the fall 1993 analysis. All measurements are in microns.

3.4.3 Modeling Interference of Neighboring Track

The most troublesome and critical correction which must be applied to the data is that resulting from inefficiency due to pattern recognition failures resulting from the interference of a neighboring particle . Since the distribution of particles across the face of DC2 and DC3 is not uniform, the loss probability is highly position and thereby momentum dependent. We choose to model this effect in a similar manner to that of decays; we calculate the survival probability, $\epsilon_{nonoverlap}$, for each test track based upon the positions at which it crosses DC2 and DC3. The final acceptance for each test track is then either $\epsilon_{nodecay} * \epsilon_{nonoverlap}$ or 0.

The occupancy per wire for central collisions varies from 3% to 18% in DC2 as shown in Figure 3.9. Any detector is characterized by some finite 2-track resolution. In the case of a drift chamber, this resolution is defined by the sense wire spacing. Multiple tracks that fall within some spatial separation will not efficiently be reconstructed as multiple tracks. A plot of the measured distribution of track separations can be seen in Fig 3.8. The most notable feature in this Figure is the dramatic fall off at separations less than 1 and 2 cm for DC2 and DC3 respectively. This fall off is due to the loss of efficiency of reconstruction at small separations. The spectrum of Figure 3.8 alone is insufficient to reconstruct the true efficiency as a function of separation(*e.g.* does the zero probability of zero track separation indicate 0% reconstruction of 50% reconstruction?). Rather than attempt to deconvolute the the details of the spectrometer response for for small separations, we have chosen to simplify it.

One simple response function would be a square response; 0% two track efficiency below some minimum separation and 100% efficiency above. This is imposed upon real tracks by throwing out tracks with separations below the minimum. This is then imposed upon software tracks by calculating the probability that no track is found within the minimum separation, $\epsilon_{nonoverlap}$, as discussed above. From Figure 3.8, it is apparent that 1 cm and 2 cm minimum

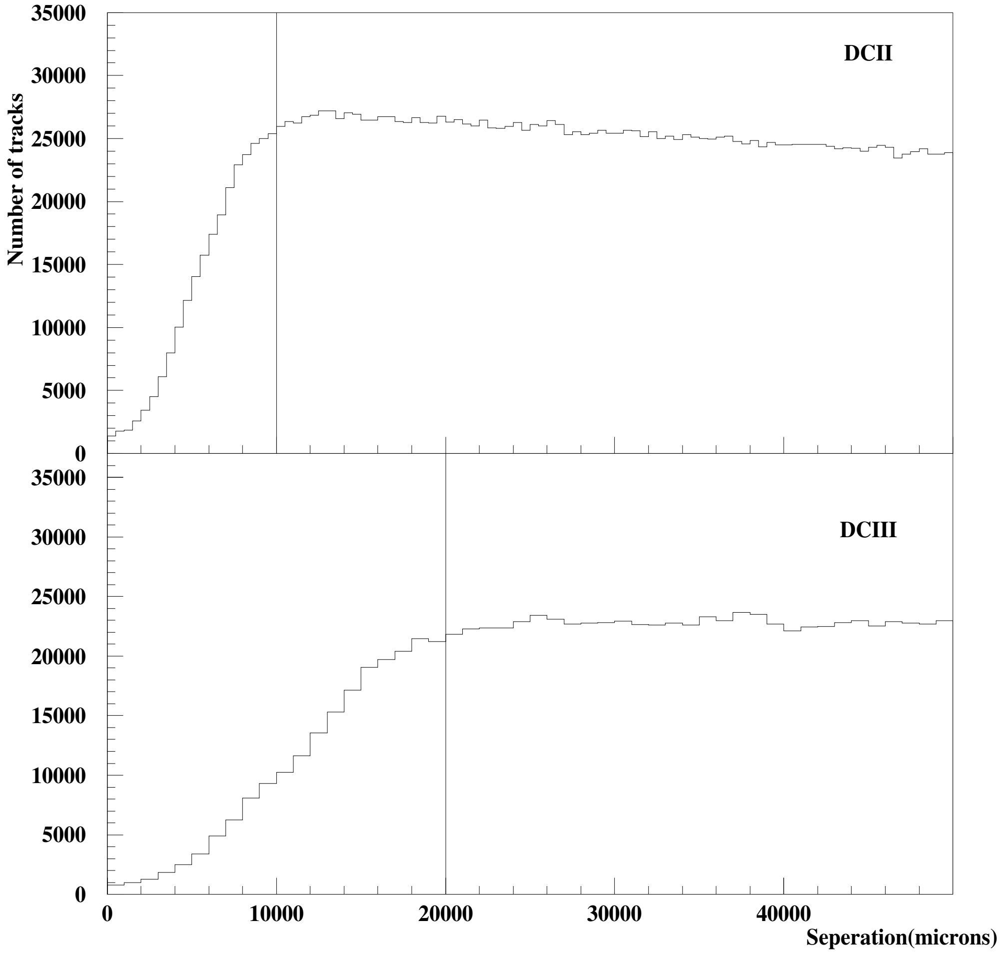

Figure 3.8: Measured separation distribution for close tracks. Reconstruction efficiency drops off dramatically for track separations smaller than 1 cm at DCII and 2 cm at DCIII. The vertical lines correspond to the minimum separation cuts as discussed in the text.

separation cuts in DC2 and DC3 are adequate.

The overlap probability distribution is entirely data driven using the fractional probability of a single wire firing. Note that this probability is determined from wire firings, not reconstructed tracks, and as such is unaffected by the efficiency of the tracking algorithm. Fig 3.9, is the probability of finding a charged track in a region whose size is equal to the wire separation. This is fitted to a polynomial denoted $f(x)$. Such fits are made for each drift chamber, field polarity, and centrality. The probability of *not* finding a track with separation less than the wire spacing at, say, DC2 can be represented as

$$probability \quad no \quad firing = 1 - f_{DC2}(x) \tag{3.31}$$

This can also be interpreted as the probability of not firing within $ws/2$ *and* $ws/2$, where the probability of firing within $ws/2$ is $g(x)$ i.e,

$$\{1 - f_{DC2}(x)\} = g_{DC2}(x) \cdot g_{DC2}(x) \tag{3.32}$$

or

$$g_{DC2}(x) = \{1 - f_{DC2}(x)\}^{\frac{1}{2}} \tag{3.33}$$

By a simple extension one can say that the probability of not firing within ws/N *and* ws/N *and* $\ldots ws/N$ (N times), where the probability of firing within ws/N is $h(x)$, is

$$\{1 - f_{DC2}(x)\} = h_{DC2}(x) \cdot h_{DC2}(x) \ldots \cdot h_{DC2}(x) = \prod_{i=1}^{N} h_{DC2(i)}(x) \tag{3.34}$$

or

$$h_{DC2}(x) = \{1 - f_{DC2}(x)\}^{\frac{1}{N}} \tag{3.35}$$

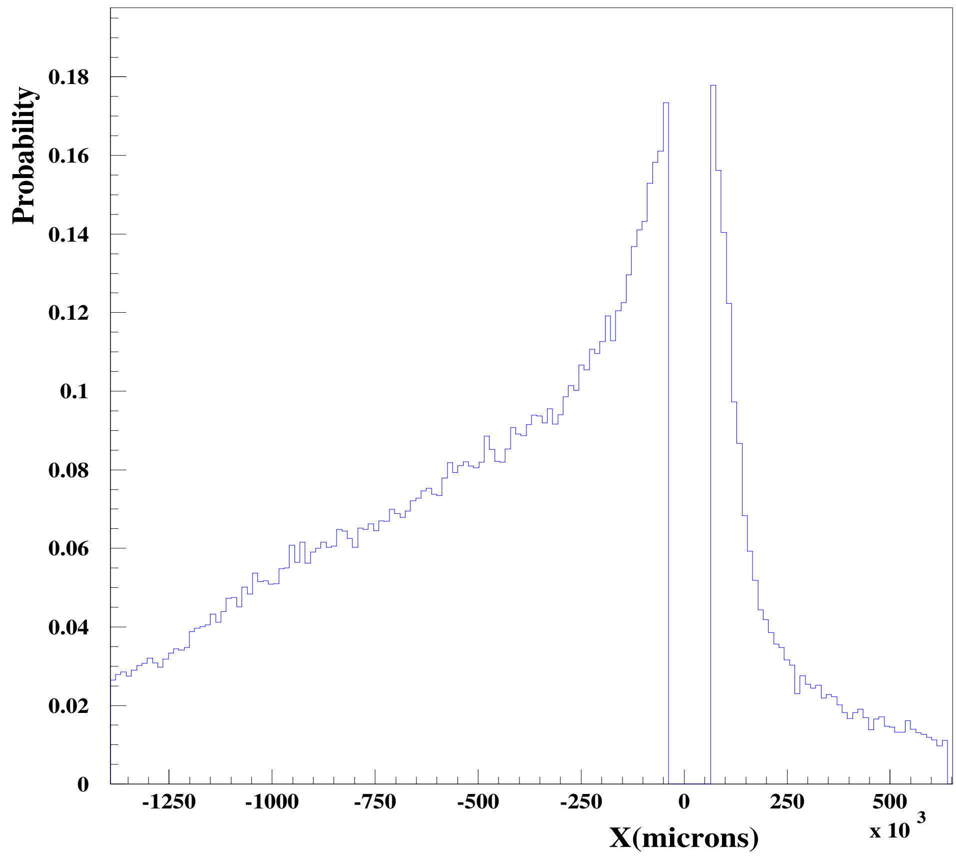

Figure 3.9: Measured DCIII occupancy. The occupancy varies from 3% at the farthest edge to 18% near the incident beam.

If we define some separation $minsep = \frac{ws}{N}$, then $N = \frac{ws}{minsep}$, and from Eq 3.35 we can say that the probability of not firing, $h_{DC2}(x)$, within some arbitrary minsep is

$$h_{DC2}(x) = \{1 - f_{DC2}(x)\}^{\frac{minsep}{ws}} \tag{3.36}$$

If the overlap in DC2 and DC3 were entirely un-correlated we would then have

$$\epsilon(x_{DC2}, x_{DC3}) = h_{DC2}(x_{DC2}) \cdot h_{DC3}(x_{DC3}). \tag{3.37}$$

If, however, the neighbor interfering with the test particle in DC3 were always the same track then, since overlaps in DC2 are more probable,

$$\epsilon_{correlation}(x_{DC2}, x_{DC3}) = h_{DC2}(x_{DC2}) \cdot 1. \tag{3.38}$$

The actual probability of total reconstruction depends upon the probability that the interfering track in DC2 also interferes in DC3. This probability, $\delta(x_2, x_3)$, can be measured using reconstructed tracks.

$$\epsilon_{nonoverlap}(x_{DC2}, x_{DC3}) = h_{DC2}(x_{DC2}) \cdot \delta(x_2, x_3) + h_{DC2}(x_{DC2}) \cdot h_{DC3(X_DC3)} \cdot (1 - \delta(x_2, x_3)) \tag{3.39}$$

Due to the size of the DC3 minimum separation cut(2cm) and the close proximity of the 1cm wide TOFU hodoscope slats, losses in efficiency due to overlap in the TOFU are already accounted for fully by the h_{DC3} factor. Overall, the factor $\epsilon_{nonoverlap}$ varies from 0.62 to 0.87.

The effectiveness of this correction was tested using a full GEANT simulation of the detector response and reconstruction of Monte Carlo tracks. Additionally, an independent effort at McGill University attempted to model

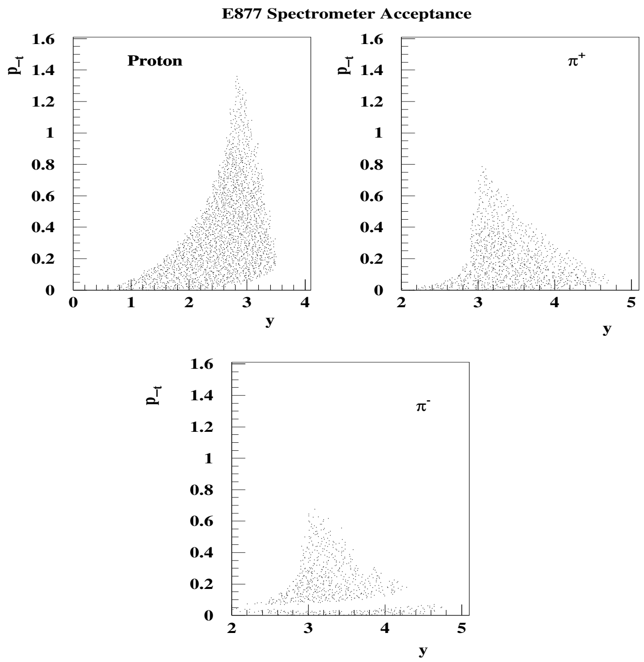

Figure 3.10: The E877 spectrometer acceptance v.s. p_t and y for the fall 1993 Au run. Included are the Proton, π^+, and π^- coverage.

---

the efficiency loss as a function of separation using a smooth function. The Monte Carlo test showed that the spectra were reconstructed to better than 5% in all bins. Additionally, comparison to the McGill effort showed less than 5% difference to the results presented here. These comparisons allow us to assign a systematic error of 10% to the final reconstructed spectra.

3.4.4 Acceptance Functions for Protons and Pions

The acceptance calculated for protons and charged pions is shown in Figure 3.10. Several features are worth noting. For each specie the left-most boundary corresponds to the x edge of the collimator, and the right-most boundary to the maximum momentum for which clean particle ID is achieved. For protons with $y > 2.6$ the acceptance does not extend down to $p_t = 0$ due to the deadened region of the spectrometer. This same region is responsible for the swath of zero acceptance for negative pions at $p_t = 150 MeV/c$.

3.5 Construction of Spectra

3.5.1 Proton Spectra

Au + Au proton spectra, for the upper four percent most central collisions, as measured by the E877 experiment are shown in Figure 3.11. The spectra are plotted as $1/m_t^2 \times d^2N/dm_t dy$ v.s. $m_t - m_{prot}$, a representation in which a Boltzmann is a pure exponential. The spectra are plotted in rapidity bins of 0.1, and in constant p_t bins of 20 MeV/c. Also plotted are the fits to a Boltzmann distribution for those rapidities that can be fit to a finite temperature. A few features are obvious upon examination. Firstly, the spectra are well described by a Boltzmann for $2.3 \leq y \leq 3.5$. For smaller rapidities, especially at the lowest m_t the spectra seem to be flatter than a Boltzmann, as pointed out elsewhere [52, 33]. Second, the slopes of the spectra are monotonically decreasing as one approaches mid-rapidity, and as such the associated temperature parameters increase towards mid-rapidity. Another feature in the spectra is a small, low temperature parameter component discernible at low m_t near beam rapidity. This cold component corresponds to beam rapidity protons that at best suffer elastic collisions with the target. Such low m_t enhancement has been observed in smaller systems such as Si+Al, and also in central Si+Pb where the target and projectile fully overlap [34, 38]. When fitting proton slopes, this component is excluded from the fit region, though evaluation of dN/dy necessarily includes it. It should be noted that the E877 spectrometer has no rejection for the decay daughters of hyperons, and as such this measurement includes their contribution. The effect of these decay products on the various spectra will be discussed in more detail in Chapter 4.

Figure 3.12 shows proton slope parameters, T_B, as a function of rapidity for the upper four percent central collisions. Closed symbols represent our measurement, reflection about mid-rapidity is indicated by the open symbols. The functional form of the temperature parameter is strictly non-$sech(y)$, in variance with what would be expected from a simple thermal picture.

The spectra can be integrated to find the rapidity density, dN/dy, of protons. The acceptance of the forward spectrometer (Fig 3.10) has a sufficient p_t bite to allow good Boltzmann fits in the region $2.3 \leq y \leq 3.5$. In this region the data, where available, has been explicitly integrated, and, where unavailable, the yield has been extrapolated using a Boltzmann and the fitted slope parameters. The results of this operation can be found in Figure 3.13.

Although the E877 spectrometer does not have sufficient p_t coverage below $y = 2.3$ to fit a Boltzmann, it does have coverage out to a p_t of 100 MeV/c down to a rapidity of $y = 1.4$. Integration of the spectra can be performed out to 100 MeV/c in p_t and subsequently give a 'short' rapidity spectra that relies on no assumptions or extrapolations, and can be directly compared to the various models. This is presented in Figure 3.14. As this measurement extends below mid-rapidity, and must be symmetric with respect to reflection about mid-rapidity, it also serves as a check on experimental systematics. In order to get a more global view of the phase space distribution of final state protons Fig 3.15 shows a three dimensional plot of the proton spectra. In this Figure we have reflected our data across mid-rapidity.

3.5.2 Pion Spectra

Figure 3.16 shows charged pion spectra in rapidity bins of 0.1 units of rapidity, and constant p_t bins of 20 MeV/c. Also plotted are Boltzmann distributions whose temperatures are fit to the high m_t tail of the spectra, specifically to the region $200MeV \leq p_t \leq 600MeV$, in rapidity bins where this tail is clearly discernible. The pion spectra show a clear deviation from a Boltzmann at low p_t, an enhancement that was clearly shown to arise from decay of the Δ resonance [39, 40, 42].

The spectra can, in a similar manner to the protons, be integrated over to find the rapidity density, dN/dy. The acceptance of the forward spectrometer (Fig 3.10) has a sufficient p_t bite to allow good Boltzmann fits for π^- in the region $2.9 \leq y \leq 4.5$, and for π^+ from $2.9 \leq y \leq 4.1$. In these regions the data, where available, has been explicitly integrated over, and, where unavailable, the yield has been extrapolated using a Boltzmann and the fitted slope parameters. The results of this operation, for both charge states, can be found in Figure 3.17. Circles represent those rapidity bins where a second hot component can be deduced from the data, triangles are those bins where only a single component is measured.

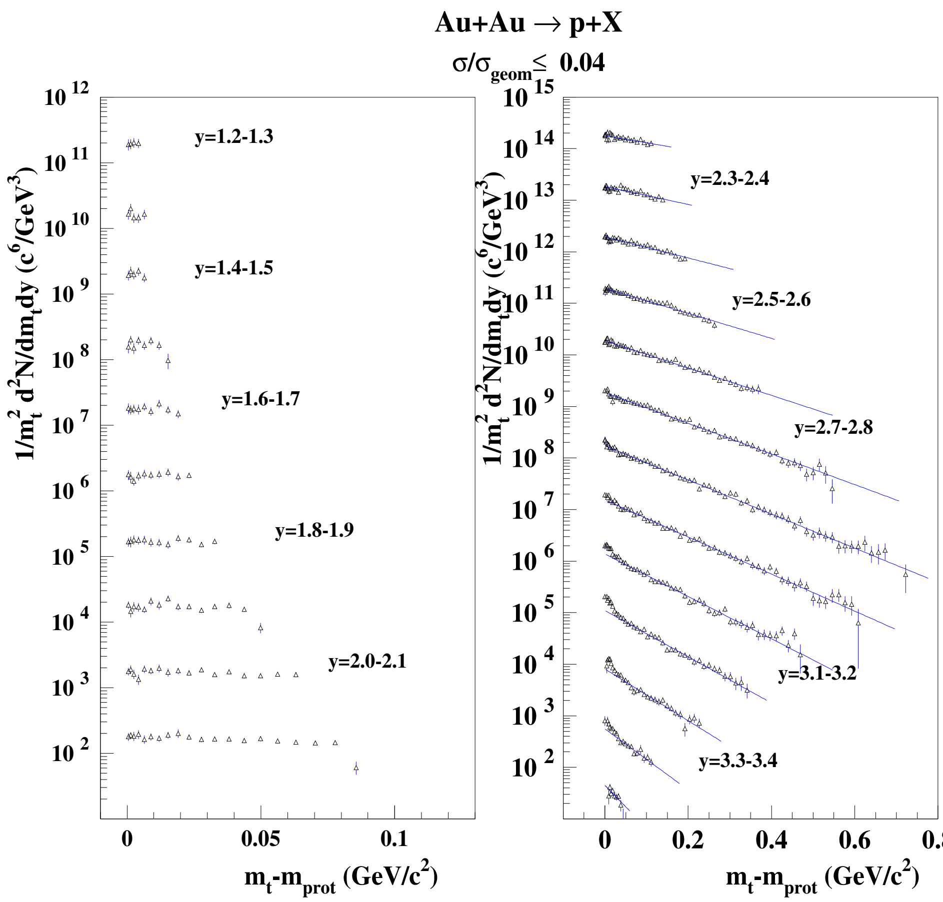

Figure 3.11: Measured proton spectra in Au + Au collisions at 10.8 GeV/c and 4% inclusive centrality.

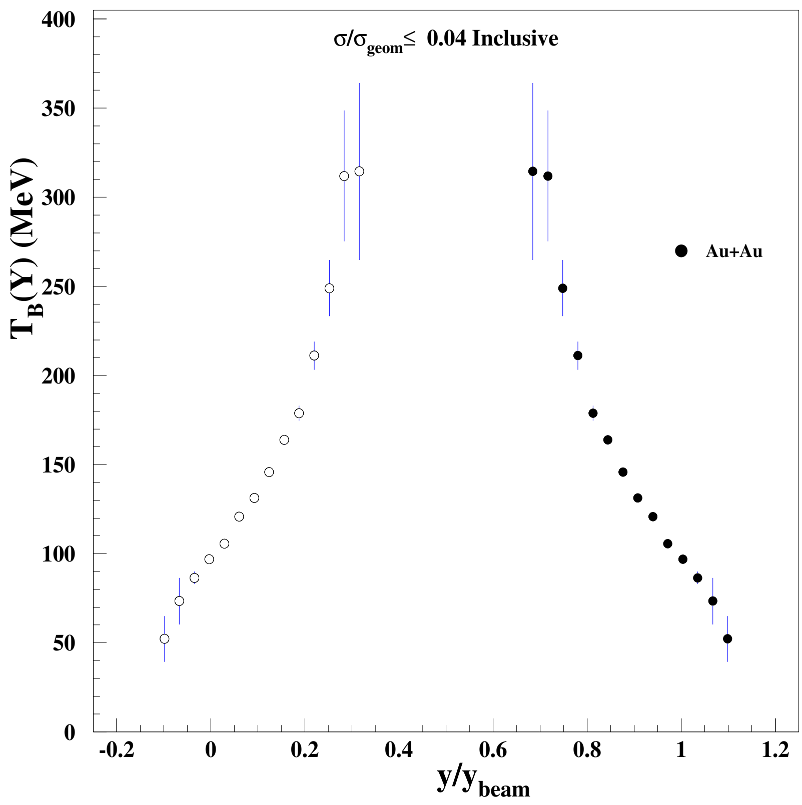

Figure 3.12: Measured proton temperature parameters in Au + Au collisions at 10.8 GeV/c and 4% inclusive centrality.

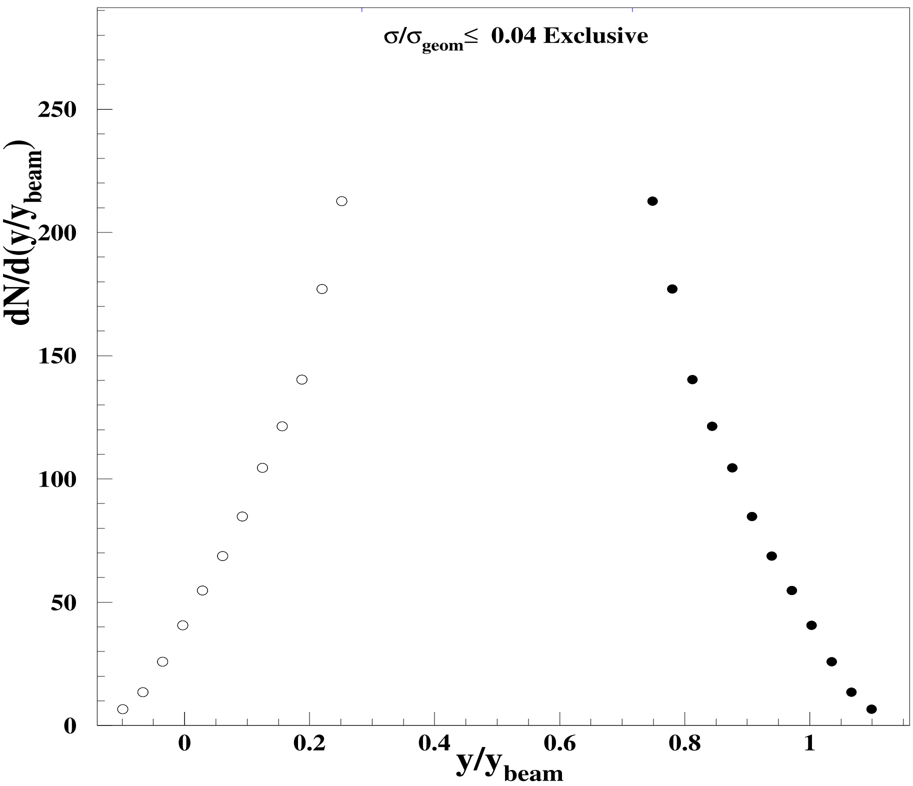

Figure 3.13: Measured proton rapidity density in Au + Au collisions at 10.8 GeV/c and 4% inclusive centrality.

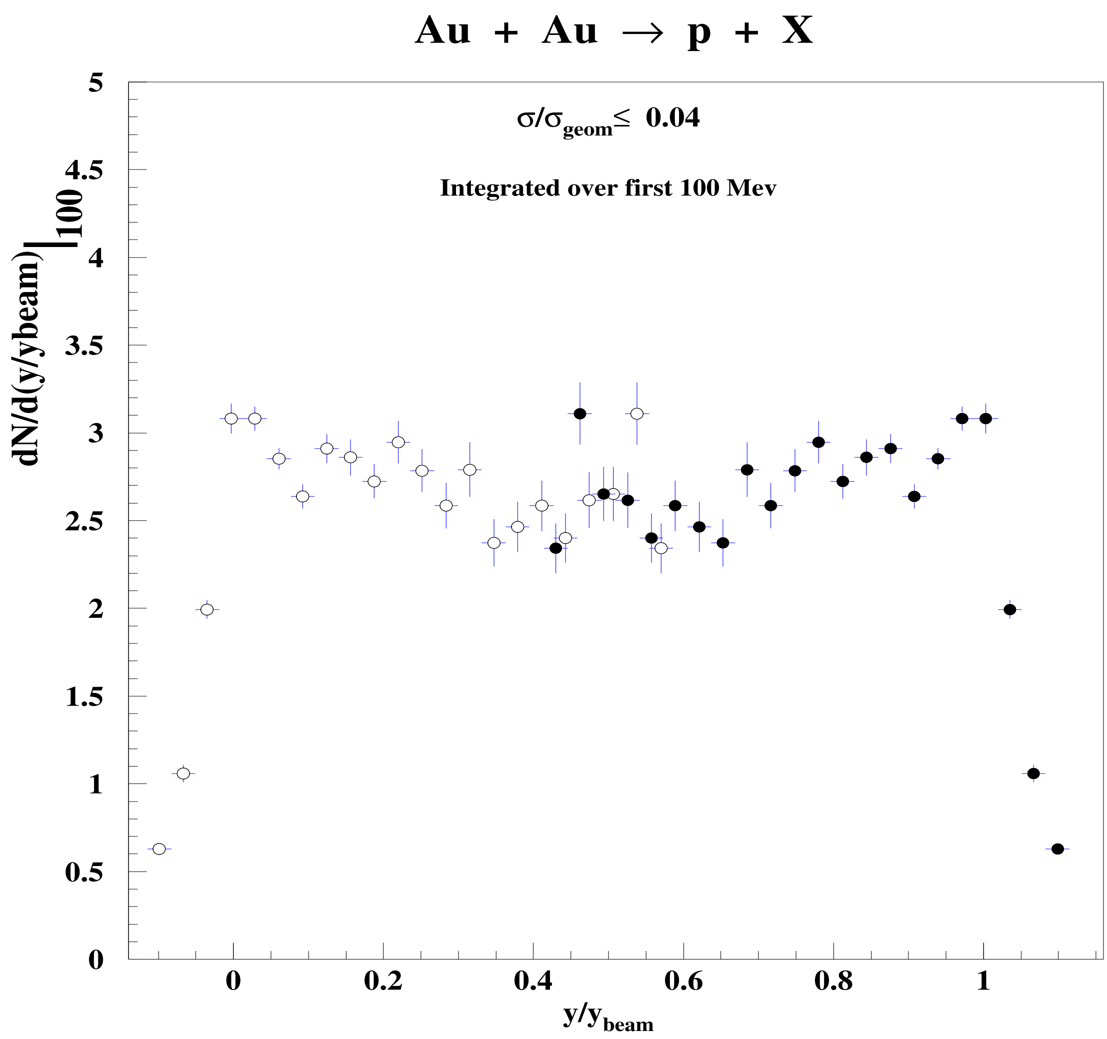

Figure 3.14: Integration over the first 100 MeV/c in p_t for proton spectra , at 4% centrality, down to a rapidity of 1.4. Closed symbols are measurements, open symbols are the measurement's reflection.

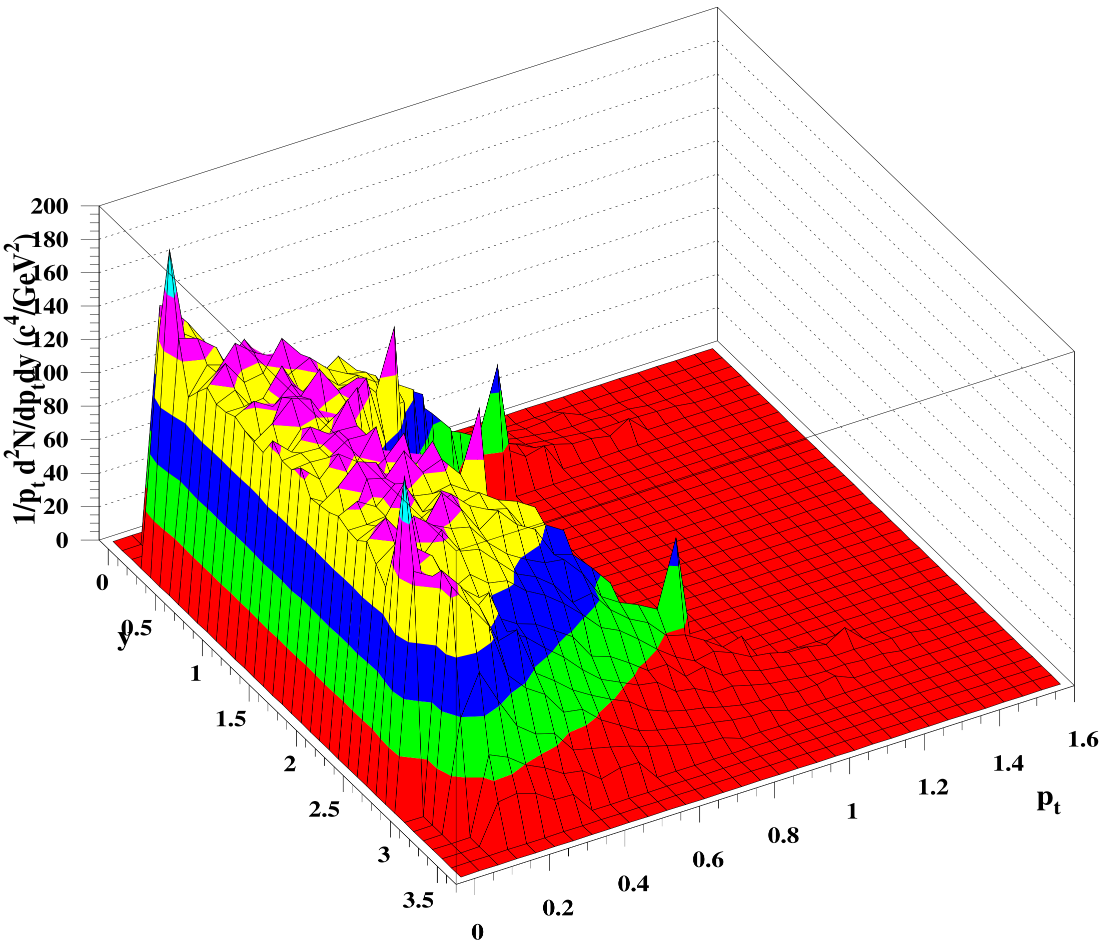

Figure 3.15: Three dimensional view of the proton phase space distribution. All data have been reflected across mid-rapidity.

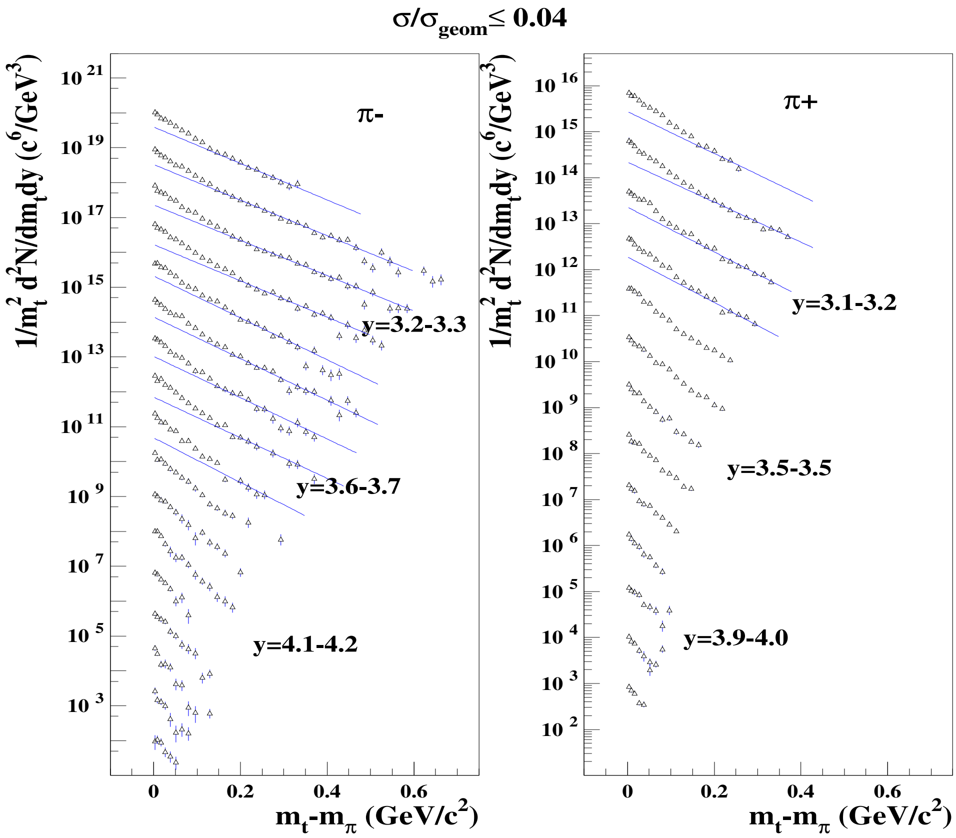

Figure 3.16: Measured pion spectra in Au + Au collisions at 10.8 GeV/c and a centrality of 4% of the geometric cross section.

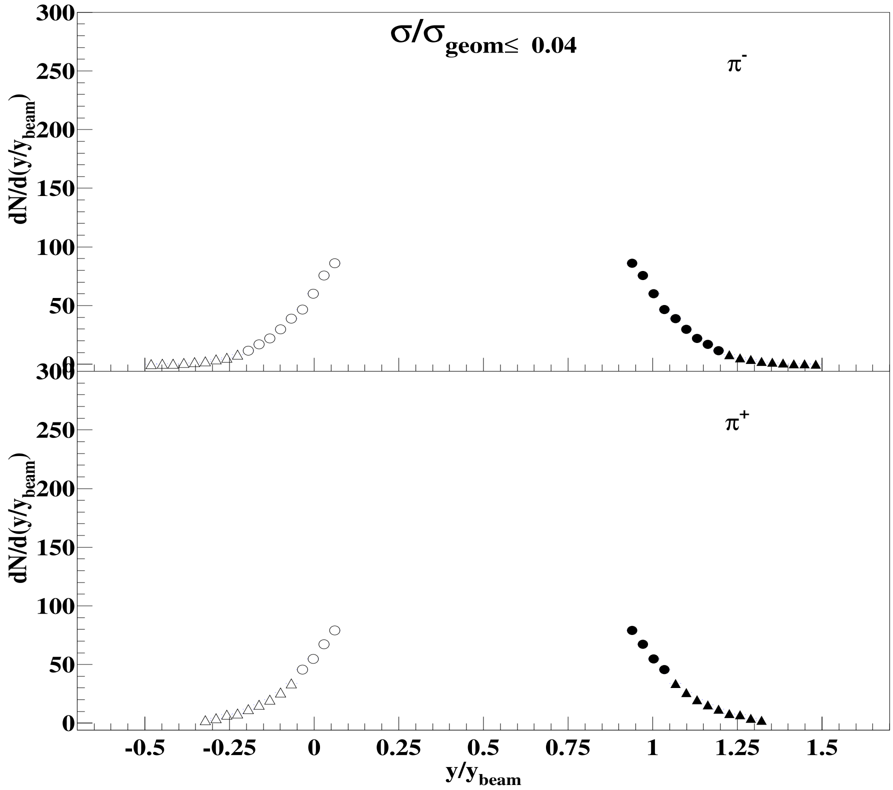

Figure 3.17: Measured charged pion rapidity density in Au + Au collisions at 10.8 GeV/c and 4% inclusive centrality. Circles represent those rapidity bins where a second hot component can be deduced from the data, triangles are those bins where only a single component is measured.

Chapter 4

Data Analysis

The effort to understand the universe is one of the very few things that lifts human life a little above the level of farce, and gives it some of the grace of tragedy.

–Steven Weinberg

In this chapter we strive to understand some of the features of the proton and pion spectra. We parameterize the transverse (m_t) and longitudinal (y) shape of the spectra and investigate the development of this shape as a function of transverse energy (collision violence). The "stopping" will be investigated via the rapidity density of protons. Pion data will be examined with particular emphasis on low p_t phenomena, and its possible relation to baryonic decays. Additionally, we discuss the experimental limitations on the precision of the spectra of promptly emitted particles via the irreducible effects of hyperon decays.

4.1 Proton Distributions

Of central importance in heavy ion collisions is the ability to understand to what extent the nuclear matter has been compressed and heated. These parameters depend critically upon the degree of stopping achieved in the collisions. Since at AGS energies the production of nucleon/anti-nucleon pairs is small [11, 12], the final state nucleon distribution is the most direct probe of stopping power. For Si beam data, it was found that the rapidity densities of many particle species could be successfully reproduced by a transversely and longitudinally expanding thermal source [49]. This model well reproduced the transverse mass spectra at mid-rapidity for all particle species studied (pions, kaons, protons and deuterons). The monotonic increase of temperature parameter with mass was attributed to a single underlying collective flow parameter. The rapidity densities for pions, kaons, lambdas, and deuterons emitted from Si+Al collisions were well fit by the assumption of a common longitudinal expansion velocity. The proton rapidity spectrum was not well fit by the model. There the experimental measurement showed a much broader rapidity spectrum than the model. This effect was attributed to partial transparency.

At the time of this writing, the *only* finalized singles spectra for Au+Au reactions measured by E877 are those for protons and pions. Our neighboring experiments (E891 and E866) have only published final results for Lambda hyperon production. Thus, there is insufficient data available to test and determine the parameters of the flowing thermal model. However, we can compare the proton and lambda rapidity widths and determine whether the Au+Au system comes closer to achieving full stopping than Si+Al.

4.1.1 Spectral Shapes

Simple Fireball Model

Arguably, the simplest and most intuitive of models is the isotropic thermal fireball model discussed in appendix 1. Although this model failed to reproduce the data measured for Si+Al collisions, it serves as a natural first test of our heavy system data. The model contains a single free parameter, the system temperature T, and serves to predict the spectral shape both longitudinally and transversely. Operationally, it is simplest to fit the spectra in each rapidity slice to the functional form:

$$\frac{1}{m_t^2}\frac{d^2N}{dm_t dy} = \frac{A_B(y)}{m} exp\left(-\frac{(m_t - m)}{T_B(y)}\right), \tag{4.1}$$

while allowing the temperature, $T_B(y)$, and amplitude, $A_B(y)$, parameters to vary freely. The model is then tested by examining the rapidity dependence of the two parameters.

Figure 4.1 shows the $T_B(y)$ result obtained from the proton spectra shown in fig 3.11 along with the best fit to the functional form $T_B(y) = T_0/cosh(y - y_{cm})$, appropriate for an isotropic thermal source. The observed temperatures follow the $sech(y - y_{cm})$ function well for rapidities above 2.45 for a characteristic temperature $T_0 = 260.51 \pm 1.08$. This can be contrasted with the result for Si beam in which the temperature parameters fell more steeply with increasing rapidity than expected for an isotropic fireball. Below

y=2.45 the temperature parameters deviate markedly from the $cosh^{-1}$ dependence tending toward dramatically high values near mid-rapidity. Plainly interpreted, this is first evidence for the failure of the isotropic fireball. As noted in Chapter 3, the measurement of $\frac{dN}{dy}$, relies upon an extrapolation function to complete the integral of the double differential cross section over all m_T. The failure of the expected rapidity dependence of the thermal parameterization, brings into question the use of a thermal Boltzmann as the extrapolation function. Whenever an extrapolation function is invoked some fraction of the $\frac{dN}{dy}$ integral will come from measurement, and is therefore correct, while the rest relies upon the validity of the extrapolation. Figure 4.2 shows the fraction of the $\frac{dN}{dy}$ integral would result from using the temperature parameters of Figure 4.1. This fraction is highest in that place where we see drastic rises in the slope parameter hinting that the Boltzmann spectrum extrapolation for these bins is invalid. Fortunately the AGS features *two* dedicated heavy ion, high resolution, spectrometers with complementary phase space coverage. The E866 experiment features rapidity coverage of approximately one unit about y_{mid} and can be consulted for guidance with regards to the high p_t character of the spectra for the bins in question.

In fig 4.3 proton spectra for $y = 2.3$ from this analysis are shown with an overlay of preliminary results from E866. One clearly sees a 'shoulder-arm' structure to the spectrum which again contradicts the naive model. This shape distortion was observed by E866 to be strongest [52] near mid rapidity and is often cited as evidence for radial flow effects [53]. Also shown in the figure are the extrapolations suggested by each measurement. Clearly extra-

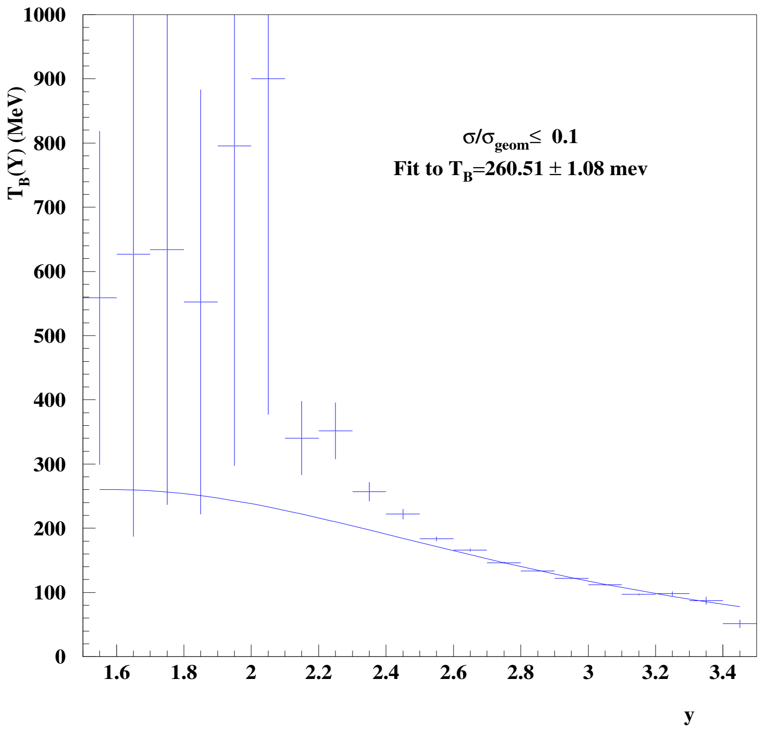

Figure 4.1: Rapidity dependence of T_B fit over all measured data. The solid line represents a fit to $T_0 sech(y - y_{cm})$, as would be expected by an isotropic fireball.

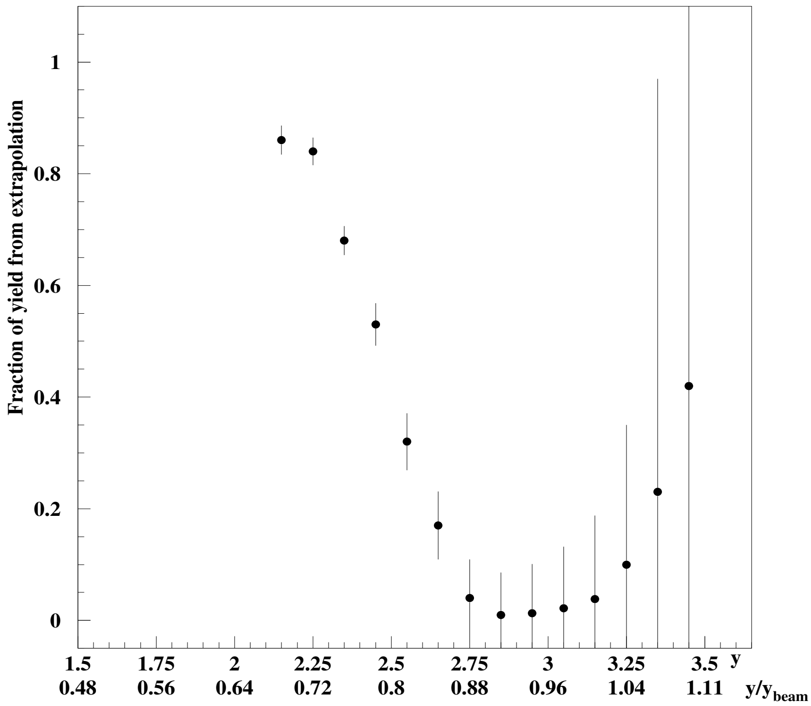

Figure 4.2: Fraction of proton yield in each rapidity bin that results from extrapolation of measured slope parameters.

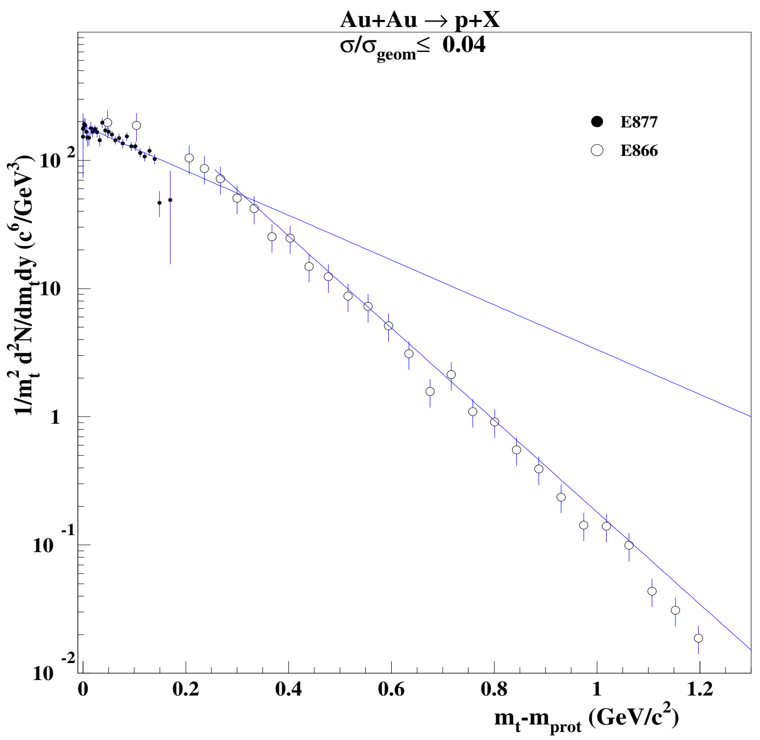

Figure 4.3: Proton spectra, $1/m_t^2 \times d^2N/dm_t dy$, for $y = 2.3$ from this analysis with an overlay of results from the AGS experiment E866. Also shown are the extrapolations suggested by each measurement.

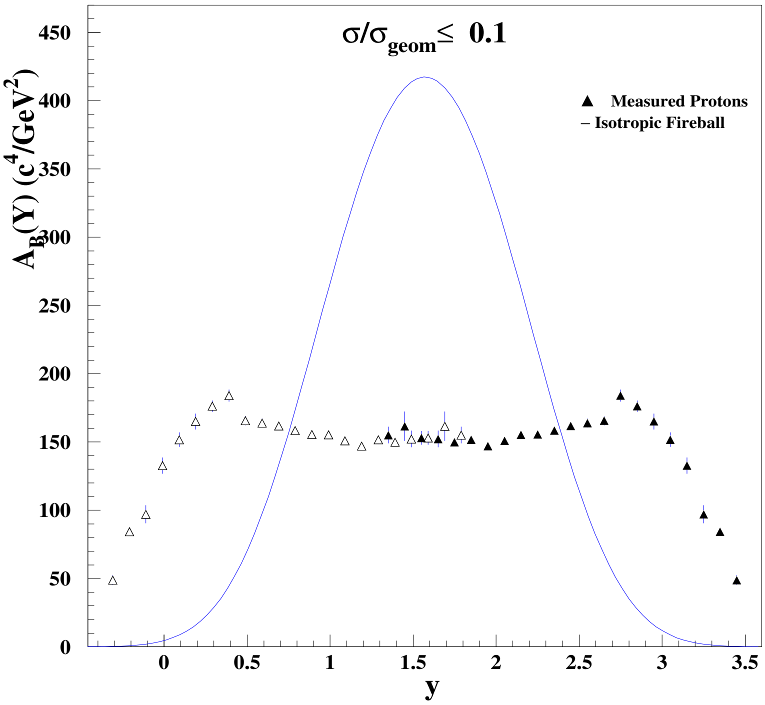

Figure 4.4: Rapidity dependence of A_B well below mid-rapidity. The solid line represents the prediction of an isotropic fireball.

polations in our lowest rapidity (narrowest acceptance) bins using the apparent temperature parameters will drastically overestimate the yield. We will only quote measurements for $\frac{dN}{dy}$ in those rapidity bins for which more than half the integral comes from the measured region, *i.e.* $y > 2.4$.

Shown in figure 4.4 are the results of the Boltzmann fit for the amplitude, A_B, as well as the prediction of the isotropic thermal model. As opposed to T_B, determination of the amplitude is insensitive to the fact that we have a limited

Rapidity	$\chi^2/ndof$
2.45	1.11
2.55	1.23
2.65	1.21
2.75	1.08
2.85	1.01
2.95	1.12
3.05	1.34
3.15	1.34
3.25	1.12
3.35	1.52
3.45	2.84

Table 4.1: Chi squared per degree of freedom for fits of the spectra, at a centrality of 10%, to a Boltzmann parameterization.

---

p_t range at low rapidities. The amplitude coefficients directly violate the naive model. We thus rule out the isotropic thermal fireball model. It should be noted, however, that although the rapidity dependence of the fit parameters is dramatically different than the simple prediction, the functional form does provide a quite reasonable fit to the spectrum. Collected in table 4.1 are the χ^2 values for the fits. We will thus later use such fit results as a convenient and compact way of summarizing the proton spectra. Specifically, we present

dN/dy and $T_B(y)$ as a spectral summary. Complete spectra for every particle species and centrality bin may by found in the Appendix.

Centrality Dependence

The data can now be integrated over transverse mass, using the measurement where available and extrapolations to $p_t = 0$ and/or $p_t \to \infty$ following the Boltzmann fits, to produce the rapidity distribution dN/dy. Owing to the deadened region in the tracking chambers, the acceptance does not extend to $p_t = 0$ at beam rapidity. For these rapidities we have used a two-component Boltzmann fit in our low p_t extrapolation. Figure 4.5 shows the measured (and reflected) $dN/d(y/y_{beam})$ versus y/y_{beam} for Au+Au collisions for a variety of centrality slices. Centrality bins are labeled by percentage. A centrality percentage is assigned to each bin in PCAL transverse energy by calculating the fraction of collisions that produce equal or greater E_T. Evident in the Figure is a strong centrality dependence of the proton spectra. Although it is well understood that cuts on neighboring tiny fractions of centrality do not represent cuts on distinct impact parameters or event classes, it is clear that the proton spectra do evolve significantly with centrality and that indeed we are increasing the mean violence and mean number of participating protons.

As noted previously, Si+Al results showed that the proton spectra rapidity distribution was roughly 1.5× broader than the Lambda, a nearly equal mass particle. Clearly the Lambda results from strong interactions and can be considered in a sense as indicative of a true participant particle since a strong interaction is required for their production. Although it is beyond the capabil-

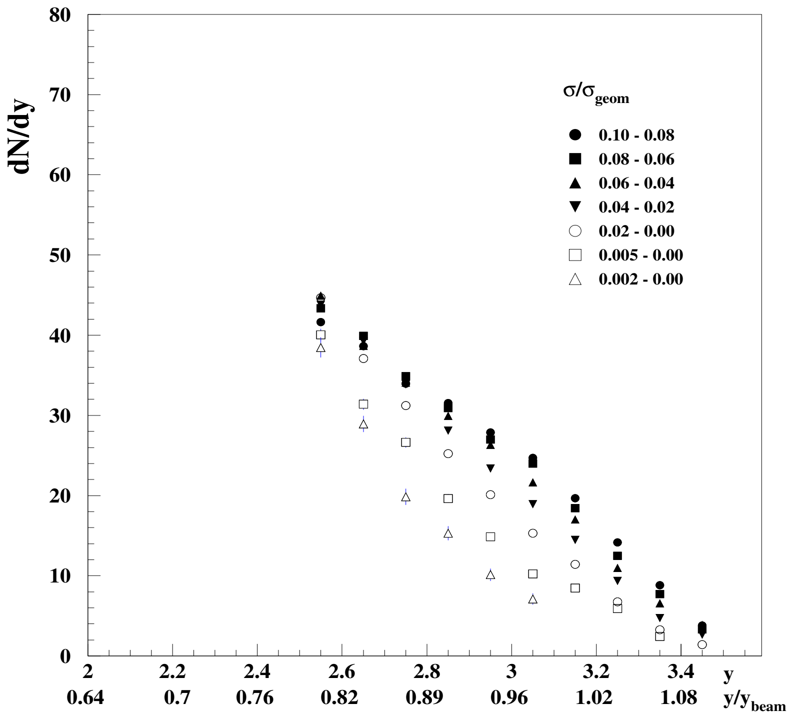

Figure 4.5: Centrality dependence of the proton rapidity density dn/dy.

ity of our experiment to measure the Lambda rapidity width, published results already exist from the E891 experiment. These results indicate a sigma of the nearly Gaussian Lambda rapidity distribution of 0.62 units, comparable to the result for Si+Al. In the tightest centrality bin, our proton rapidity spectrum has an apparent width of 0.7 units, much closer to that of the Lambda than was true for the light system. To the extent that the previous result was indicative of partial transparency, this result shows nearly complete stopping.

Plotted in Figure 4.6 is the measured Boltzmann parameter for rapidity bins above y=2.4. The different symbols in the plot indicate cuts on centrality identical to those studies for $\frac{dN}{dy}$. Contrary to the proton rapidity spectrum which shows a strong dependence upon centrality the temperature parameters show no systematic trend with centrality. This indicates that the development with centrality represents a continual movement for protons across rapidity bins, likely due to increased numbers of principle and secondary interactions, but that the result of these additional interactions on former spectators is the same as experienced by other participants. This development must be reflected in A_B, a variable which we measure over the entire phase space.

To put the A_B measurements into a somewhat more physically intuitive representation, we choose to present a truncated integral of the double differential cross section over the lowest 100 MeV/c of p_t . The result of this severely truncated integral is nearly independent of temperature parameter and yields the same units as $\frac{dN}{dy}$. Figures 4.7- 4.12 show this quantity for six centrality bins previously analyzed. The shape of each spectrum is characterized by a mid-rapidity 'plateau' and beam rapidity 'wings'. The action imposed by

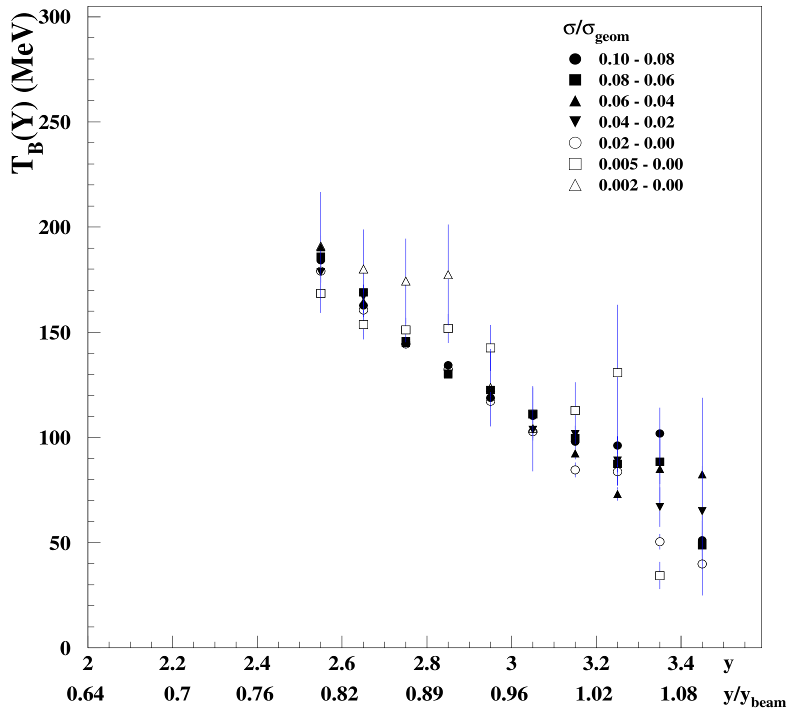

Figure 4.6: Centrality dependence of the proton inverse Boltzmann temperature parameter T_B.

the tight centrality cut, limiting the spectator region can be seen even more dramatically in this representation. With increasing tightness of the centrality cut, the 'wings' (representing fragmentation protons) decrease as the 'plateau' increases. We quantify this centrality dependence by calculating the spectral sum across both the mid-centrality 'plateau' region ($0.9 \leq y \leq 2.5$) and the spectator 'wings'. Figure 4.13, shows the development of each of these quantities with centrality.

We show in Figure 4.14 a comparison of our measured $\frac{dN}{dy}$ for the 4% inclusive centrality bin with the failed thermal model, the Si+Al result and the cascade code RQMD. We have plotted the functions vs y/y_{beam} to account for the difference in incident momentum of the Si beam experiments and that of Au. Additionally (and correctly) the vertical scale has been multiplied by the proper Jacobian (differential $= d(y/y_{beam})$). Clearly the result for the Au beam even at this limited centrality indicates more stopping in the heavier system.

Over most of the measured range the RQMD model does well in reproducing the measurement. The one exception is the lack of "bumps" in the data near beam and target rapidity. This difference is easily understood since the RQMD always disassociates the entire spectator region into individual nucleons. In the real case, many of the nucleons come out in clusters and although tracked, are not identified as free protons.

Finally, in an analogous fashion to Si+Al [49] we present the results of fitting the entire rapidity density, from data presented in this thesis as well as preliminary E866 data, to a longitudinally expanding thermal source. Individual isotropic thermal sources are superimposed upon each other within some rapidity interval $[-\eta_{max}, \eta_{max}]$, i.e.

$$\frac{dN}{dy} = \int_{-\eta_{max}}^{\eta_{max}} d\eta \frac{dN_{iso}(y-\eta)}{d\eta} \tag{4.2}$$

This is done separately for protons, Fig 4.15, and pions, Fig 4.16. Values which give the best fits are $\eta_{max} = 1.292 \pm 0.00135$ for protons and $\eta_{max} = 1.058 \pm 0.0036$ for pions. Taken at face value, the higher η_{max} for the protons would indicate incomplete stopping. As noted previously, however, the proton width spectra show a strong dependence upon centrality even with very tight centrality cuts. Thus, it would be desirable to perform the fit using the tightest centrality cuts. E866 data at this centrality is not available, however, since the tails of the distribution have the most influence on the η_{max} parameter we nonetheless perform the fit to E877 0.2% centrality and E866 4% centrality, Fig 4.17. In this case we determine $\eta_{max} = 1.102 \pm 0.0088$, which is nearly consistent with the pion result. Thus, we find that protons are fit with nearly equivalent longitudinal flow velocities and conclude that proton stopping has finally become complete. It is interesting to note that the multi-specie best fit value for Si+Al was $\eta_{max} = 1.15$, similar to the result just found. This analysis did *not* include a fit to the proton rapidity density since clear transparency was observed for the smaller system.

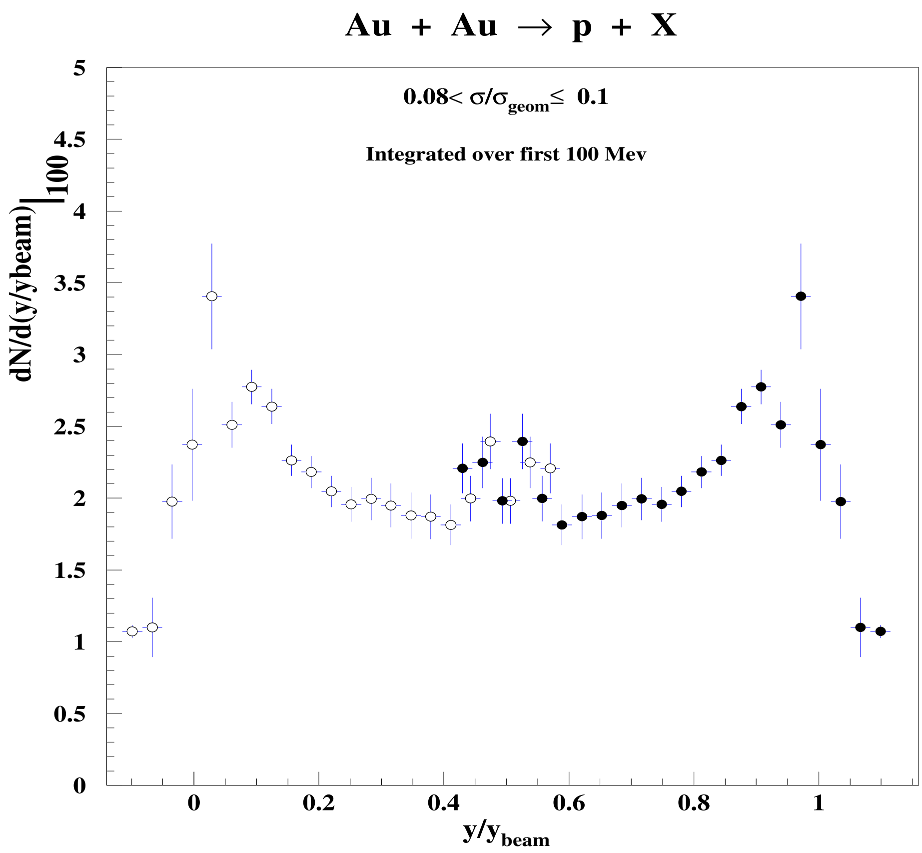

Figure 4.7: Integration over the first 100 MeV/c in p_t for proton spectra , at a centrality of 10-8%, down to a rapidity of 1.4. Closed symbols are measurements, open symbols are the measurement's reflection.

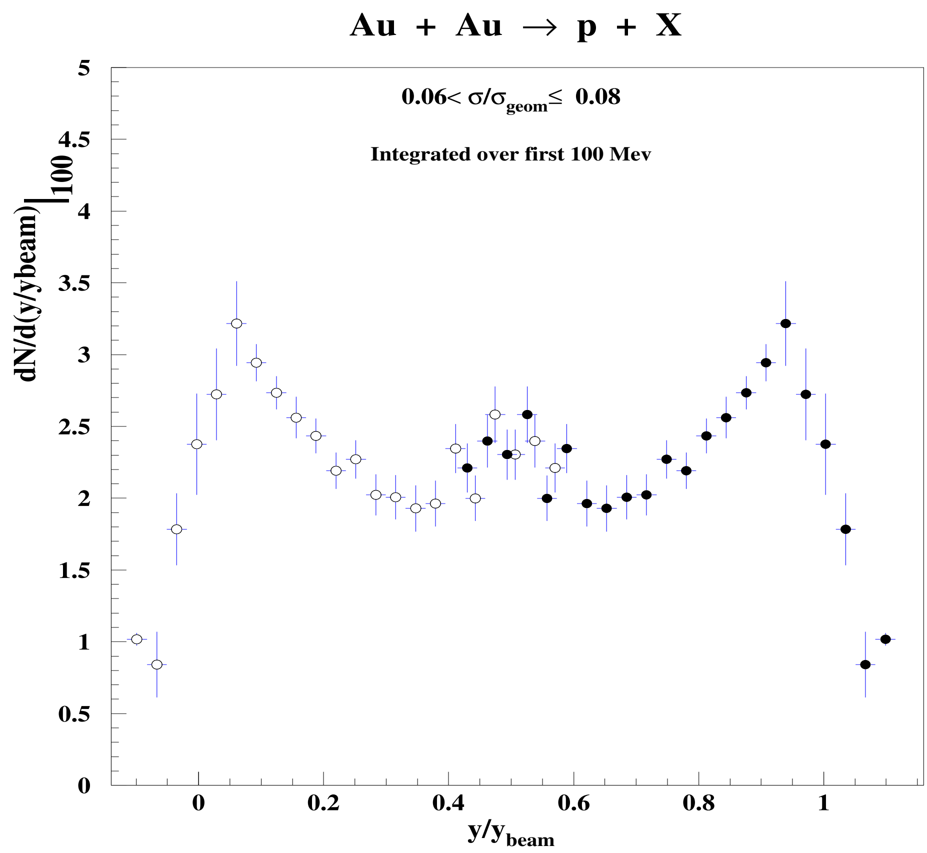

Figure 4.8: Integration over the first 100 MeV/c in p_t for proton spectra , at a centrality of 8-6%, down to a rapidity of 1.4. Closed symbols are measurements, open symbols are the measurement's reflection.

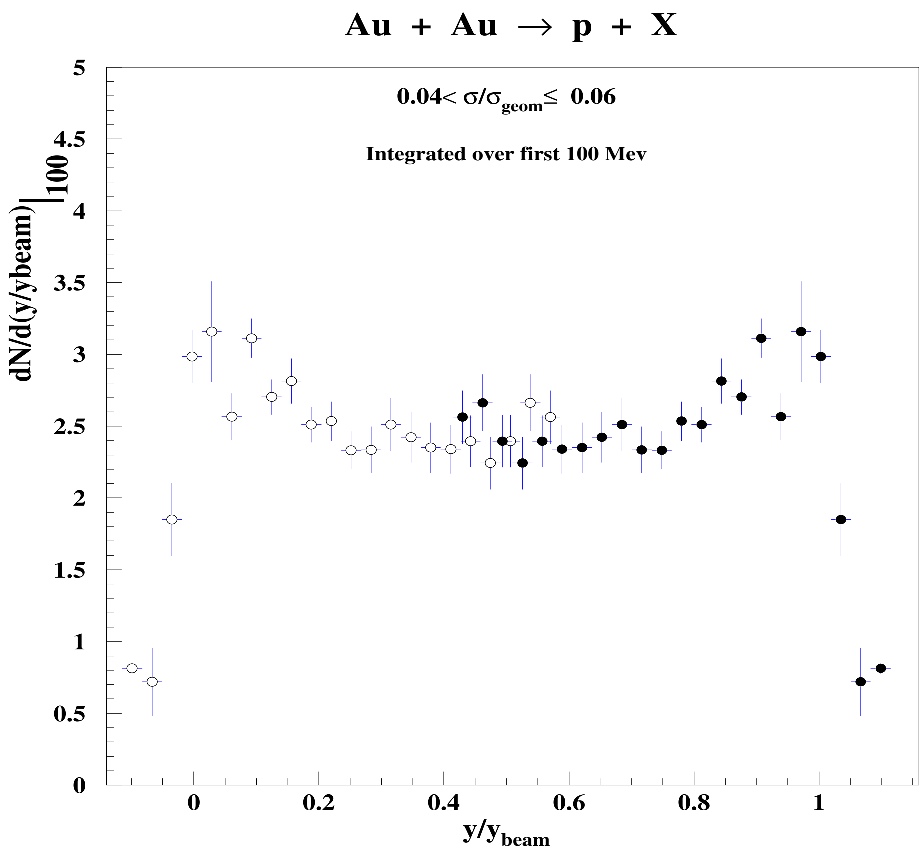

Figure 4.9: Integration over the first 100 MeV/c in p_t for proton spectra , at a centrality of 6-4%, down to a rapidity of 1.4. Closed symbols are measurements, open symbols are the measurement's reflection.

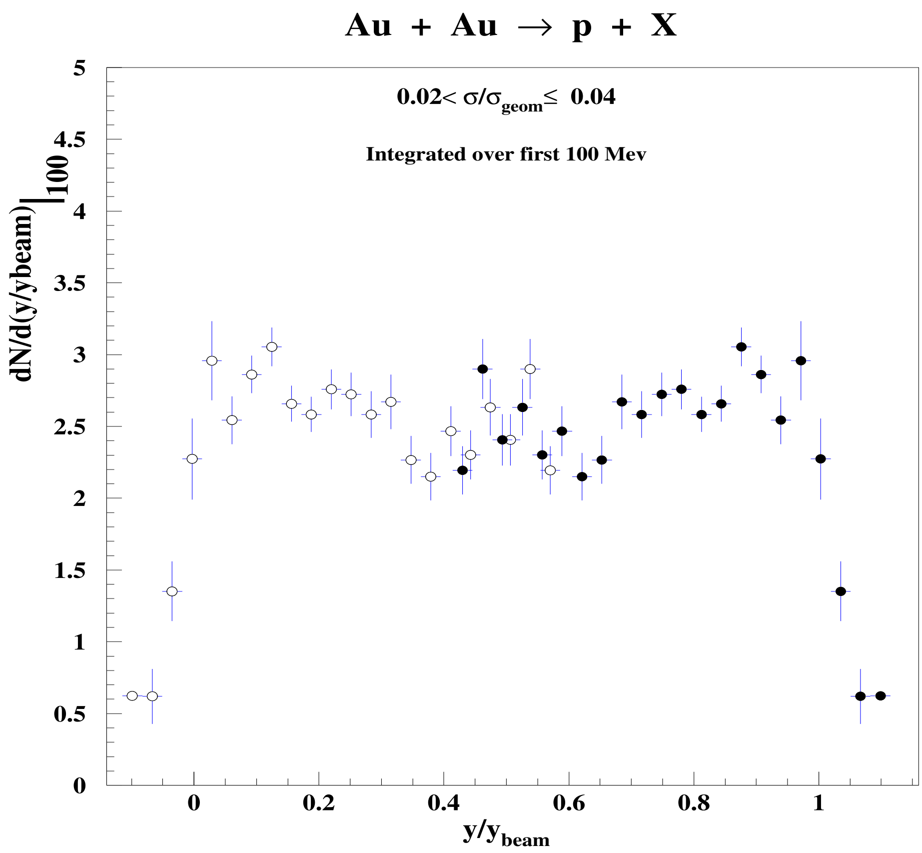

Figure 4.10: Integration over the first 100 MeV/c in p_t for proton spectra , at a centrality of 6-2%, down to a rapidity of 1.4. Closed symbols are measurements, open symbols are the measurement's reflection.

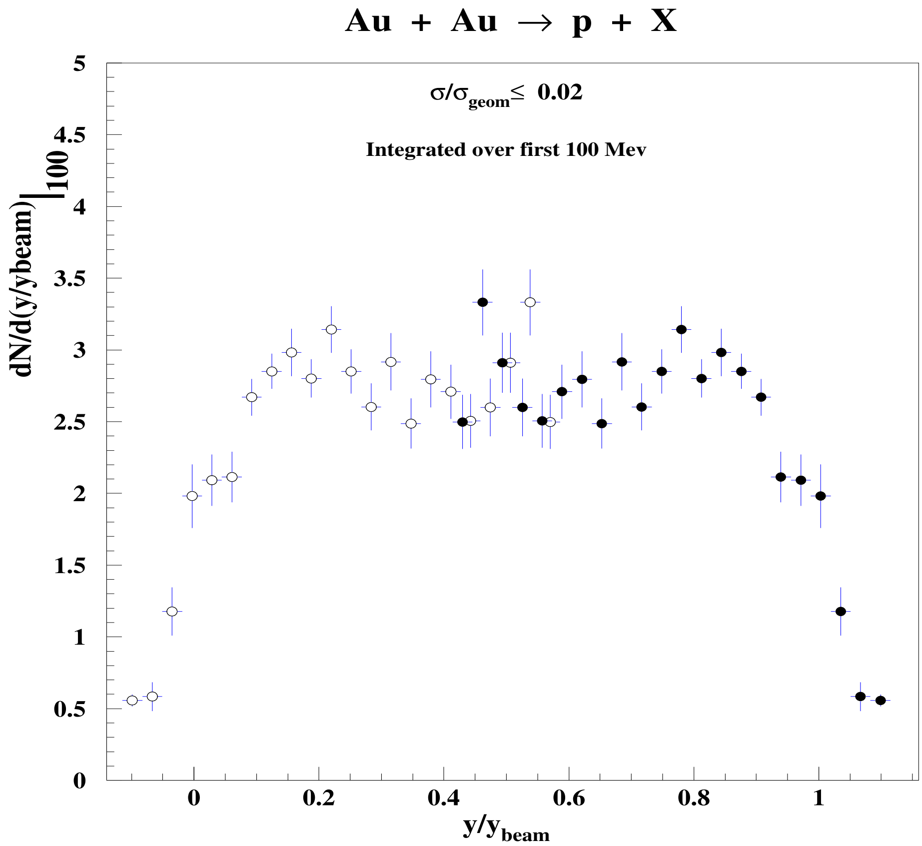

Figure 4.11: Integration over the first 100 MeV/c in p_t for proton spectra , at 2% centrality, down to a rapidity of 1.4. Closed symbols are measurements, open symbols are the measurement's reflection.

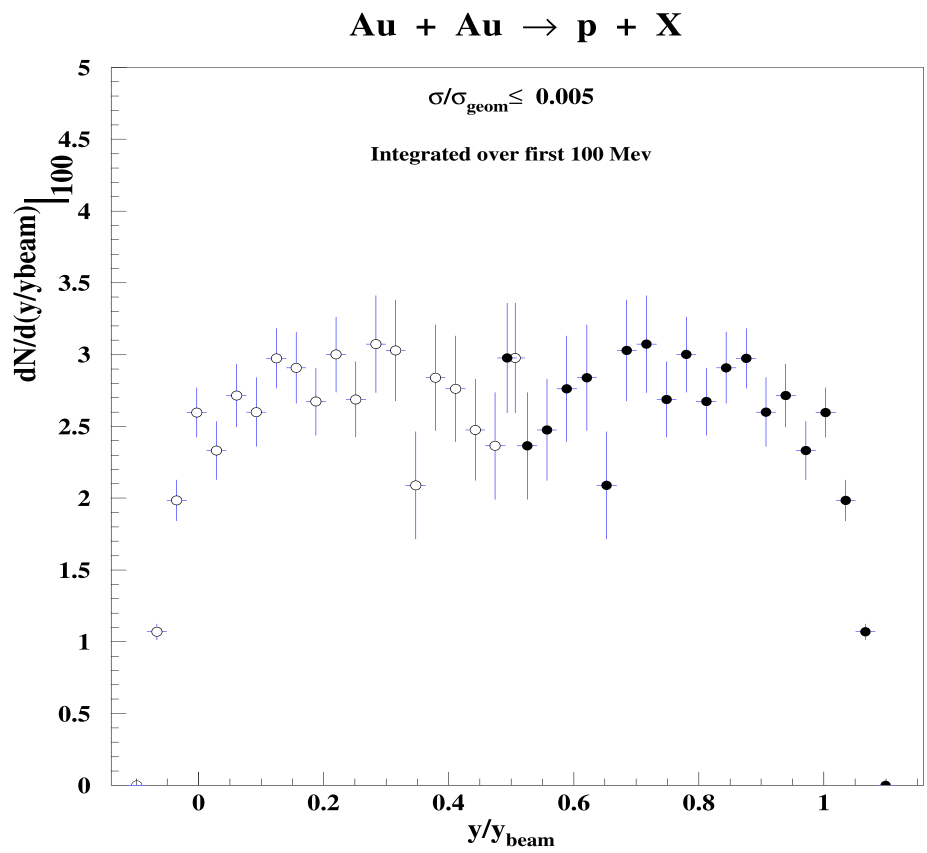

Figure 4.12: Integration over the first 100 MeV/c in p_t for proton spectra , at 0.5% centrality, down to a rapidity of 1.4. Closed symbols are measurements, open symbols are the measurement's reflection.

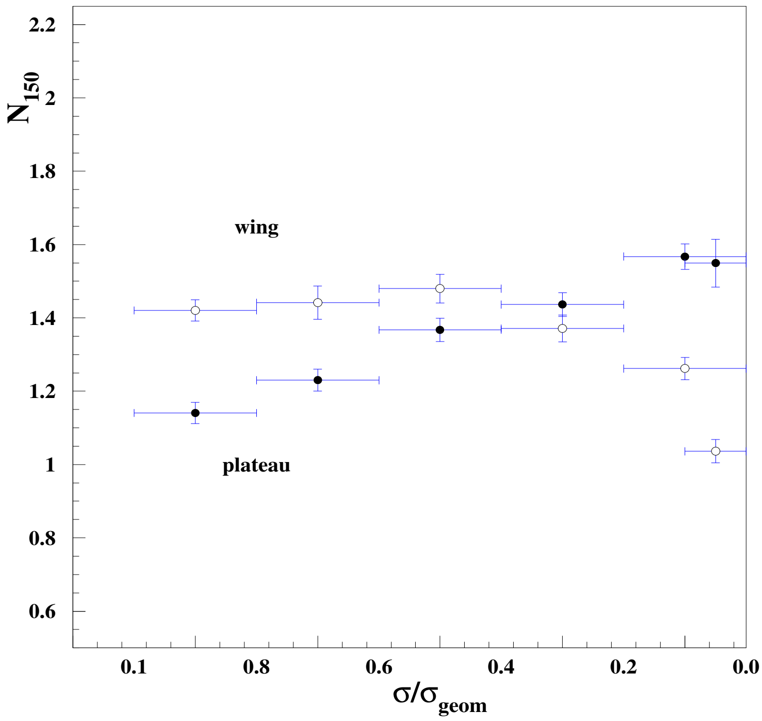

Figure 4.13: Centrality dependence of the 'plateau' and 'wing' structure (see text) of the integral over the first 100 MeV/c in p_t.

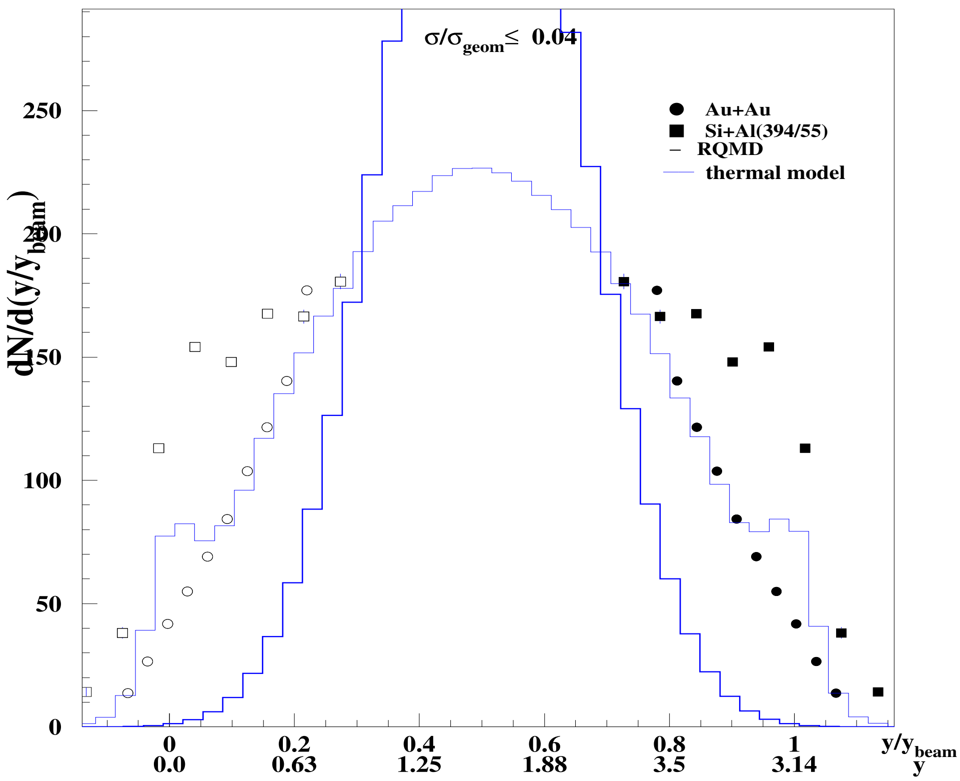

Figure 4.14: Measured proton rapidity density in Au + Au collisions at 10.8 GeV/c and 4% inclusive centrality compared to Si+Al, RQMD, and results of a thermal model.

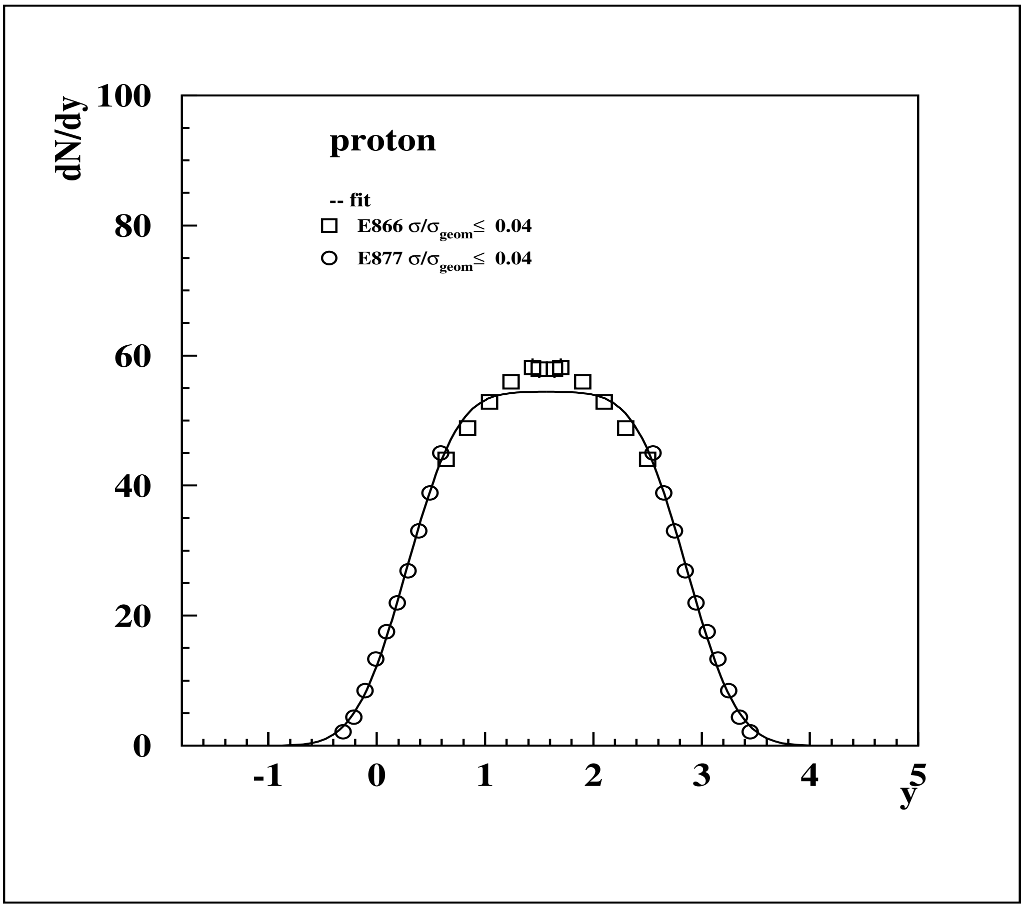

Figure 4.15: Measured proton rapidity density in Au + Au collisions from E877 and preliminary E866 results. The data is best fit by a longitudinally expanding thermal source with $\eta_{max} = 1.29$, as discussed in the text.

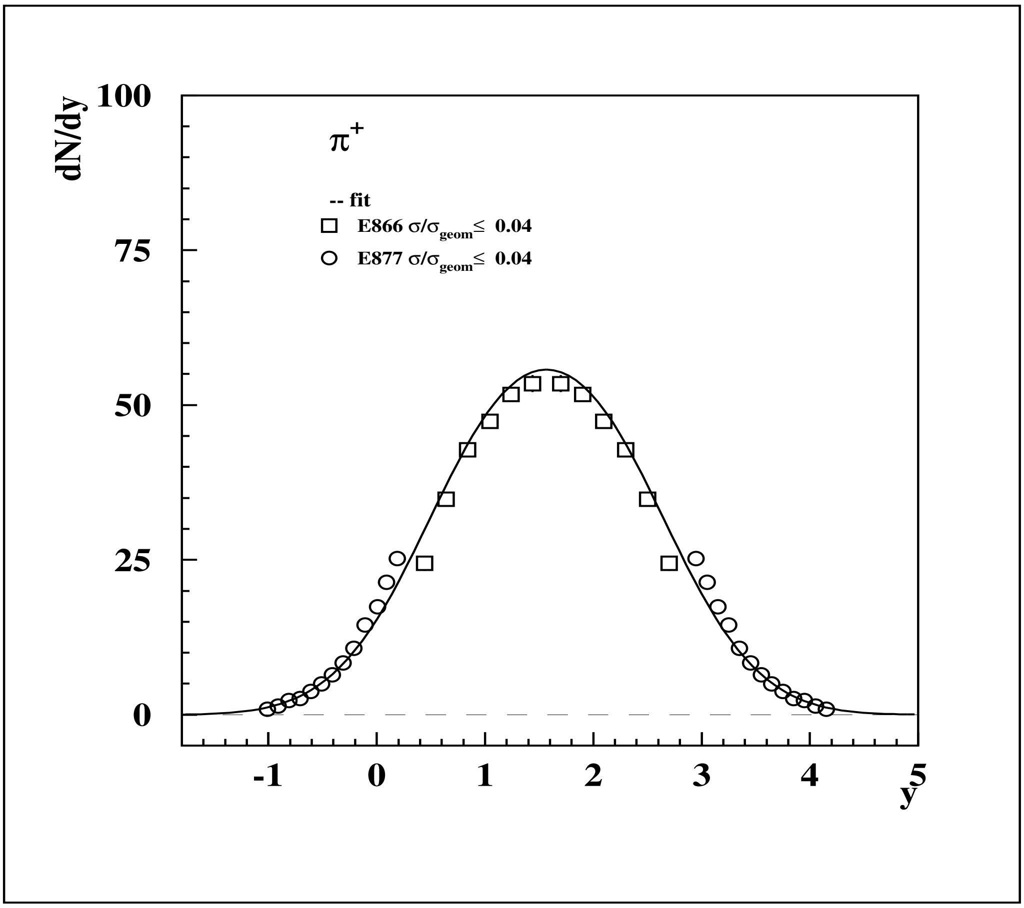

Figure 4.16: Measured pion rapidity density in Au + Au collisions from E877 and preliminary E866 results. The data is best fit by a longitudinally expanding thermal source with $\eta_{max} = 1.06$, as discussed in the text.

4.1.2 Hyperon contribution

Since the E877 tracking system uses the vector direction of the track downstream of the analyzing magnet and the *assumption* that the track originated at the target, it will suffer an irreducible background from weakly decaying particles. In this case, although the vector direction of the track downstream of the magnet is indeed correctly identified, the assumption of the target is incorrect. Thus the particle is labeled with the wrong momentum. Decay of the various hyperons is well documented [37] and is summarized in table 4.2.

For tracks with significant kinks, the error in momentum will be sufficient to result in the particle not falling into one of the defined $mass^2$ bands. Unfortunately, both pion and proton as hyperon decay products have reasonably large chances of passing our acceptance cuts if they fall geometrically within the acceptance of the spectrometer. The primary feeding channel is Lambda decay. This is a low Q value decay. The proton resulting from such a decay, especially at the high rapidities associated with our acceptance will suffer little deflection as compared to the initial Lambda direction. As such, its magnetic analysis will be nearly as accurate as if it came from the target, resulting in a false source of "protons".

The pion from the Lambda decay does suffer a significant kink. However, since the pion is the lightest meson, its velocity is often near the speed of light and thus, its mass resolution is overwhelmingly dominated by contributions from the velocity measurement. Thus, even though the momentum measurement may be significantly in error, the $mass^2$ is still within the cut.

We have estimated the level of contamination of our proton (and pion) spectra by using a modified version of the acceptance calculation routine. The modified version simply allows the particle's origin to be away from the interaction point (as a result of decay in flight). Analysis then proceeds normally.

Our Monte Carlo source of hyperons was based upon a parameterization of the Lambda yield measured by AGS experiment E891 [51]. Shown in Figure 4.19 is the ratio of hyperon daughter protons to the total measured proton yield as a function of rapidity. The fraction of protons from hyperon decay is maximal at y=2.2 and has a value of 14%, and is minimal at y=3.45 with a value of 1%. In the limit of zero Q value, the daughters of any decay have identical velocity to the parent. Since both the Lambda mass and its primary momentum distribution are similar to that of the proton, it does not distort the proton spectrum significantly. Shown in Figure 4.18 is the primary Lambda $\frac{dN}{dy}$ spectrum, the spectrum of $p\pi^-$ decays (lower by the branching ratio) and the simulation of its contribution to the proton $\frac{dN}{dy}$. As can be seen, the probability of a decay Lambda reconstructing as a proton is nearly one at the highest rapidities and significantly lower as the rapidity and momentum of the parent decrease.

It is in general a poor practice to correct one's own data using the measurements of another . Since the hyperon contamination to the protons is small, we ask the reader to consider that Figure 4.18 is an estimate of how much background is likely to be in the measured spectrum.

In the case of the pion from Lambda decay, the velocity will be similar to that of the parent which means that its momentum will be significantly

Specie	**Mass**(GeV/c^2)	**Decay mode**	**Branching ratio**	**q (GeV/c)**	**Yield**
Λ	1.1157	$\Lambda \rightarrow p + \pi^-$	0.639	0.101	16.7
Σ^+	1.1189	$\Sigma^+ \rightarrow p + \pi^o$	0.516	0.189	5.97
Σ^+	1.1189	$\Sigma^+ \rightarrow n + \pi^+$	0.483	0.185	5.97
Σ^o	1.1926	$\Sigma^o \rightarrow \Lambda + \gamma$	1.0	0.074	5.90
Σ^-	1.1974	$\Sigma^- \rightarrow n + \pi^-$	0.998	0.193	5.96
Ξ^o	1.3149	$\Xi^o \rightarrow \Lambda + \pi^o$	0.995	0.135	0.53
Ξ^-	1.3213	$\Xi^- \rightarrow \Lambda + \pi^-$	0.999	0.139	0.58

Table 4.2: Hyperon decay modes and their various decay parameters, yields are from the model RQMD.

---

smaller. Thus even a small overall population of Lambda decay pions will have a significant impact on the pion spectral shape. These effects are dealt with in more detail below.

4.1.3 Pions

Collisions at AGS energies are characterized by copious pion production. Pions have the dual virtues of a large interaction cross section, as well as a low mass, making them quick to thermalize and less sensitive to flow effects than other produced particles. The pion spectral shape in many systems and at various energies has consistently shown an excess of pions, with regards to a thermal distribution, at low p_t [42] . Indeed, it was shown in a study of the Si+Pb system at the AGS that pion spectra, together with a direct $\Delta^{++}(1232)$ reconstruction, could effectively be exploited to determine the freeze-out population of the delta resonance [40] .

Pion spectra are examined, as well as their related quantities such as slope parameter and rapidity density. Information regarding delta resonance population is inferred from the low p_t enhancement in the π^- system.

4.1.4 Pion Spectral Shapes

Charged pion spectra, for $\sigma/\sigma_{geom} \leq 0.1$, are presented in fig 4.20. A cursory glance is sufficient to realize that a single Boltzmann fit is a fruitless endeavor. There is an obvious enhancement, with respect to the high p_t tail, of low p_t pions. Indeed it is this enhancement that makes the π spectra a tool to measure the resonances [54]. Plotted on the same figure are Boltzmann parameterizations fit to the spectra over the range $0.3 < p_t < 0.6\mathrm{GeV}/c^2$. These can be examined in more detail in figure 4.21 in which the slope parameters are plotted as a function of rapidity for both charged pions. Also plotted are best fits of the data to an $T_0^{\pm}/cosh(y - y_{cm})$ parameterization yielding $T_0^+ = 210.03 \pm 3.12$ and $T_0^- = 220.22 \pm 3.20$.

In the lighter symmetric system, Si+Al, the two component nature of the pion spectra was attributed, both through direct reconstruction of $\Delta^{++}(1232)$ and through pion spectral analysis, to the delta resonance [39, 40]. The lesser signal to noise for direct $\Delta^{++}(1232)$ reconstruction has prevented a similar analysis (true pair yields are proportional to the multiplicity, false pairs to the square). However, we will pursue a nearly identical spectral shape analysis, albeit without the confirming evidence of a direct $\Delta^{++}(1232)$ reconstruction.

Prior to the Δ-driven shape analysis, however, several new features of the pion spectra must be understood. In Figure 4.20 it is apparent that in addition to both charged pions exhibiting a low p_T enhancement, the spectra also show a difference between the two charged states. The low p_t enhancement is significantly larger for π^- than for the π^+.

Shown in Figure 4.23 is the ratio of the measured π^- and π^+ m_T spectra for several rapidity bins with a 4% inclusive centrality cut. The ratio shows an increase of roughly 1.5X at the origin. Several obvious processes could contribute to this difference, here we will discuss the contributions of hyperon decay and Coulomb. Following the prescriptions of the preceding section, we have calculated the expected contribution to our spectra from the decay of the Lambda. Again using the E891 measurement as an input, we calculate the solid line in the figure as the predicted distortion due to this decay. Accounting for the 20% systematic error they quote in their measurement, this shows agreement with the measurement. Other sources of π^-/π^+ spectral shape differences clearly must exist (Coulomb will contribute). However, they will only be measurable by us IF their contribution is larger than the systematic errors in the background calculation. For the centrality bin shown, that is not the case.

Figures 4.28- 4.24 show the evolution of the ratio of the π^-/π^+ ratio measurements as a function of centrality for a number of exclusive bins. The E891 prediction for the Lambda contribution is also shown in each bin, however, the centrality dependence of the Lambda production has not been published by them. Thus, the comparison should only be used as a rough guide.

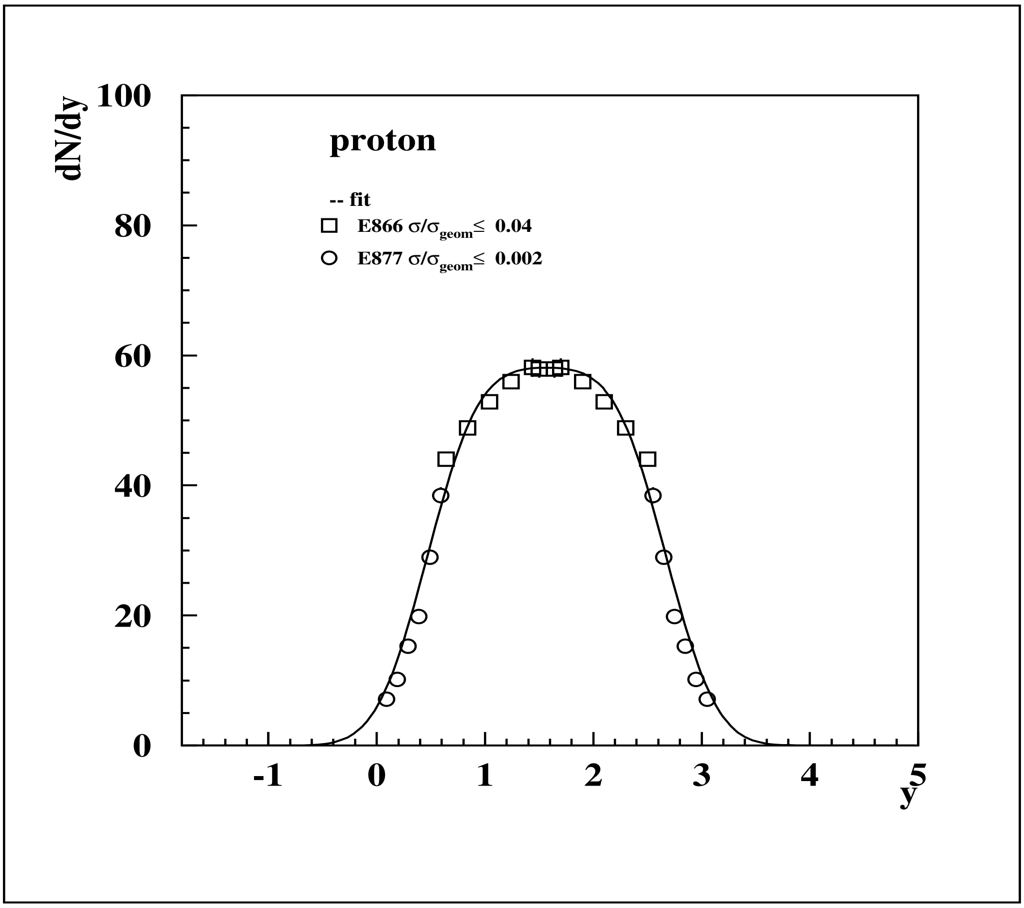

Figure 4.17: Measured proton rapidity density in Au + Au collisions from E877 and preliminary E866 results at centralities of 0.2% and 4% respectively. The data is best fit by a longitudinally expanding thermal source with $\eta_{max} = 1.29$, as discussed in the text.

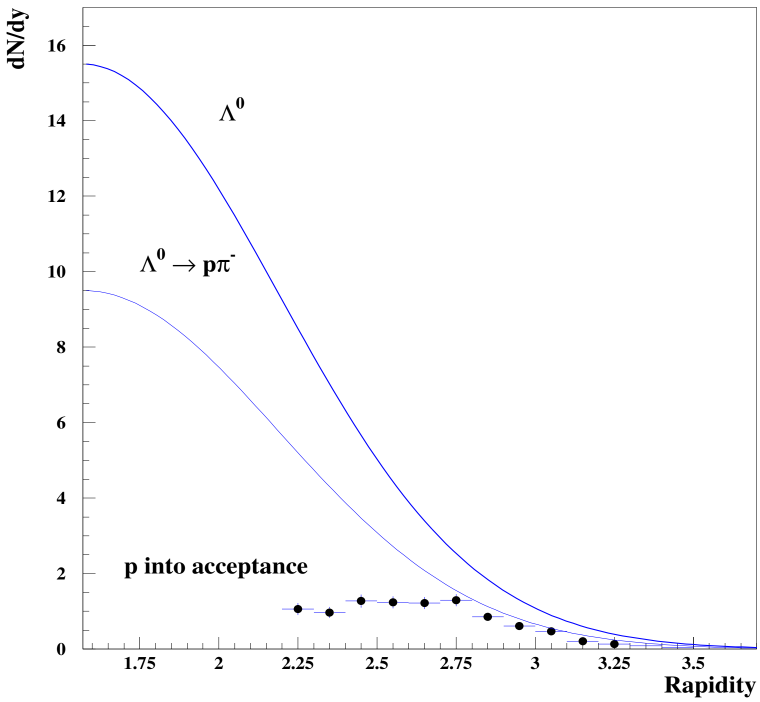

Figure 4.18: Rapidity distribution of protons from Λ decay, the dark solid curve representing lambda hyperons from all sources, the light line is the dark one multiplied by the 64% branching ratio for lambda decay into a proton and pion.

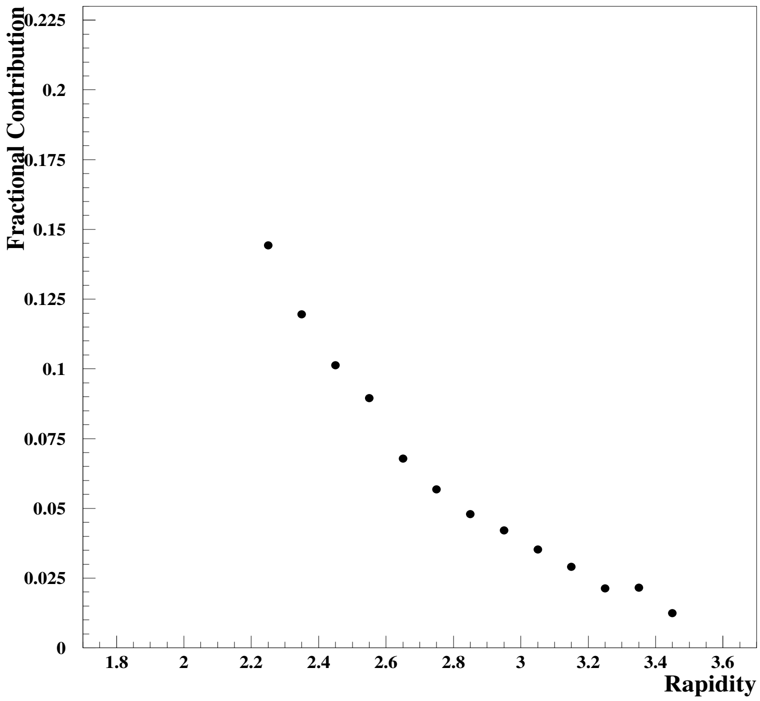

Figure 4.19: Fractional hyperon contribution to proton spectra as determined by Monte Carlo.

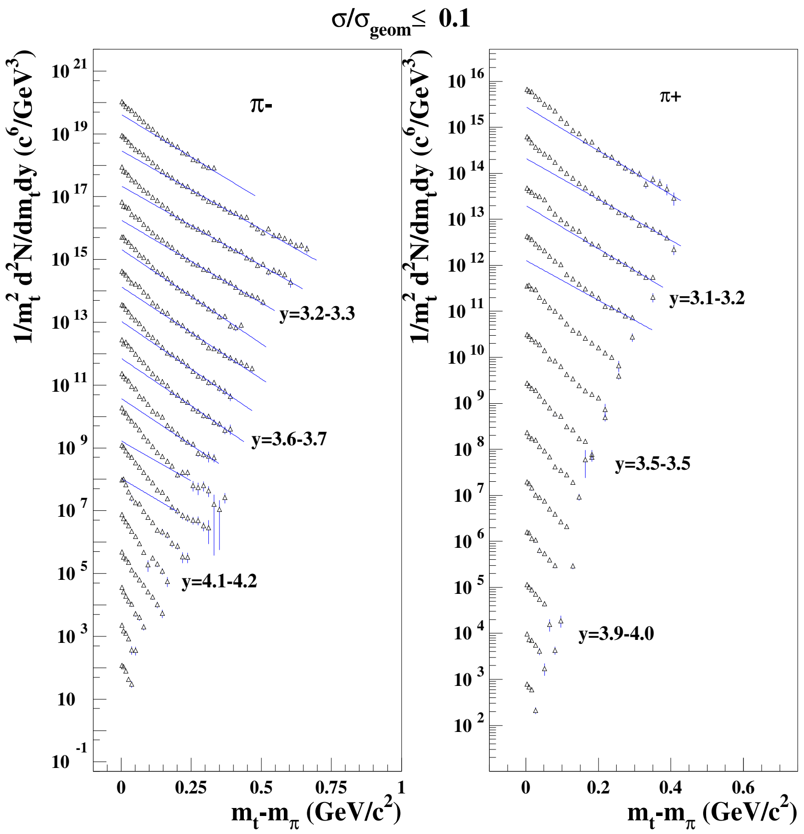

Figure 4.20: Measured charged pion spectra in Au + Au collisions at 10.8 GeV/c and 10% inclusive centrality.

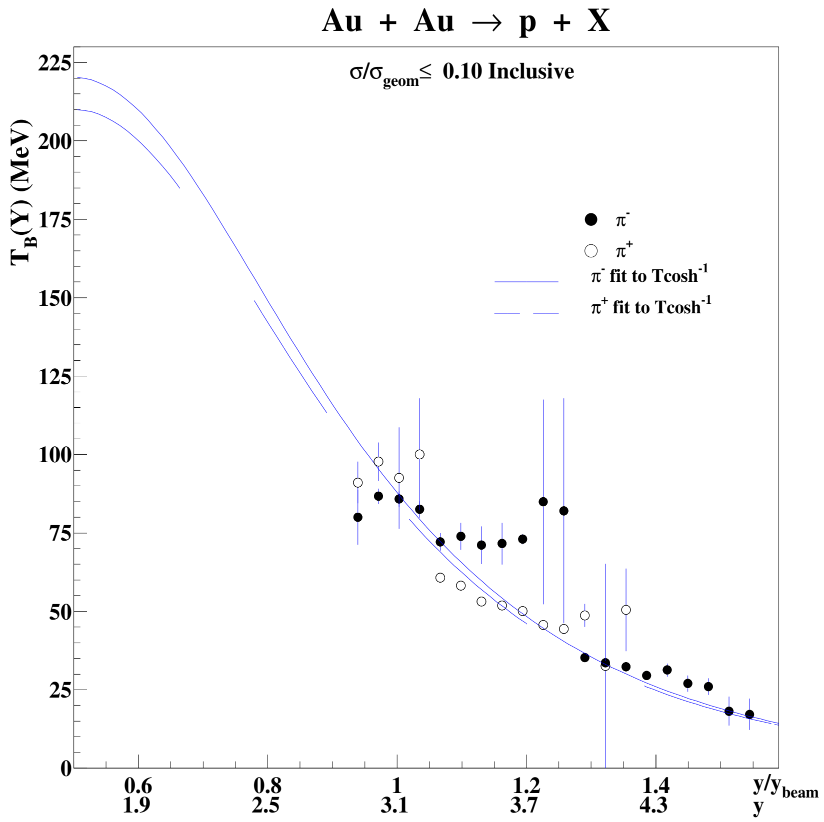

Figure 4.21: Measured π^- and π^+ temperature parameters fit to the hot component, when it can be deduced, in Au + Au collisions at 10.8 GeV/c and 10% inclusive centrality. Also shown are fits to the functional form $T_0/cosh(y-y_{cm})$, with $T_0 = 220.22 \pm 3.2$ for π^-, and $T_0 = 210.03 \pm 3.12$ for π^+.

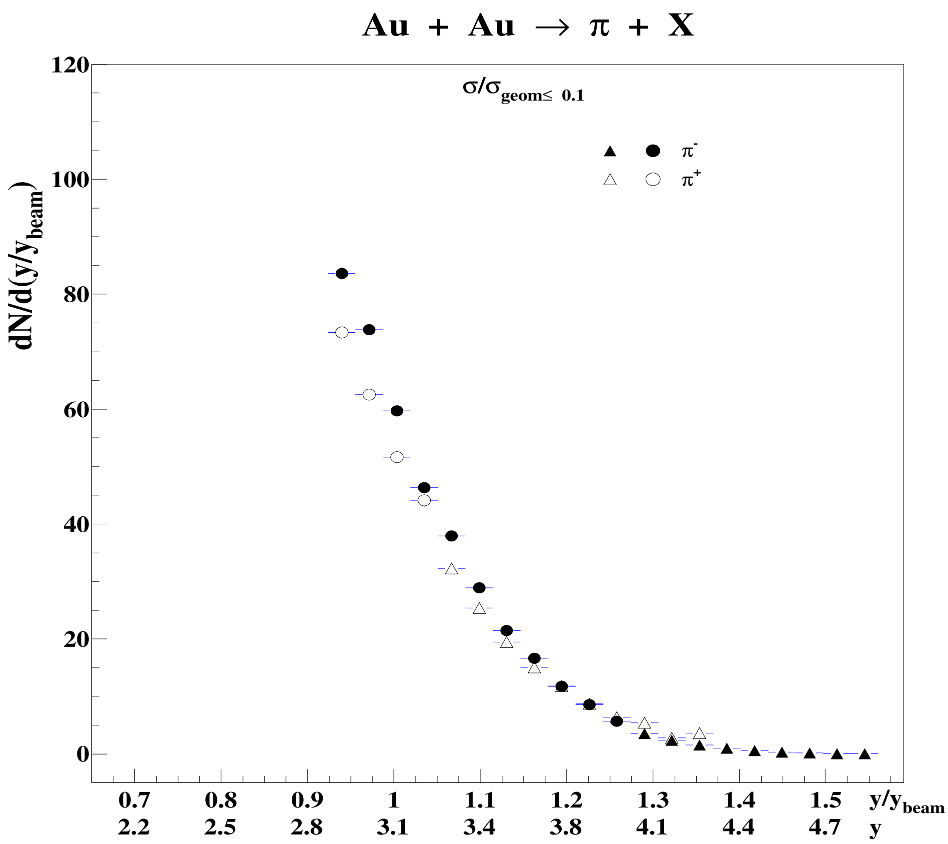

Figure 4.22: Measured charged pion rapidity density in Au + Au collisions at 10.8 GeV/c and 10% inclusive centrality. Circles represent those rapidity bins where a second hot component can be deduced from the data, triangles are those bins where only a single component is measured.

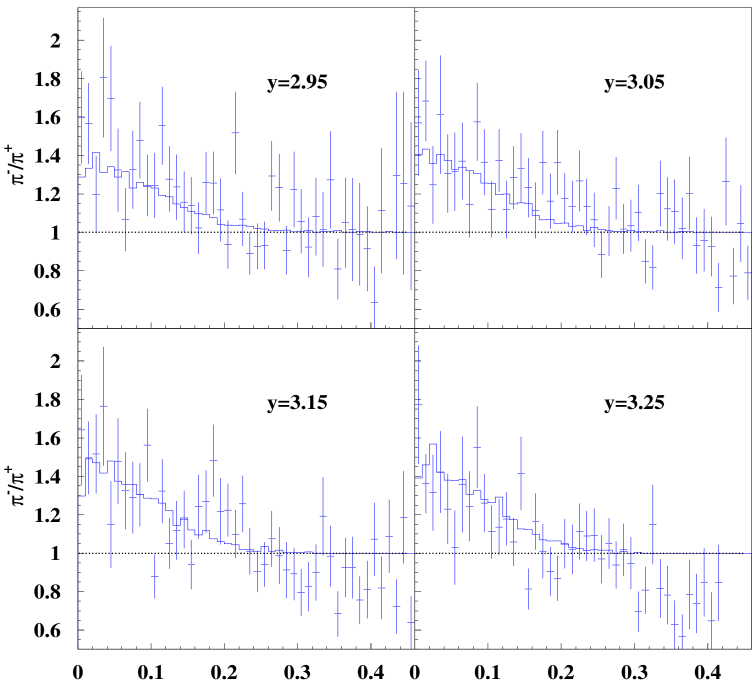

Figure 4.23: Ratios of pion spectra for various rapidity bins. The points are the measurement, the solid histogram is the result of a Monte Carlo decaying lambda using a phase space parameterization consistent with measurement. [45]

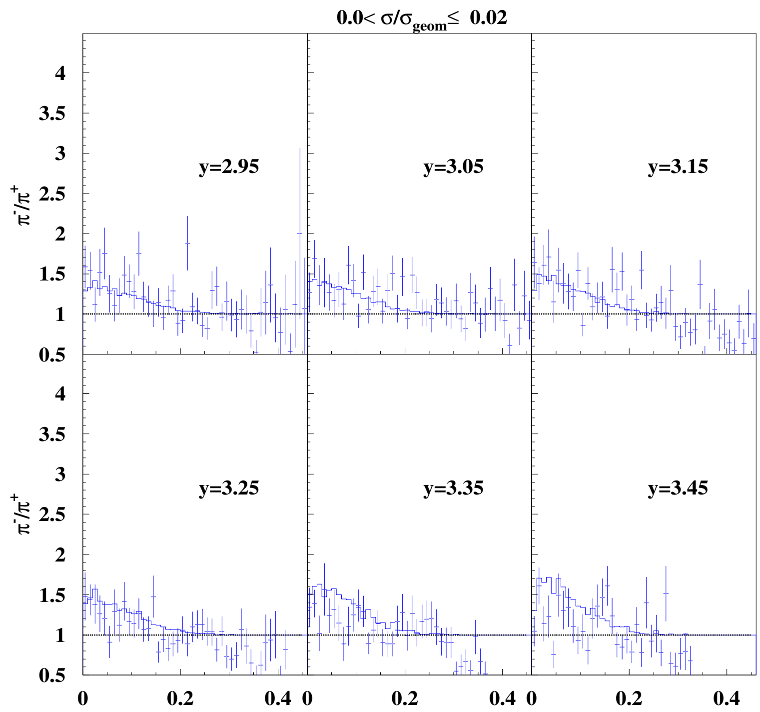

Figure 4.24: Ratios of pion spectra for various rapidity bins and for a centrality of 2% inclusive . The points are the measurement, the solid histogram is the result of a Monte Carlo decaying lambda using a phase space parameterization consistent with measurement. [45]

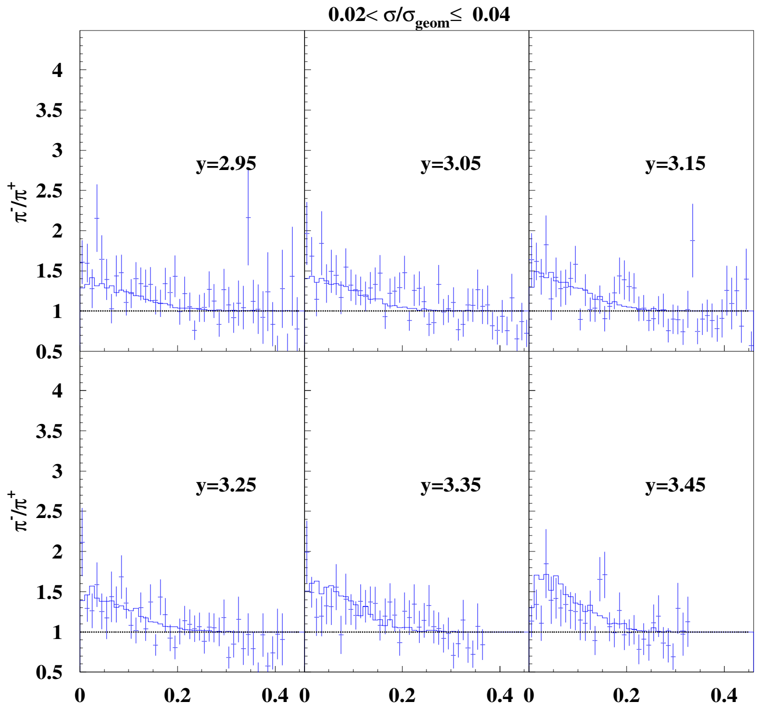

Figure 4.25: Ratios of pion spectra for various rapidity bins and for a centrality of 4-2% exclusive. The points are the measurement, the solid histogram is the result of a Monte Carlo decaying lambda using a phase space parameterization consistent with measurement. [45]

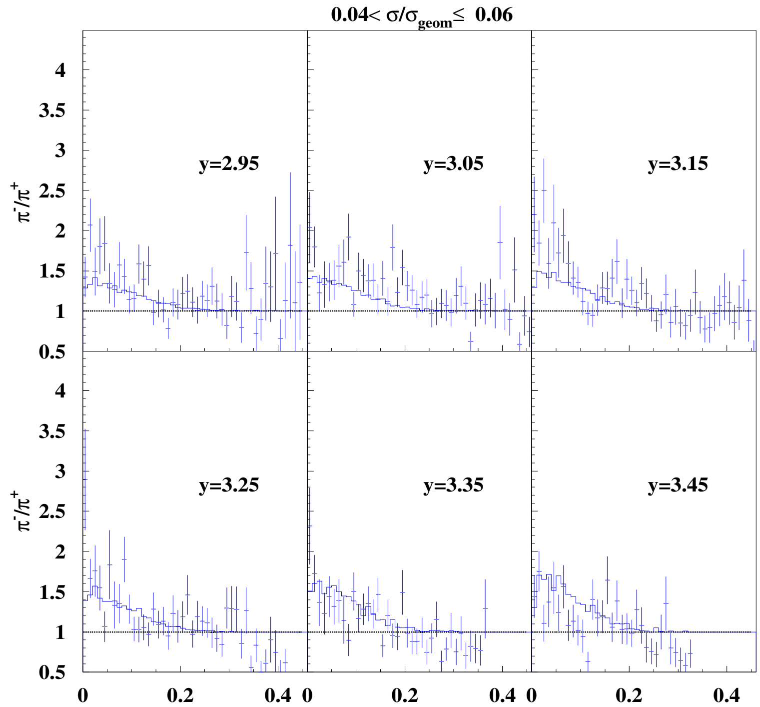

Figure 4.26: Ratios of pion spectra for various rapidity bins and for a centrality of 6-4% exclusive. The points are the measurement, the solid histogram is the result of a Monte Carlo decaying lambda using a phase space parameterization consistent with measurement. [45]

One striking feature of the ratio spectra stands out distinctly at low centrality. A sharp component in the spectra for rapidity bins at or near beam rapidity is clearly seen rising significantly about the background from Lambda. The effect disappears for bins well above or below the beam rapidity and disappears in all bins at sufficiently high centrality. The peak is likely due to coulomb interactions between the produced pions and the spectator region of the projectile. The centrality dependence is caused by the diminishing of the spectator region of the most central collisions. This effect was observed also for lower energy collisions at the BEVALAC by Sullivan et. al. and indeed contributed to Coulomb with the fragmentating spectator region. Models of the interaction depend upon detailed knowledge of the spectator fragmentation function which is not available to us.

Given that a reasonable understanding of the difference between π^- and π^+ is available, we can re-perform an analysis of the spectral shape in terms of resonance feeding. Into our spectrometer model we finally add Δ resonance decay pions. The spectral shape of these decay pions depends critically on the spectrum of the parent. In analysis of Si+Pb collisions, the spectral shape was assumed to follow RQMD and the strength of the effect normalized to best fit data. Here we take a more data driven approach.

The kinematical spectrum of excited baryonic resonances is intimately linked to that of the proton (the residue of the decay). In Si beam collisions, due to the lack of full stopping, numerous protons in the “wings” of the rapidity spectrum were either non or minor participants in the interaction and would not necessarily reflect the distribution of excitations. Our increased ability

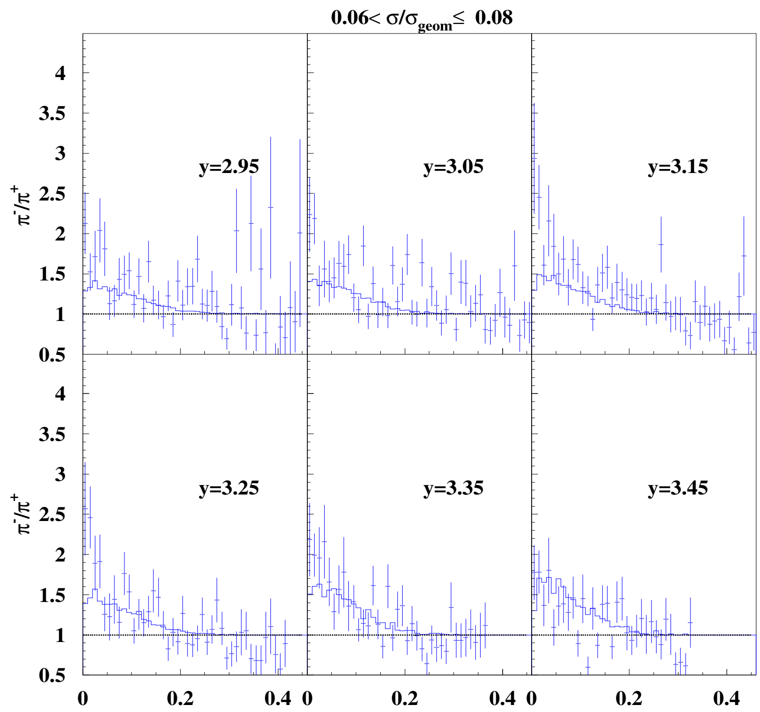

Figure 4.27: Ratios of pion spectra for various rapidity bins and for a centrality of 8-6% exclusive. The points are the measurement, the solid histogram is the result of a Monte Carlo decaying lambda using a phase space parameterization consistent with measurement. [45]

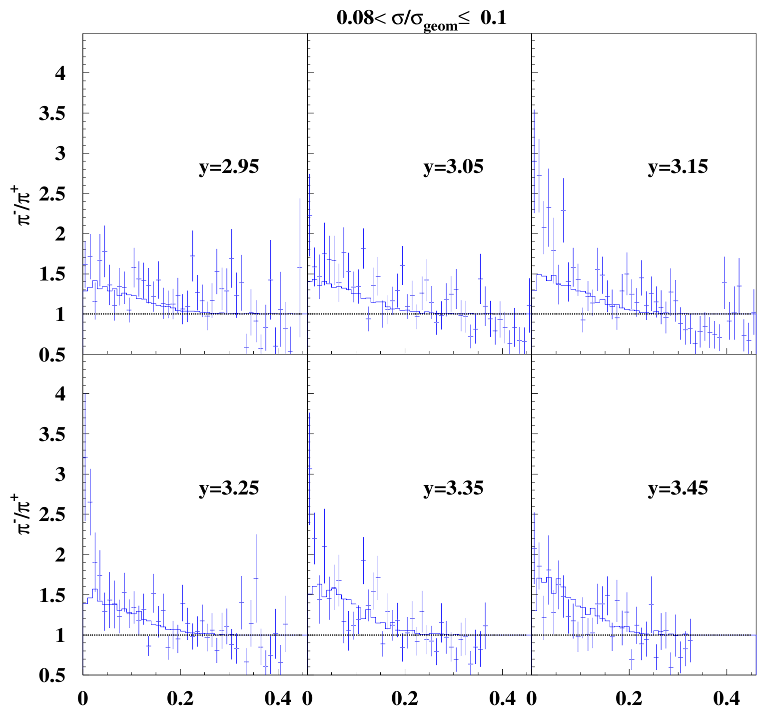

Figure 4.28: Ratios of pion spectra for various rapidity bins and for a centrality of 10-8% exclusive. The points are the measurement, the solid histogram is the result of a Monte Carlo decaying lambda using a phase space parameterization consistent with measurement. [45]

to select high centrality collisions shows the evolution of the proton spectrum with centrality and especially that protons from the most central collisions have a rapidity spectrum similar to Lambdas. We have analyzed the effects of baryonic resonance feeding into pion spectra using both 0.7 (measured proton for most central) and 0.62 (measured Lambda) widths of the rapidity density of Deltas. The difference in the results are within statistics. The data presented below represent the analysis using the proton width, $\sigma_y = 0.7$ units.

Shown in Figure 4.29 is the ratio of the "pion" spectrum to the high-tail Boltzmann fit. The spectrum itself is the result of subtracting from our negative pion data the contribution of the Lambda expected from the E891 measurement. Negative pions must be used since the positive pion measurement does not extend to sufficiently high m_T. The free parameter in the Monte Carlo calculation is the concentration of Δ resonance at freezeout. This free parameter is reflected directly in the π_Δ/π_{dir} ratio. Clearly values of π_Δ/π_{dir} in the range 0.4-0.6 provide a reasonable description of the data. This result is consistent with the Si result. As shown previously, this Δ concentration is consistent to the expectation for a thermally excited source with an excited nucleon to total nucleon ratio of 0.311-0.409 and a Boltzmann temperature of $138^{+30}_{-20} MeV$ (Fig. 4.30).

Let me take a moment to present a caveat to the Δ resonance analysis. Lacking direct confirmation of the Δ concentration, the spectral shape analysis, although it beautifully describes the data, cannot be taken as direct evidence of the Δ concentration. For that reason, we do not state as experimental fact a thermal temperaute of the system. However, we state firmly that any

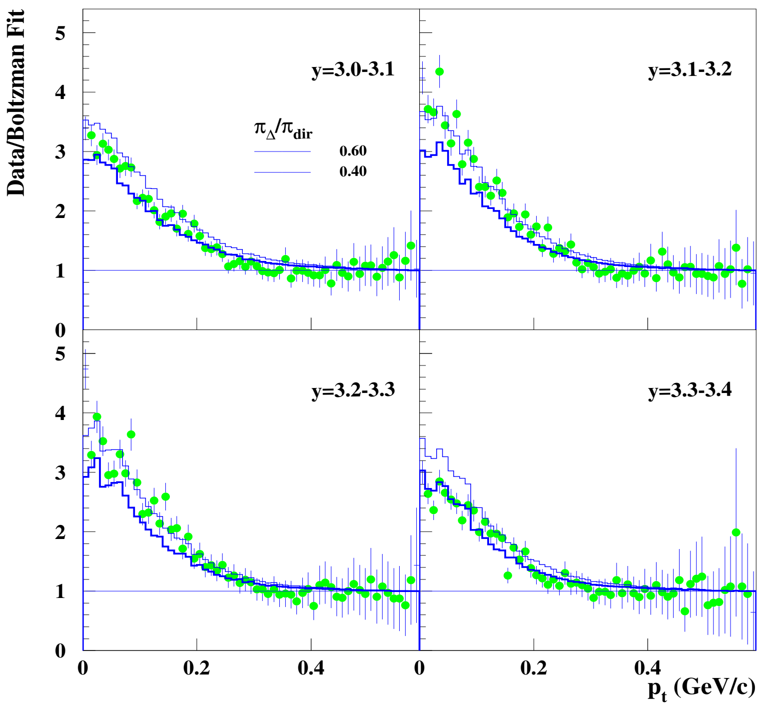

Figure 4.29: Ratios of pion spectra, with respect to a Boltzmann fit to the high p_t part of the π^- spectra, for various rapidity bins. The points are the measurement, the solid histograms are the result of a Monte Carlo as described in the text.

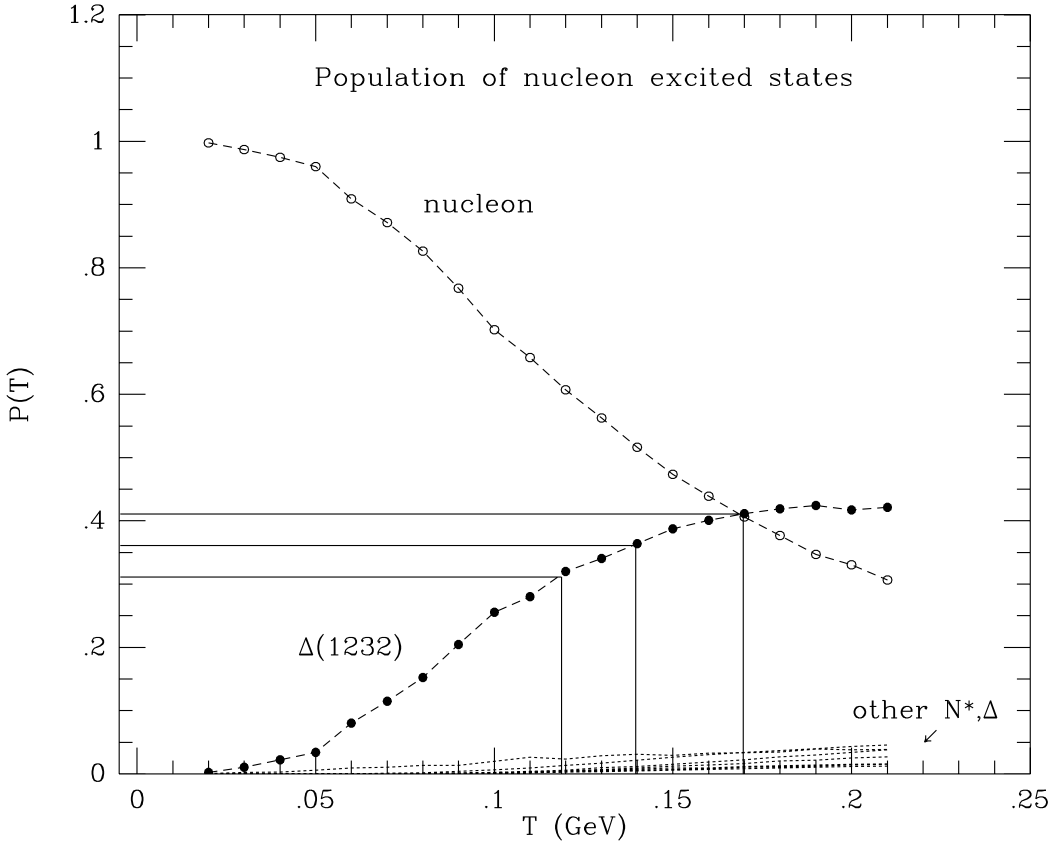

Figure 4.30: Relative population of various resonances as a function of temperature based on the thermal model.

reasonable thermalized model of the system must include baryonic excitation and will inevitably lead to a kinematical spectrum of resonant states which is nearly the same as that of the proton. The temperature parameter of such a model must be near 140 MeV or else it will be in strong disagreement with the experimentally determined pion enhancement.

The pion rapidity spectra for a centrality of 10% inclusive are shown in Figure 4.22. These spectra have been integrated along p_t in a fashion analogous to the protons. In this figure circles represent those rapidity bins where a second hot component can be deduced from the data, triangles are those bins where only a single component is measured. In this figure there appears to be a slightly enhanced yield of π^- to π^+, as would be expected from an isospin asymmetric system such as Au. In Figures 4.31 and 4.32 are presented π^- and pi^+ rapidity densities as a function of centrality. Contrary to the protons, there appears to be no significant centrality dependence to the pion yields over our rapidity coverage.

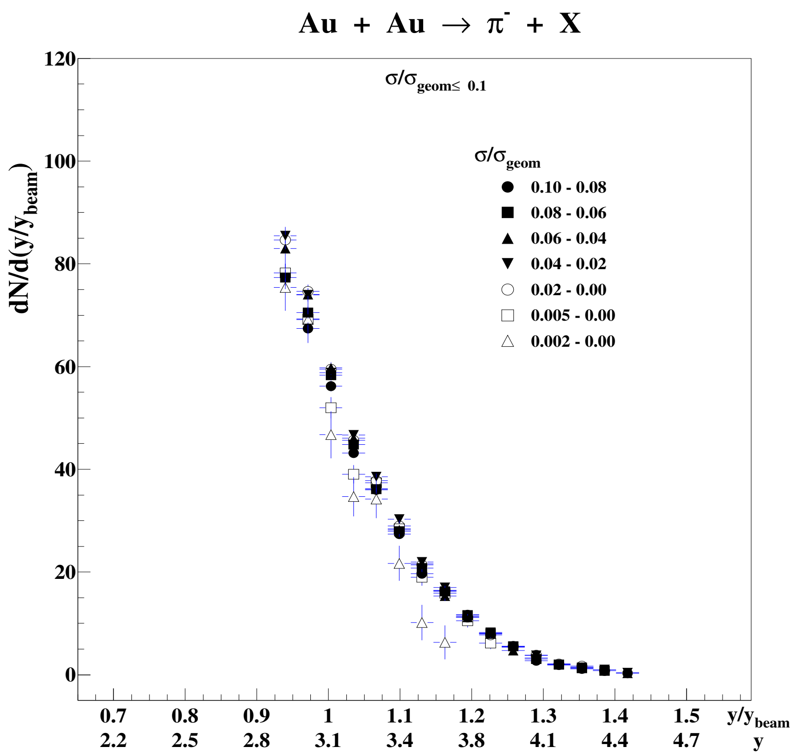

Figure 4.31: Pi minus spectra as a function of centrality.

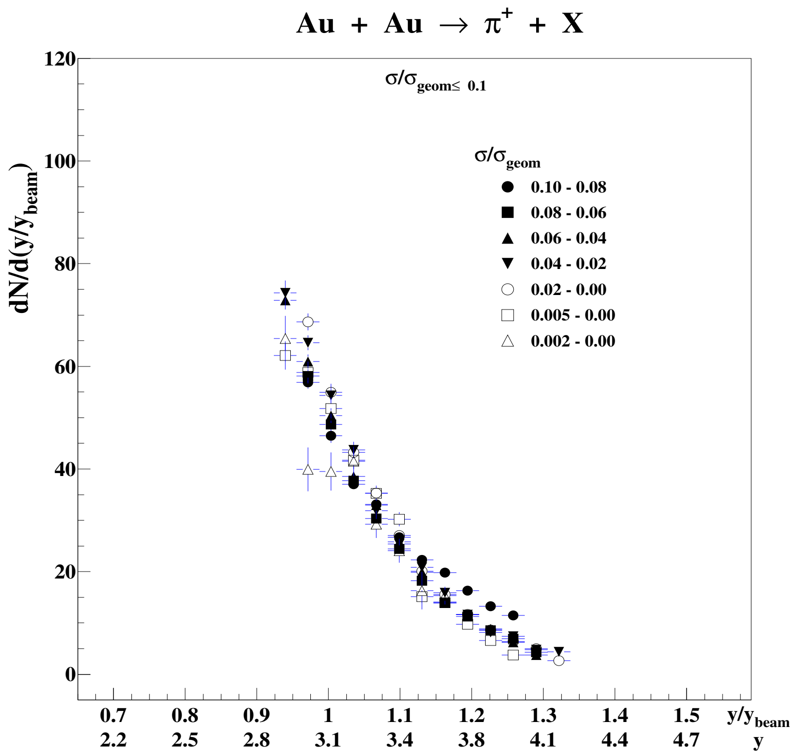

Figure 4.32: Pi plus spectra as a function of centrality.

Chapter 5

Overview

We have seen that proton and pion spectra within our acceptance are well described by Boltzmann parameterizations. A simple isotropic model fails both with regards to the rapidity dependence of the temperature, as well as the p_t=0 intercept. These facts give a strong indication that transverse flow will be important in the Au+Au system.

No significant nuclear transparency is observed, and a strong centrality dependence of dN/dy is observed. In the most central collisions the width of the proton dN/dy begins to approach that of the measured Lambda width [51]. This indicates that a large degree of stopping, and thus a large baryon density is reached in these collisions. RQMD, which predicts a peak baryon density 7 times that of normal nuclear matter, reproduces the rapidity distributions of protons rather well.

As was observed in Si+Pb and Si+Al, the pion spectra show a clear two component nature, with the low p_t component being significantly colder than that at high p_t. The two pion charge states show a pronounced anisotropy in the transverse momentum spectra at low p_t. This effect can quantitatively be described, within statistics, by hyperon decay. An intriguing centrality dependence was observed in the charged pion spectral ratios. This dependence was confined to rapidities around beam rapidity, and may indicate Coulomb interaction with the nuclear spectators at high centrality. Studies of the rapidity dependence this effect, with higher statistics (i.e. 1994 run) and finer rapidity binning, could yield information on the absolute time scale of pion emission. Pion dN/dy show little, if any, evolution over centrality bins. Quantitative analysis of the π^- spectral shapes, in the context of the Delta feeding model, results in a $\pi_\Delta/\pi_{direct} = 0.5 \pm 0.1$. This implies a fractional delta population of 0.36 and a freezout temperature of $138^{+30}_{-20} MeV$ in good agreement with those results from Si+Pb of $130 \pm 10 MeV$. In this case a direct reconstruction of the Delta resonance, with improved statistics, would of course cinch the Delta analysis.

Bibliography

[1] A. Das and T. Ferbel, Introduction To Nuclear and Particle Physics, John Wiley & Sons, New York,(1994)1.

[2] G. Baym, *et al., Quark Matter '88, Nucl. Phys.* **A498,(1989)1c-628c.**

[3] J.P. Blaizot, *et al., Quark Matter '90, Nucl. Phys.* **A525,(1991)1c-723c.**

[4] L. Van Hove, Indian J. Phys. **(63A)(7),(1989)757.**

[5] M. Jacob, *et al., Phys. Reports* **88***(19982)321.*

[6] B. Müller, Nucl-th preprint **NUCL-TH-9410005.**

[7] L McLerran, Rev. Mod. Phys. **58**, No. 4,(1986)1021.

[8] V. M. Emel'yanov, *et al., Fortschr. Phys.* **38**, *1(1990)1.*

[9] T.C. Awes, *et al., Quark Matter '91, Nucl. Phys.* **A544,(1992)1c-669c.**

[10] H. Sorge, *et al.*, Ann. Phys. (NY) **A192**,(1989)266.

[11] D. Beavis, *et al.*, Nucl. Phys. **A590**,(1995)491c.

[12] J. Barrette, *et al.*, Phys. Rev. Lett. **70, (1993)1763.**

[13] M.S. Muthuswamy, Ph.D. thesis, SUNY at Stony Brook, 1992.

[14] J. Dee, Ph.D. thesis, SUNY at Stony Brook, 1995.

[15] L.S. Waters, Ph.D. thesis, SUNY at Stony Brook, 1990.

[16] J. Barrette, *et al., Phys. Rev.* **C46, (1992)312.**

[17] J. Barrette, *et al., Phys. Rev.* **C51, (1995)3309.**

[18] J.D. Jackson, Classical Electrodynamics, John Wiley & Sons, Inc. New York, 1975.

[19] J. Simon-Gillo, Ph.D thesis, Texas A&M Univ. (1992).

[20] Z. Zhang, Ph.D thesis, Univ. of Pittsburg (1993).

[21] Y. Zhang, Ph.D. thesis, SUNY at Stony Brook (1995).

[22] A.G. Ruggiero, AIP Conf. Proc. 249, Vol. 2 (1989).

[23] P. Thieberger, *et al.,Nucl. Instrum. Methods* **A268, (1988) 513-521.**

[24] P. Braun-Munzinger, *et al., E877 Note #1. (1994).*

[25] P. Braun-Munzinger, *et al., E877 Note#3. (1994).*

[26] B. Hong, Ph.D thesis, SUNY at Stony Brook (1995).

[27] R. Debbe, *et al., IEEE Trans. Nucl. Sci.* **37, (1990)88.**

[28] J Fischer, *et al., IEEE Trans. Nucl. Sci.* **37, (1990)82.**

[29] S.V. Green, Ph.D thesis, Yale University (1992).

[30] W.C. Llope, Ph.D thesis, SUNY at Stony Brook(1991).

[31] http://www.csulb.edu/vc/libarts/am-indian/

[32] D.G. Cassel and H. Kowalski, Nucl. Instrum. Methods **185, (1981).**

[33] K. Shigaki, Ph.D thesis, University of Tokyo(1995).

[34] J. Barrette, *et al., Phys. Rev.* **C45, (1992)819.**

[35] J. Barrette, *et al., Phys. Rev.* **C50, (1992)3047.**

[36] R. Bersch, M.S Thesis, SUNY at Stony Brook (1995).

[37] Particle Data Group, Phys. Rev. **D45, (1992).**

[38] J. Barrette, *et al., Phys. Rev. Lett.* **64, (1990)1219.**

[39] G.E. Brown, *et al., Phys. Lett.* **B253, (1991)19.**

[40] J. Barrette, *et al., Phys. Lett.* **B351, (1995)93.**

[41] D. Miskowiec, E877 Note.#8 (1996).

[42] J. Gillo, Nucl. Phy. **A566, (1994)175c.**

[43] R. Lacasse, Ph.D. Dissertation, McGill University, in preparation.

[44] R. Brun *et al.*, Geant 3 Users Guide, CERN Data Handling Division Report No. DD/EE/84-1, 1984(unpublished)

[45] S. Ahmad, *et al., Phys. Lett.* **B382, (1996)35.**

[46] I. Bearden, *et al., Submitted Phys. Rev. Lett., Nov 1996, Cern preprint* **CERN-PPE/96-163.**

[47] T. Csörgő, *et al., Phys Rev.* **C54, 1390(1996).**

[48] E. Schnedermann, *et al., Phys. Rev.* **C48, 625(1990).**

[49] P. Braun-Munzinger, *et al., Phys. Lett.* **B344, 43(1995).**

[50] T. Abbott, *et al., Phys. Rev.* **C50, 1024(1994).**

[51] S. Ahmad, *et al., Phys. Lett.* **B382, 35(1996).**

[52] Z. Chen, Proc. HIPAGS'96, Wayne State Univ., WSU-NP-96-16,5(1996).

[53] R. Mattiello, *et al., Submitted Phys. Rev.* **C, NUCL-TH/9607003.**

[54] H. Sorge, *et al., Phys. Rev.* **C49**, *1253(1994).*

Appendix A

Thermal Model

The predictions of a purely thermal model for the number of particles d^3N, of a givem mass m, produced into an element of phase space d^3p satisfies

$$\frac{d^3N}{d^3p} \propto exp\left(-\frac{E-\mu}{T}\right), \tag{A.1}$$

where T is the temperature of the source, E is the center-of-momentum energy associated with d^3p, and μ is the chemical potential. Expressed in terms of the invariant multiplicity this becomes

$$\frac{1}{m_t}\frac{d^2N}{dm_t dy} = A_B(y)\frac{m_t}{m}exp\left(-\frac{(m_t-m)}{T_B(y)}\right), \tag{A.2}$$

with $A_B \propto mcosh(y-y_{cm})exp(\mu/T - m/T_B)$ being the $m_t - m = 0$ intercept of the function in the rapidity bin centered about y. $T_B(y) = T/cosh(y-y_{cm})$ and y_{cm} is the rapidity of the center-of-momentum frame. These functional forms of A_B and T_B hold only for an isotropically emitting source, in the presence of momentum-space correlations (flow) the shapes of these variable may vary.

To determine the rapidity density from an isotropic thermal fireball one must integrate

$$\frac{d^2N}{dm_t dy} = A' m_t^2 cosh(y) exp\left(-\frac{m_t cosh(y)}{T}\right). \tag{A.3}$$

Performing the integral over m_t, we find

$$\frac{dN}{dy} = Ce^{-\alpha}\left(1 + \frac{2}{\alpha} + \frac{2}{\alpha^2}\right) \tag{A.4}$$

where

$$\alpha = \frac{m}{T} coshy. \tag{A.5}$$

Appendix B

Tabulated results

y	$T_B(GeV)$	$A_B\left(\frac{c^4}{GeV^2}\right)$	$\frac{dn}{dy}$
2.15	0.3403 ± 0.0576	154.84 ± 3.57	98.48 ± 1.76
2.25	0.3517 ± 0.0439	155.99 ± 3.17	104.46 ± 1.38
2.35	0.2570 ± 0.0147	164.67 ± 2.84	67.63 ± 0.48
2.45	0.2220 ± 0.0078	170.98 ± 2.63	56.57 ± 0.34
2.55	0.1834 ± 0.0037	177.14 ± 2.34	44.88 ± 0.30
2.65	0.1660 ± 0.0022	177.30 ± 2.15	39.54 ± 0.28
2.75	0.1464 ± 0.0013	181.79 ± 2.01	34.27 ± 0.26
2.85	0.1335 ± 0.0012	175.02 ± 2.30	29.59 ± 0.22
2.95	0.1219 ± 0.0012	165.24 ± 2.85	25.40 ± 0.18
3.05	0.1118 ± 0.0013	148.71 ± 2.90	21.40 ± 0.16
3.15	0.0970 ± 0.0014	131.84 ± 3.15	16.57 ± 0.12
3.25	0.0980 ± 0.0034	87.22 ± 4.07	11.48 ± 0.09
3.35	0.0874 ± 0.0060	64.70 ± 3.82	6.78 ± 0.08
3.45	0.0513 ± 0.0063	58.06 ± 3.55	3.02 ± 0.07

Table B.1: Tabulated results for protons at 10% centrality using a Boltzmann parameterization, i.e. $\frac{1}{m_t^2} \cdot \frac{d^2N}{dm_t dy} = \frac{A_B(y)}{m_p} \cdot e^{\frac{m_t - m_p}{T_B(y)}}$. All errors are statistical.

y	$T_B(GeV)$	$A_B\left(\frac{c^4}{GeV^2}\right)$	$\frac{dn}{dy}$
2.95	0.0579 ± 0.0010	1390.0 ± 41.7	26.63 ± 0.36
3.05	0.0585 ± 0.0009	1155.8 ± 34.2	23.52 ± 0.27
3.15	0.0554 ± 0.0009	1051.7 ± 31.4	19.02 ± 0.23
3.25	0.0547 ± 0.0008	839.56 ± 24.20	14.76 ± 0.18
3.35	0.0518 ± 0.0008	751.35 ± 22.56	12.09 ± 0.16
3.45	0.0507 ± 0.0007	604.37 ± 17.55	9.21 ± 0.12
3.55	0.0478 ± 0.0008	494.37 ± 14.82	6.84 ± 0.10
3.65	0.0469 ± 0.0007	382.93 ± 11.67	5.31 ± 0.08
3.75	0.0433 ± 0.0007	317.25 ± 10.32	3.74 ± 0.07
3.85	0.0405 ± 0.0007	255.75 ± 8.67	2.74 ± 0.07
3.95	0.0397 ± 0.0007	176.50 ± 6.10	1.80 ± 0.05
4.05	0.0353 ± 0.0008	141.19 ± 5.67	1.14 ± 0.03
4.15	0.0336 ± 0.0008	100.93 ± 4.17	0.75 ± 0.02
4.25	0.0323 ± 0.0008	66.07 ± 3.03	0.50 ± 0.02
4.35	0.0296 ± 0.0010	49.48 ± 2.77	0.32 ± 0.01
4.45	0.0313 ± 0.0021	27.36 ± 2.14	0.20 ± 0.01
4.55	0.0270 ± 0.0026	18.70 ± 2.03	0.11 ± 0.01
4.65	0.0260 ± 0.0027	11.34 ± 1.52	0.06 ± 0.01
4.75	0.0182 ± 0.0046	8.36 ± 2.46	0.02 ± 0.01
4.85	0.0172 ± 0.0050	8.00 ± 2.95	0.02 ± 0.01

Table B.2: Tabulated results for pi plus at 10% centrality using a Boltzmann parameterization over the first 300MeV/c in p_t. All errors are statistical.

y	$T_B(GeV)$	$A_B\left(\frac{c^4}{GeV^2}\right)$
2.95	0.0800 ± 0.0087	581.29 ± 209.08
3.05	0.0867 ± 0.0025	407.52 ± 40.99
3.15	0.0858 ± 0.0025	307.69 ± 31.94
3.25	0.0825 ± 0.0026	250.88 ± 29.34
3.35	0.0722 ± 0.0028	296.34 ± 45.01
3.45	0.0739 ± 0.0043	190.51 ± 43.86
3.55	0.0711 ± 0.0060	151.90 ± 51.19
3.65	0.0716 ± 0.0067	99.82 ± 36.79
3.75	0.0730 ± 0.0016	52.64 ± 40.45
3.85	0.0849 ± 0.0326	23.36 ± 27.37
3.95	0.0821 ± 0.0358	14.97 ± 18.71

Table B.3: Tabulated results for pi plus at 10% centrality using a Boltzmann parameterization over $300MeV/c \leq p_t \leq 600MeV/c$.

y	$T_B(GeV)$	$A_B\left(\frac{c^4}{GeV^2}\right)$	$\frac{dn}{dy}$
2.95	0.0646 ± 0.0012	957.53 ± 28.49	23.36 ± 0.37
3.05	0.0658 ± 0.0011	786.82 ± 22.89	19.92 ± 0.28
3.15	0.0646 ± 0.0011	669.52 ± 19.47	16.45 ± 0.37
3.25	0.0622 ± 0.0010	599.47 ± 16.76	14.06 ± 0.36
3.35	0.0608 ± 0.0010	511.84 ± 15.07	10.28 ± 0.15
3.45	0.0582 ± 0.0009	443.05 ± 12.87	8.09 ± 0.13
3.55	0.0531 ± 0.0011	396.87 ± 11.98	6.20 ± 0.11
3.65	0.0519 ± 0.0011	319.00 ± 10.55	4.80 ± 0.08
3.75	0.0501 ± 0.0012	271.54 ± 9.40	3.76 ± 0.07
3.85	0.0457 ± 0.0014	227.18 ± 8.39	2.79 ± 0.06
3.95	0.0444 ± 0.0017	176.39 ± 6.52	2.04 ± 0.04
4.05	0.0487 ± 0.0037	130.71 ± 5.65	1.73 ± 0.05
4.15	0.0326 ± 0.0326	124.30 ± 6.35	0.90 ± 0.25
4.25	0.0505 ± 0.0132	83.55 ± 5.66	1.17 ± 0.08
4.35	—	62.46 ± 2.91	$- - \pm$

Table B.4: Tabulated results for pi plus at 10% centrality using a Boltzmann parameterization over the first 300MeV/c in p_t. All errors are statistical.

y	$T_B(GeV)$	$A_B\left(\frac{c^4}{GeV^2}\right)$
2.95	0.0911 ± 0.0066	389.32 ± 83.63
3.05	0.0977 ± 0.0062	294.75 ± 53.68
3.15	0.0925 ± 0.0162	277.39 ± 140.76
3.25	0.1001 ± 0.0178	178.82 ± 75.83

Table B.5: Tabulated results for pi plus at 10% centrality using a Boltzmann parameterization over $300MeV/c \leq p_t \leq 600MeV/c$.

y	$T_B(GeV)$	$A_B\left(\frac{c^4}{GeV^2}\right)$	$\frac{dn}{dy}$
2.15	0.3145 ± 0.0634	172.37 ± 4.94	$---$
2.25	0.2802 ± 0.0350	172.30 ± 4.36	$---$
2.35	0.2612 ± 0.0205	173.46 ± 3.81	67.72 ± 0.55
2.45	0.2112 ± 0.0087	185.96 ± 3.51	56.39 ± 0.41
2.55	0.1797 ± 0.0046	185.06 ± 3.16	44.69 ± 0.37
2.65	0.1647 ± 0.0029	178.04 ± 2.78	38.67 ± 0.35
2.75	0.1451 ± 0.0018	177.48 ± 3.00	33.26 ± 0.31
2.85	0.1312 ± 0.0015	162.20 ± 3.34	26.98 ± 0.26
2.95	0.1208 ± 0.0016	144.89 ± 3.38	21.90 ± 0.22
3.05	0.1057 ± 0.0018	128.75 ± 3.69	17.44 ± 0.19
3.15	0.0969 ± 0.0024	103.35 ± 3.89	12.95 ± 0.17
3.25	0.0865 ± 0.0034	75.76 ± 3.84	8.22 ± 0.12
3.35	0.0734 ± 0.0130	52.41 ± 8.51	4.31 ± 0.11
3.45	0.0522 ± 0.0128	42.08 ± 4.92	2.09 ± 0.09

Table B.6: Tabulated results for protons at 4% centrality using a Boltzmann parameterization, i.e. $\frac{1}{m_t^2} \cdot \frac{d^2N}{dm_t dy} = \frac{A_B(y)}{m_p} \cdot e^{\frac{m_t - m_p}{T_B(y)}}$. All errors are statistical.

y	$T_B(GeV)$	$A_B\left(\frac{c^4}{GeV^2}\right)$	$\frac{dn}{dy}$
2.95	0.0567 ± 0.0018	1480.4 ± 46.4	27.41 ± 0.44
3.05	0.0565 ± 0.0018	1256.1 ± 40.0	24.05 ± 0.33
3.15	0.0523 ± 0.0016	1110.6 ± 34.2	19.13 ± 0.28
3.25	0.0502 ± 0.0014	933.70 ± 27.50	14.88 ± 0.23
3.35	0.0482 ± 0.0014	838.11 ± 24.42	12.32 ± 0.20
3.45	0.0504 ± 0.0014	642.87 ± 18.96	9.47 ± 0.16
3.55	0.0453 ± 0.0014	518.32 ± 16.29	6.98 ± 0.15
3.65	0.0448 ± 0.0012	423.39 ± 13.23	5.40 ± 0.12
3.75	0.0396 ± 0.0010	361.43 ± 11.30	3.64 ± 0.09
3.85	0.0383 ± 0.0011	279.50 ± 9.11	2.56 ± 0.08
3.95	0.0356 ± 0.0012	197.90 ± 6.93	1.73 ± 0.06
4.05	0.0322 ± 0.0009	169.85 ± 5.98	1.26 ± 0.05
4.15	0.0274 ± 0.0012	118.52 ± 4.86	0.73 ± 0.04
4.25	0.0327 ± 0.0014	70.82 ± 3.47	0.51 ± 0.03
4.35	0.0232 ± 0.0012	63.84 ± 3.18	0.32 ± 0.02
4.45	0.0201 ± 0.0023	38.45 ± 2.88	0.18 ± 0.02
4.55	0.0291 ± 0.0044	18.80 ± 2.05	0.10 ± 0.01
4.65	0.0271 ± 0.0065	11.56 ± 2.42	0.05 ± 0.01
4.75	—	7.32 ± 2.50	$- - \pm$

Table B.7: Tabulated results for pi plus at 4% centrality using a Boltzmann parameterization over the first 300MeV/c in p_t. All errors are statistical.

y	$T_B(GeV)$	$A_B\left(\frac{c^4}{GeV^2}\right)$
2.95	0.0731 ± 0.0027	862.56 ± 90.29
3.05	0.0791 ± 0.0016	604.76 ± 37.01
3.15	0.0761 ± 0.0016	506.11 ± 33.11
3.25	0.0704 ± 0.0017	462.24 ± 35.13
3.35	0.0636 ± 0.0016	489.91 ± 41.35
3.45	0.0634 ± 0.0019	340.91 ± 33.66
3.55	0.0618 ± 0.0032	265.99 ± 44.61
3.65	0.0614 ± 0.0034	194.82 ± 32.68
3.75	0.0514 ± 0.0031	197.87 ± 38.22
3.85	0.0566 ± 0.0191	94.57 ± 86.16

Table B.8: Tabulated results for pi plus at 4% centrality using a Boltzmann parameterization over $300MeV/c \leq p_t \leq 600MeV/c$.

y	$T_B(GeV)$	$A_B\left(\frac{c^4}{GeV^2}\right)$	$\frac{dn}{dy}$
2.95	0.0685 ± 0.0034	1001.5 ± 40.7	25.23 ± 0.58
3.05	0.0625 ± 0.0026	882.50 ± 35.28	21.39 ± 0.37
3.15	0.0585 ± 0.0022	784.60 ± 29.76	17.42 ± 0.39
3.25	0.0627 ± 0.0026	666.06 ± 26.01	14.51 ± 0.41
3.35	0.0545 ± 0.0021	618.08 ± 24.29	10.74 ± 0.19
3.45	0.0574 ± 0.0023	482.21 ± 19.63	8.36 ± 0.17
3.55	0.0510 ± 0.0016	436.39 ± 16.85	6.42 ± 0.15
3.65	0.0507 ± 0.0015	355.71 ± 14.40	4.96 ± 0.10
3.75	0.0489 ± 0.0017	283.51 ± 12.78	3.75 ± 0.09
3.85	0.0433 ± 0.0025	241.52 ± 12.06	2.60 ± 0.08
3.95	0.0450 ± 0.0043	194.85 ± 10.65	2.28 ± 0.06
4.05	0.0383 ± 0.0060	152.04 ± 10.19	1.39 ± 0.06
4.15	0.0289 ± 0.0049	140.82 ± 11.12	0.85 ± 0.05
4.25	—	95.08 ± 14.06	$- - \pm$
4.35	—	59.56 ± 7.68	$- - \pm$

Table B.9: Tabulated results for pi plus at 4% centrality using a Boltzmann parameterization over the first 300MeV/c in p_t. All errors are statistical.

y	$T_B(GeV)$	$A_B\left(\frac{c^4}{GeV^2}\right)$
2.95	0.0790 ± 0.0033	664.66 ± 69.42
3.05	0.0856 ± 0.0023	483.30 ± 34.60
3.15	0.0784 ± 0.0023	482.61 ± 37.99
3.25	0.0748 ± 0.0031	421.36 ± 43.67
3.35	0.0821 ± 0.0048	277.90 ± 35.29

Table B.10: Tabulated results for pi plus at 4% centrality using a Boltzmann parameterization over $300MeV/c \leq p_t \leq 600MeV/c$.

y	$T_B(GeV)$	$A_B\left(\frac{c^4}{GeV^2}\right)$	$\frac{dn}{dy}$
2.25	0.4127 ± 0.0828	134.74 ± 4.17	117.43 ± 2.45
2.35	0.2623 ± 0.0226	146.87 ± 3.89	62.31 ± 0.67
2.45	0.2311 ± 0.0127	148.23 ± 3.51	51.66 ± 0.49
2.55	0.1843 ± 0.0060	164.81 ± 3.67	41.63 ± 0.44
2.65	0.1627 ± 0.0035	177.84 ± 3.53	38.60 ± 0.42
2.75	0.1454 ± 0.0021	181.67 ± 3.22	33.97 ± 0.40
2.85	0.1343 ± 0.0016	184.94 ± 3.08	31.53 ± 0.36
2.95	0.1188 ± 0.0020	185.71 ± 5.29	27.57 ± 0.32
3.05	0.1103 ± 0.0022	177.66 ± 5.64	24.66 ± 0.31
3.15	0.0981 ± 0.0027	157.01 ± 6.57	19.19 ± 0.27
3.25	0.0962 ± 0.0043	118.21 ± 6.27	13.90 ± 0.21
3.35	0.1019 ± 0.0123	74.54 ± 6.81	8.74 ± 0.18
3.45	0.0511 ± 0.0121	71.69 ± 8.29	3.72 ± 0.17

Table B.11: Tabulated results for protons at an exclusive centrality of 10%−8% using a Boltzmann parameterization, i.e. $\frac{1}{m_t^2} \cdot \frac{d^2N}{dm_t dy} = \frac{A_B(y)}{m_p} \cdot e^{\frac{m_t - m_p}{T_B(y)}}$. All errors are statistical.

y	$T_B(GeV)$	$A_B\left(\frac{c^4}{GeV^2}\right)$	$\frac{dn}{dy}$
2.95	0.0581 ± 0.0012	1305.1 ± 41.8	
3.05	0.0579 ± 0.0012	1124.9 ± 36.4	21.47 ± 0.38
3.15	0.0528 ± 0.0011	1068.6 ± 34.0	17.90 ± 0.33
3.25	0.0515 ± 0.0010	860.66 ± 26.54	13.76 ± 0.27
3.35	0.0493 ± 0.0010	784.89 ± 25.06	11.47 ± 0.25
3.45	0.0492 ± 0.0010	588.38 ± 19.64	8.72 ± 0.20
3.55	0.0473 ± 0.0013	460.73 ± 16.79	6.27 ± 0.18
3.65	0.0473 ± 0.0010	381.30 ± 13.60	5.23 ± 0.16
3.75	0.0415 ± 0.0010	339.31 ± 12.98	3.72 ± 0.13
3.85	0.0371 ± 0.0010	282.38 ± 11.49	2.55 ± 0.11
3.95	0.0403 ± 0.0014	177.94 ± 7.97	1.74 ± 0.09
4.05	0.0325 ± 0.0017	134.97 ± 7.76	0.86 ± 0.07
4.15	0.0267 ± 0.0034	113.53 ± 7.63	0.60 ± 0.05
4.25	0.0223 ± 0.0028	74.37 ± 5.72	0.37 ± 0.04
4.35	0.0267 ± 0.0058	37.38 ± 4.24	0.26 ± 0.03
4.45	0.0298 ± 0.0088	27.03 ± 3.54	0.10 ± 0.03

Table B.12: Tabulated results for pi plus at an exclusive centrality of $10\% - 8\%$ using a Boltzmann parameterization over the first 300MeV/c in p_t. All errors are statistical.

y	$T_B(GeV)$	$A_B\left(\frac{c^4}{GeV^2}\right)$
3.05	0.0831 ± 0.0054	388.49 ± 89.90
3.15	0.0879 ± 0.0063	246.21 ± 60.20
3.25	0.0771 ± 0.0060	293.90 ± 84.66
3.35	0.0776 ± 0.0019	207.74 ± 170.94
3.45	0.0687 ± 0.0018	242.85 ± 241.37

Table B.13: Tabulated results for pi plus at an exclusive centrality of $10\% - 8\%$ using a Boltzmann parameterization over $300MeV/c \leq p_t \leq 600MeV/c$.

y	$T_B(GeV)$	$A_B\left(\frac{c^4}{GeV^2}\right)$	$\frac{dn}{dy}$
2.95	0.0607 ± 0.0015	949.61 ± 37.87	
3.05	0.0660 ± 0.0017	727.80 ± 28.82	$18.12\pm$
3.15	0.0640 ± 0.0016	608.81 ± 24.22	$14.80\pm$
3.25	0.0631 ± 0.0016	519.04 ± 21.02	$11.80\pm$
3.35	0.0628 ± 0.0017	443.33 ± 19.33	$10.53\pm$
3.45	0.0586 ± 0.0016	392.00 ± 17.41	$8.50\pm$
3.55	0.0548 ± 0.0020	345.07 ± 16.47	$7.09\pm$
3.65	0.0574 ± 0.0026	270.01 ± 14.72	$6.32\pm$
3.75	0.0517 ± 0.0027	247.16 ± 14.21	$5.19\pm$
3.85	0.0486 ± 0.0039	212.61 ± 13.68	$4.22\pm$
3.95	0.0486 ± 0.0076	131.31 ± 10.47	$3.65\pm$
4.05	—-	98.55 ± 10.08	
4.15	—-	113.67 ± 10.92	

Table B.14: Tabulated results for pi plus at an exclusive centrality of $10\% - 8\%$ using a Boltzmann parameterization over the first 300MeV/c in p_t. All errors are statistical.

y	$T_B(GeV)$	$A_B\left(\frac{c^4}{GeV^2}\right)$
3.05	0.0913 ± 0.0108	314.12 ± 112.70
3.15	0.0859 ± 0.0189	315.29 ± 210.54

Table B.15: Tabulated results for pi plus at an exclusive centrality of $10\% - 8\%$ using a Boltzmann parameterization over $300 MeV/c \leq p_t \leq 600 MeV/c$.

y	$T_B(GeV)$	$A_B\left(\frac{c^4}{GeV^2}\right)$	$\frac{dn}{dy}$
2.25	0.5081 ± 0.1127	139.77 ± 3.87	
2.35	0.2693 ± 0.0224	154.07 ± 3.80	67.98 ± 0.70
2.45	0.2340 ± 0.0125	157.70 ± 3.56	56.08 ± 0.51
2.55	0.1860 ± 0.0056	168.71 ± 3.35	43.34 ± 0.45
2.65	0.1689 ± 0.0037	176.38 ± 3.56	39.91 ± 0.43
2.75	0.1458 ± 0.0021	185.74 ± 3.36	34.88 ± 0.40
2.85	0.1303 ± 0.0016	188.20 ± 3.20	30.96 ± 0.36
2.95	0.1225 ± 0.0021	173.82 ± 4.96	27.04 ± 0.33
3.05	0.1110 ± 0.0022	168.97 ± 5.49	23.60 ± 0.30
3.15	0.0997 ± 0.0028	142.89 ± 6.06	18.05 ± 0.25
3.25	0.0875 ± 0.0041	116.42 ± 6.83	12.17 ± 0.19
3.35	0.0885 ± 0.0107	75.22 ± 7.82	7.54 ± 0.17
3.45	0.0487 ± 0.0116	68.26 ± 8.19	3.38 ± 0.14

Table B.16: Tabulated results for protons at an exclusive centrality of $8\% - 6\%$ using a Boltzmann parameterization, i.e. $\frac{1}{m_t^2} \cdot \frac{d^2N}{dm_t dy} = \frac{A_B(y)}{m_p} \cdot e^{\frac{m_t - m_p}{T_B(y)}}$. All errors are statistical.

y	$T_B(GeV)$	$A_B\left(\frac{c^4}{GeV^2}\right)$	$\frac{dn}{dy}$
2.95	0.0559 ± 0.0011	1419.4 ± 43.2	24.62 ± 0.49
3.05	0.0564 ± 0.0011	1200.6 ± 37.1	22.46 ± 0.38
3.15	0.0537 ± 0.0011	1101.4 ± 34.4	18.58 ± 0.34
3.25	0.0514 ± 0.0010	898.69 ± 28.45	14.28 ± 0.28
3.35	0.0482 ± 0.0010	817.09 ± 25.02	11.52 ± 0.25
3.45	0.0495 ± 0.0011	606.02 ± 20.93	8.90 ± 0.20
3.55	0.0451 ± 0.0011	514.45 ± 18.16	6.62 ± 0.19
3.65	0.0466 ± 0.0011	393.32 ± 14.74	5.18 ± 0.16
3.75	0.0440 ± 0.0012	294.23 ± 12.04	3.70 ± 0.14
3.85	0.0402 ± 0.0011	258.96 ± 10.84	2.58 ± 0.11
3.95	0.0392 ± 0.0013	182.82 ± 8.48	1.77 ± 0.08
4.05	0.0309 ± 0.0014	148.54 ± 7.83	0.99 ± 0.07
4.15	0.0221 ± 0.0016	116.51 ± 6.78	0.62 ± 0.05
4.25	0.0302 ± 0.0027	59.38 ± 4.83	0.40 ± 0.04
4.35	0.0225 ± 0.0025	60.20 ± 4.60	0.25 ± 0.04

Table B.17: Tabulated results for pi plus at an exclusive centrality of $8\% - 6\%$ using a Boltzmann parameterization over the first 300MeV/c in p_t. All errors are statistical.

y	$T_B (GeV)$	$A_B \left(\frac{c^4}{GeV^2}\right)$
2.95	0.0618 ± 0.0166	1190.7 ± 1197.1
3.05	0.0819 ± 0.0051	454.22 ± 101.32
3.15	0.0764 ± 0.0054	388.17 ± 105.46
3.25	0.0800 ± 0.0064	257.37 ± 74.14
3.35	0.0624 ± 0.0125	478.61 ± 392.89
3.45	0.0725 ± 0.0184	191.80 ± 181.08

Table B.18: Tabulated results for pi plus at an exclusive centrality of $8\% - 6\%$ using a Boltzmann parameterization over $300 MeV/c \leq p_t \leq 600 MeV/c$.

y	$T_B(GeV)$	$A_B\left(\frac{c^4}{GeV^2}\right)$	$\frac{dn}{dy}$
2.95	0.0636 ± 0.0016	921.63 ± 36.68	
3.05	0.0644 ± 0.0017	767.05 ± 30.82	18.51 ± 0.41
3.15	0.0645 ± 0.0017	629.12 ± 25.41	15.51 ± 0.41
3.25	0.0638 ± 0.0016	539.65 ± 22.26	12.02 ± 0.26
3.35	0.0605 ± 0.0015	489.11 ± 20.34	9.66 ± 0.22
3.45	0.0574 ± 0.0016	428.54 ± 19.37	7.77 ± 0.20
3.55	0.0529 ± 0.0019	367.48 ± 16.99	5.80 ± 0.18
3.65	0.0494 ± 0.0023	304.37 ± 16.24	4.42 ± 0.13
3.75	0.0507 ± 0.0028	250.25 ± 14.98	3.60 ± 0.11
3.85	0.0472 ± 0.0038	210.72 ± 13.60	2.74 ± 0.11
3.95	0.0511 ± 0.0076	153.25 ± 11.59	2.21 ± 0.11
4.05	0.0410 ± 0.0095	133.77 ± 12.36	1.38 ± 0.10

Table B.19: Tabulated results for pi plus at an exclusive centrality of $8\% - 6\%$ using a Boltzmann parameterization over the first 300MeV/c in p_t. All errors are statistical.

$\mathbf{y}$	$T_B(GeV)$	$A_B\left(\frac{c^4}{GeV^2}\right)$
3.05	0.0992 ± 0.0098	305.05 ± 99.35
3.15	0.0953 ± 0.0029	230.16 ± 196.90

Table B.20: Tabulated results for pi plus at an exclusive centrality of $8\% - 6\%$ using a Boltzmann parameterization over $300MeV/c \leq p_t \leq 600MeV/c$.

y	$T_B(GeV)$	$A_B\left(\frac{c^4}{GeV^2}\right)$	$\frac{dn}{dy}$
2.15	0.3819 ± 0.0951	149.73 ± 4.77	
2.25	0.2849 ± 0.0368	160.51 ± 4.48	
2.35	0.2556 ± 0.0211	159.47 ± 4.02	64.22 ± 0.59
2.45	0.2078 ± 0.0100	171.24 ± 3.83	51.34 ± 0.48
2.55	0.1905 ± 0.0056	172.25 ± 3.32	44.94 ± 0.45
2.65	0.1646 ± 0.0032	176.21 ± 3.08	38.67 ± 0.42
2.75	0.1449 ± 0.0021	182.58 ± 3.21	34.09 ± 0.40
2.85	0.1299 ± 0.0016	182.10 ± 3.05	29.98 ± 0.35
2.95	0.1202 ± 0.0020	171.47 ± 4.90	26.11 ± 0.31
3.05	0.1110 ± 0.0025	149.69 ± 5.53	21.48 ± 0.29
3.15	0.0925 ± 0.0029	142.06 ± 7.07	16.83 ± 0.23
3.25	0.0732 ± 0.0032	123.49 ± 7.80	10.75 ± 0.18
3.35	0.0851 ± 0.0190	69.25 ± 12.22	6.41 ± 0.21
3.45	0.0825 ± 0.0364	53.33 ± 6.88	3.93 ± 0.25

Table B.21: Tabulated results for protons at an exclusive centrality of $6\% - 4\%$ using a Boltzmann parameterization, i.e. $\frac{1}{m_t^2} \cdot \frac{d^2N}{dm_t dy} = \frac{A_B(y)}{m_p} \cdot e^{\frac{m_t - m_p}{T_B(y)}}$. All errors are statistical.

y	$T_B(GeV)$	$A_B\left(\frac{c^4}{GeV^2}\right)$	$\frac{dn}{dy}$
2.95	0.0567 ± 0.0012	1412.0 ± 44.3	26.44 ± 0.53
3.05	0.0572 ± 0.0011	1237.7 ± 37.1	23.58 ± 0.39
3.15	0.0536 ± 0.0011	1107.4 ± 35.5	19.03 ± 0.35
3.25	0.0540 ± 0.0011	853.43 ± 26.77	14.66 ± 0.29
3.35	0.0501 ± 0.0010	776.76 ± 24.73	11.54 ± 0.25
3.45	0.0498 ± 0.0011	619.62 ± 20.74	8.98 ± 0.21
3.55	0.0455 ± 0.0012	535.58 ± 18.65	6.88 ± 0.20
3.65	0.0460 ± 0.0011	378.47 ± 14.52	4.88 ± 0.15
3.75	0.0432 ± 0.0011	306.53 ± 12.26	3.56 ± 0.13
3.85	0.0401 ± 0.0012	267.42 ± 11.19	2.55 ± 0.11
3.95	0.0402 ± 0.0017	163.27 ± 8.70	1.51 ± 0.08
4.05	0.0330 ± 0.0014	156.16 ± 7.95	1.05 ± 0.07
4.15	0.0313 ± 0.0036	111.25 ± 6.93	0.67 ± 0.06
4.25	0.0358 ± 0.0026	62.91 ± 4.66	0.48 ± 0.06
4.35	0.0267 ± 0.0029	46.92 ± 4.06	0.25 ± 0.04
4.45	0.0379 ± 0.0127	21.45 ± 3.19	0.11 ± 0.04

Table B.22: Tabulated results for pi plus at an exclusive centrality of $6\% - 4\%$ using a Boltzmann parameterization over the first 300MeV/c in p_t. All errors are statistical.

y	$T_B(GeV)$	$A_B\left(\frac{c^4}{GeV^2}\right)$
2.95	0.0871 ± 0.0027	469.68 ± 408.26
3.05	0.0845 ± 0.0043	433.83 ± 79.10
3.15	0.0800 ± 0.0048	393.19 ± 88.18
3.25	0.0774 ± 0.0085	312.34 ± 126.48
3.35	0.0658 ± 0.0039	406.57 ± 94.60
3.45	0.0662 ± 0.0161	272.55 ± 262.66

Table B.23: Tabulated results for pi plus at an exclusive centrality of $6\% - 4\%$ using a Boltzmann parameterization over $300MeV/c \leq p_t \leq 600MeV/c$.

y	$T_B(GeV)$	$A_B\left(\frac{c^4}{GeV^2}\right)$	$\frac{dn}{dy}$
2.95	0.0654 ± 0.0016	943.30 ± 36.42	23.21 ± 0.57
3.05	0.0652 ± 0.0017	786.35 ± 31.39	19.41 ± 0.44
3.15	0.0653 ± 0.0017	655.82 ± 26.76	16.05 ± 0.45
3.25	0.0609 ± 0.0014	597.67 ± 23.53	12.29 ± 0.26
3.35	0.0616 ± 0.0016	514.42 ± 21.65	10.49 ± 0.24
3.45	0.0575 ± 0.0016	447.65 ± 20.06	8.22 ± 0.21
3.55	0.0526 ± 0.0017	409.43 ± 18.52	6.33 ± 0.19
3.65	0.0467 ± 0.0018	337.22 ± 17.19	4.49 ± 0.13
3.75	0.0473 ± 0.0023	291.34 ± 16.29	3.71 ± 0.12
3.85	0.0445 ± 0.0038	227.86 ± 14.92	2.81 ± 0.11
3.95	0.0420 ± 0.0043	196.88 ± 11.74	1.99 ± 0.08
4.05	0.0368 ± 0.0065	131.79 ± 11.07	1.21 ± 0.07
4.15	—-	117.04 ± 12.39	

Table B.24: Tabulated results for pi plus at an exclusive centrality of $6\% - 4\%$ using a Boltzmann parameterization over the first 300MeV/c in p_t. All errors are statistical.

y	$T_B(GeV)$	$A_B\left(\frac{c^4}{GeV^2}\right)$
2.95	0.0787 ± 0.0023	562.95 ± 501.84
3.05	0.0925 ± 0.0115	268.04 ± 96.27
3.15	0.0848 ± 0.0169	351.75 ± 220.16

Table B.25: Tabulated results for pi plus at an exclusive centrality of $6\% - 4\%$ using a Boltzmann parameterization over $300MeV/c \leq p_t \leq 600MeV/c$.

y	$T_B(GeV)$	$A_B\left(\frac{c^4}{GeV^2}\right)$	$\frac{dn}{dy}$
2.15	0.3753 ± 0.0872	159.92 ± 4.89	
2.25	0.2945 ± 0.0398	168.65 ± 4.70	
2.35	0.2403 ± 0.0123	172.14 ± 3.54	63.72 ± 0.51
2.45	0.2139 ± 0.0116	179.97 ± 4.26	56.26 ± 0.53
2.55	0.1786 ± 0.0051	182.87 ± 3.57	43.76 ± 0.45
2.65	0.1670 ± 0.0034	176.77 ± 3.19	39.23 ± 0.43
2.75	0.1447 ± 0.0020	182.53 ± 3.03	33.90 ± 0.39
2.85	0.1303 ± 0.0016	170.81 ± 2.83	28.13 ± 0.34
2.95	0.1212 ± 0.0022	152.00 ± 4.58	23.22 ± 0.29
3.05	0.1036 ± 0.0026	142.99 ± 6.40	18.80 ± 0.26
3.15	0.1016 ± 0.0040	104.48 ± 6.34	14.16 ± 0.22
3.25	0.0890 ± 0.0116	76.25 ± 12.69	9.15 ± 0.17
3.35	0.0670 ± 0.0094	61.81 ± 7.08	4.61 ± 0.13
3.45	0.0649 ± 0.0215	81.26 ± 5.35	2.70 ± 0.14

Table B.26: Tabulated results for protons at an exclusive centrality of $4\% - 2\%$ using a Boltzmann parameterization, i.e. $\frac{1}{m_t^2} \cdot \frac{d^2N}{dm_t dy} = \frac{A_B(y)}{m_p} \cdot e^{\frac{m_t - m_p}{T_B(y)}}$. All errors are statistical.

y	$T_B(GeV)$	$A_B\left(\frac{c^4}{GeV^2}\right)$	$\frac{dn}{dy}$
2.95	0.0567 ± 0.0011	1481.5 ± 44.6	27.23 ± 0.54
3.05	0.0576 ± 0.0011	1218.5 ± 37.8	23.55 ± 0.40
3.15	0.0550 ± 0.0011	1060.4 ± 33.4	18.72 ± 0.34
3.25	0.0536 ± 0.0011	900.71 ± 27.40	14.86 ± 0.29
3.35	0.0513 ± 0.0010	810.40 ± 24.94	12.27 ± 0.26
3.45	0.0503 ± 0.0011	636.10 ± 20.77	9.64 ± 0.22
3.55	0.0482 ± 0.0013	479.25 ± 17.52	7.00 ± 0.20
3.65	0.0482 ± 0.0011	390.50 ± 14.26	5.41 ± 0.16
3.75	0.0408 ± 0.0010	356.03 ± 13.62	3.61 ± 0.13
3.85	0.0402 ± 0.0011	269.77 ± 10.82	2.63 ± 0.11
3.95	0.0372 ± 0.0014	200.77 ± 9.02	1.70 ± 0.10
4.05	0.0335 ± 0.0013	160.58 ± 7.73	1.20 ± 0.08
4.15	0.0265 ± 0.0027	114.03 ± 6.68	0.64 ± 0.06
4.25	0.0306 ± 0.0022	68.96 ± 4.81	0.45 ± 0.05
4.35	0.0262 ± 0.0030	62.45 ± 4.58	0.31 ± 0.04
4.45	0.0156 ± 0.0029	40.12 ± 4.71	0.12 ± 0.04

Table B.27: Tabulated results for pi plus at an exclusive centrality of $4\% - 2\%$ using a Boltzmann parameterization over the first 300MeV/c in p_t. All errors are statistical.

y	$T_B(GeV)$	$A_B\left(\frac{c^4}{GeV^2}\right)$
2.95	0.0729 ± 0.0196	814.34 ± 723.80
3.05	0.0853 ± 0.0069	437.81 ± 121.03
3.15	0.0773 ± 0.0045	437.96 ± 98.50
3.25	0.0741 ± 0.0065	337.89 ± 111.82
3.35	0.0686 ± 0.0149	345.31 ± 278.75
3.45	0.0779 ± 0.0201	180.90 ± 159.69
3.55	0.0648 ± 0.0239	241.82 ± 340.29

Table B.28: Tabulated results for pi plus at an exclusive centrality of $4\% - 2\%$ using a Boltzmann parameterization over $300MeV/c \leq p_t \leq 600MeV/c$.

y	$T_B(GeV)$	$A_B\left(\frac{c^4}{GeV^2}\right)$	$\frac{dn}{dy}$
2.95	0.0648 ± 0.0016	1010.2 ± 39.0	23.67 ± 0.77
3.05	0.0656 ± 0.0016	826.05 ± 32.28	20.58 ± 0.46
3.15	0.0641 ± 0.0017	733.22 ± 29.58	17.31 ± 0.49
3.25	0.0616 ± 0.0015	650.29 ± 25.79	13.92 ± 0.51
3.35	0.0572 ± 0.0015	565.97 ± 24.25	10.15 ± 0.23
3.45	0.0576 ± 0.0015	459.27 ± 19.98	8.09 ± 0.20
3.55	0.0532 ± 0.0019	425.50 ± 19.55	6.63 ± 0.19
3.65	0.0525 ± 0.0021	336.32 ± 17.49	5.05 ± 0.13
3.75	0.0488 ± 0.0024	276.59 ± 16.48	3.70 ± 0.11
3.85	0.0412 ± 0.0030	249.43 ± 15.73	2.61 ± 0.11
3.95	0.0449 ± 0.0082	201.49 ± 27.38	2.37 ± 0.14
4.05	0.0409 ± 0.0100	147.85 ± 14.00	1.52 ± 0.11
4.15	0.0450 ± 0.0157	120.42 ± 12.91	1.40 ± 0.14

Table B.29: Tabulated results for pi plus at an exclusive centrality of $4\% - 2\%$ using a Boltzmann parameterization over the first 300MeV/c in p_t. All errors are statistical.

y	$T_B(GeV)$	$A_B\left(\frac{c^4}{GeV^2}\right)$
2.95	0.0903 ± 0.0291	402.47 ± 350.44
3.05	0.0913 ± 0.0104	382.80 ± 133.62
3.15	0.0928 ± 0.0203	263.29 ± 166.60
3.25	0.0823 ± 0.0223	295.44 ± 233.75

Table B.30: Tabulated results for pi plus at an exclusive centrality of $4\% - 2\%$ using a Boltzmann parameterization over $300MeV/c \leq p_t \leq 600MeV/c$.

y	$T_B(GeV)$	$A_B\left(\frac{c^4}{GeV^2}\right)$	$\frac{dn}{dy}$
2.15	0.2694 ± 0.0465	177.16 ± 5.51	
2.25	0.3284 ± 0.0511	166.92 ± 4.78	
2.35	0.2550 ± 0.0210	174.32 ± 4.35	69.77 ± 0.73
2.45	0.2105 ± 0.0102	185.74 ± 4.13	56.84 ± 0.52
2.55	0.1791 ± 0.0054	182.92 ± 3.69	44.68 ± 0.47
2.65	0.1605 ± 0.0033	175.40 ± 3.27	37.08 ± 0.43
2.75	0.1445 ± 0.0023	168.64 ± 3.12	31.20 ± 0.38
2.85	0.1323 ± 0.0020	150.23 ± 3.38	25.28 ± 0.32
2.95	0.1172 ± 0.0024	136.26 ± 4.67	19.95 ± 0.28
3.05	0.1027 ± 0.0030	108.79 ± 2.03	15.09 ± 0.23
3.15	0.0846 ± 0.0035	102.00 ± 6.68	11.17 ± 0.19
3.25	0.0838 ± 0.0068	63.24 ± 5.98	6.57 ± 0.14
3.35	0.0505 ± 0.0037	59.92 ± 3.44	3.21 ± 0.10
3.45	0.0399 ± 0.0150	37.72 ± 7.64	1.39 ± 0.11

Table B.31: Tabulated results for protons at a centrality of 2% inclusive using a Boltzmann parameterization, i.e. $\frac{1}{m_t^2} \cdot \frac{d^2N}{dm_t dy} = \frac{A_B(y)}{m_p} \cdot e^{\frac{m_t - m_p}{T_B(y)}}$. All errors are statistical.

y	$T_B(GeV)$	$A_B\left(\frac{c^4}{GeV^2}\right)$	$\frac{dn}{dy}$
2.95	0.0584 ± 0.0012	1426.5 ± 45.7	26.96 ± 0.58
3.05	0.0576 ± 0.0011	1247.7 ± 38.7	23.78 ± 0.41
3.15	0.0547 ± 0.0011	1085.0 ± 34.1	18.95 ± 0.35
3.25	0.0541 ± 0.0011	875.65 ± 27.31	14.53 ± 0.29
3.35	0.0523 ± 0.0011	781.97 ± 24.76	12.05 ± 0.26
3.45	0.0504 ± 0.0010	638.75 ± 20.47	9.23 ± 0.22
3.55	0.0469 ± 0.0013	522.15 ± 18.50	6.81 ± 0.20
3.65	0.0438 ± 0.0011	434.20 ± 15.84	5.21 ± 0.16
3.75	0.0419 ± 0.0011	341.41 ± 13.15	3.57 ± 0.14
3.85	0.0378 ± 0.0012	279.38 ± 11.48	2.47 ± 0.12
3.95	0.0388 ± 0.0016	183.56 ± 8.73	1.78 ± 0.10
4.05	0.0326 ± 0.0012	170.70 ± 8.03	1.23 ± 0.08
4.15	0.0251 ± 0.0017	120.39 ± 6.75	0.67 ± 0.06
4.25	0.0353 ± 0.0023	66.22 ± 4.89	0.54 ± 0.05
4.35	0.0216 ± 0.0025	66.87 ± 5.09	0.27 ± 0.04

Table B.32: Tabulated results for pi plus at a centrality of 2% inclusive using a Boltzmann parameterization over the first 300MeV/c in p_t. All errors are statistical.

y	$T_B(GeV)$	$A_B\left(\frac{c^4}{GeV^2}\right)$
2.95	0.0847 ± 0.0260	508.05 ± 451.78
3.05	0.0722 ± 0.0040	773.32 ± 170.76
3.15	0.0807 ± 0.0068	353.15 ± 108.95
3.25	0.0794 ± 0.0061	271.24 ± 75.79

Table B.33: Tabulated results for pi plus at a centrality of 2% inclusive using a Boltzmann parameterization over $300MeV/c \leq p_t \leq 600MeV/c$.

y	$T_B(GeV)$	$A_B\left(\frac{c^4}{GeV^2}\right)$	$\frac{dn}{dy}$
2.95	0.0656 ± 0.0018	1014.5 ± 40.7	
3.05	0.0632 ± 0.0016	894.31 ± 35.49	21.87 ± 0.52
3.15	0.0622 ± 0.0016	747.99 ± 30.47	17.50 ± 0.53
3.25	0.0620 ± 0.0015	670.19 ± 26.71	13.77 ± 0.29
3.35	0.0584 ± 0.0015	603.24 ± 25.34	11.24 ± 0.25
3.45	0.0569 ± 0.0015	489.86 ± 21.44	8.61 ± 0.22
3.55	0.0521 ± 0.0018	421.55 ± 20.24	6.39 ± 0.19
3.65	0.0489 ± 0.0019	366.94 ± 18.57	4.96 ± 0.13
3.75	0.0475 ± 0.0021	290.65 ± 16.33	3.72 ± 0.12
3.85	0.0459 ± 0.0038	227.09 ± 15.08	2.75 ± 0.11
3.95	0.0419 ± 0.0053	195.54 ± 14.43	2.04 ± 0.10
4.05	0.0447 ± 0.0119	143.30 ± 13.29	1.60 ± 0.13
4.15	0.0289 ± 0.0049	140.82 ± 11.12	0.85 ± 0.05

Table B.34: Tabulated results for pi plus at a centrality of 2% inclusive using a Boltzmann parameterization over the first 300MeV/c in p_t. All errors are statistical.

y	$T_B(GeV)$	$A_B\left(\frac{c^4}{GeV^2}\right)$
3.05	0.1043 ± 0.0141	270.96 ± 98.23
3.15	0.0908 ± 0.0201	312.83 ± 199.34

Table B.35: Tabulated results for pi plus at a centrality of 2% inclusive using a Boltzmann parameterization over $300MeV/c \leq p_t \leq 600MeV/c$.

y	$T_B(GeV)$	$A_B\left(\frac{c^4}{GeV^2}\right)$	$\frac{dn}{dy}$
2.15	0.2367 ± 0.0676	175.41 ± 10.10	
2.25	0.3039 ± 0.0802	164.67 ± 8.75	
2.35	0.2907 ± 0.0506	163.72 ± 7.72	79.97 ± 1.66
2.45	0.2260 ± 0.0237	167.25 ± 7.37	55.94 ± 0.99
2.55	0.1685 ± 0.0093	177.02 ± 6.77	40.04 ± 0.76
2.65	0.1536 ± 0.0069	160.20 ± 6.24	31.38 ± 0.68
2.75	0.1511 ± 0.0058	151.08 ± 5.57	26.66 ± 0.64
2.85	0.1518 ± 0.0069	124.91 ± 5.54	19.76 ± 0.55
2.95	0.1426 ± 0.0109	95.33 ± 7.55	14.94 ± 0.47
3.05	0.1112 ± 0.0126	94.35 ± 10.01	10.19 ± 0.40
3.15	0.1128 ± 0.0135	74.01 ± 7.77	8.47 ± 0.38
3.25	0.1308 ± 0.0323	45.71 ± 5.21	5.92 ± 0.34
3.35	0.0344 ± 0.0065	73.27 ± 10.71	2.50 ± 0.25

Table B.36: Tabulated results for protons at a centrality of 0.5% inclusive using a Boltzmann parameterization, i.e. $\frac{1}{m_t^2} \cdot \frac{d^2N}{dm_t dy} = \frac{A_B(y)}{m_p} \cdot e^{\frac{m_t - m_p}{T_B(y)}}$. All errors are statistical.

y	$T_B(GeV)$	$A_B\left(\frac{c^4}{GeV^2}\right)$	$\frac{dn}{dy}$
2.95	0.0575 ± 0.0022	1341.1 ± 71.6	24.91 ± 1.00
3.05	0.0556 ± 0.0020	1243.7 ± 64.2	22.07 ± 0.71
3.15	0.0522 ± 0.0021	1063.7 ± 58.2	16.56 ± 0.65
3.25	0.0515 ± 0.0019	839.73 ± 47.10	12.43 ± 0.57
3.35	0.0542 ± 0.0023	738.08 ± 41.90	11.91 ± 0.56
3.45	0.0473 ± 0.0021	690.79 ± 37.47	9.06 ± 0.52
3.55	0.0435 ± 0.0032	490.31 ± 36.23	6.04 ± 0.52
3.65	0.0450 ± 0.0031	376.27 ± 28.62	5.05 ± 0.48
3.75	0.0436 ± 0.0031	302.72 ± 24.26	3.35 ± 0.42
3.85	0.0344 ± 0.0030	294.34 ± 23.52	1.97 ± 0.36

Table B.37: Tabulated results for pi plus at a centrality of 0.5% inclusive using a Boltzmann parameterization over the first 300MeV/c in p_t. All errors are statistical.

y	$T_B(GeV)$	$A_B\left(\frac{c^4}{GeV^2}\right)$	$\frac{dn}{dy}$
2.95	0.0687 ± 0.0034	893.12 ± 59.82	19.79 ± 0.88
3.05	0.0622 ± 0.0028	857.42 ± 57.42	18.73 ± 0.68
3.15	0.0630 ± 0.0031	723.16 ± 50.97	16.50 ± 0.63
3.25	0.0648 ± 0.0032	612.79 ± 45.08	13.28 ± 0.54
3.35	0.0620 ± 0.0031	515.93 ± 39.04	11.24 ± 0.47
3.45	0.0616 ± 0.0033	477.40 ± 37.65	9.63 ± 0.44
3.55	0.0404 ± 0.0047	490.92 ± 46.99	4.81 ± 0.40
3.65	0.0421 ± 0.0046	366.96 ± 38.27	4.45 ± 0.27
3.75	0.0496 ± 0.0099	217.46 ± 33.70	3.10 ± 0.24
3.85	0.0440 ± 0.0120	184.69 ± 31.01	2.10 ± 0.22
3.95	0.0249 ± 0.0074	198.25 ± 32.87	1.20 ± 0.14

Table B.38: Tabulated results for pi plus at a centrality of 0.5% inclusive using a Boltzmann parameterization over the first 300MeV/c in p_t. All errors are statistical.

y	$T_B(GeV)$	$A_B\left(\frac{c^4}{GeV^2}\right)$	$\frac{dn}{dy}$
2.25	0.1937 ± 0.0598	193.22 ± 17.77	
2.35	0.5672 ± 0.3170	155.98 ± 12.40	
2.45	0.2268 ± 0.0418	172.56 ± 13.00	53.68 ± 1.64
2.55	0.1910 ± 0.0257	173.33 ± 12.26	38.47 ± 1.25
2.65	0.1800 ± 0.0189	168.64 ± 11.31	28.93 ± 1.02
2.75	0.1744 ± 0.0202	157.35 ± 10.99	19.86 ± 1.00
2.85	0.1773 ± 0.0239	126.45 ± 9.59	15.30 ± 0.88
2.95	0.1237 ± 0.0184	142.25 ± 11.22	10.14 ± 0.78
3.05	0.1042 ± 0.0203	131.58 ± 11.41	7.12 ± 0.71

Table B.39: Tabulated results for protons at a centrality of 0.2% inclusive using a Boltzmann parameterization, i.e. $\frac{1}{m_t^2} \cdot \frac{d^2N}{dm_t dy} = \frac{A_B(y)}{m_p} \cdot e^{\frac{m_t - m_p}{T_B(y)}}$. All errors are statistical.

y	$T_B(GeV)$	$A_B\left(\frac{c^4}{GeV^2}\right)$	$\frac{dn}{dy}$
2.95	0.0887 ± 0.0126	699.89 ± 84.11	24.02 ± 1.46
3.05	0.0693 ± 0.0114	711.37 ± 94.71	22.02 ± 1.46
3.15	0.0556 ± 0.0066	763.14 ± 91.67	14.88 ± 1.45
3.25	0.0662 ± 0.0069	604.28 ± 74.02	11.04 ± 1.22
3.35	0.0532 ± 0.0076	541.45 ± 74.80	10.89 ± 1.17
3.45	0.0512 ± 0.0076	532.12 ± 74.95	6.91 ± 1.08
3.55	0.0640 ± 0.0640	461.32 ± 86.14	3.24 ± 1.09
3.65	0.0569 ± 0.0113	308.66 ± 59.21	2.01 ± 1.06

Table B.40: Tabulated results for pi plus at a centrality of 0.2% inclusive using a Boltzmann parameterization over the first 300MeV/c in p_t. All errors are statistical.

y	$T_B(GeV)$	$A_B\left(\frac{c^4}{GeV^2}\right)$	$\frac{dn}{dy}$
2.95	0.0876 ± 0.0110	703.95 ± 81.68	20.84 ± 1.41
3.05	0.0694 ± 0.0114	711.42 ± 94.65	12.71 ± 1.36
3.15	0.0556 ± 0.0066	763.16 ± 91.64	12.58 ± 1.18
3.25	0.0652 ± 0.0074	610.22 ± 75.98	13.21 ± 0.92
3.35	0.0556 ± 0.0077	529.21 ± 73.36	9.31 ± 0.84
3.45	0.0534 ± 0.0078	511.84 ± 73.95	7.68 ± 0.74
3.55	0.0641 ± 0.0383	460.97 ± 86.05	5.20 ± 1.16
3.65	0.0594 ± 0.0146	293.37 ± 73.29	4.89 ± 0.55

Table B.41: Tabulated results for pi plus at a centrality of 0.2% inclusive using a Boltzmann parameterization over the first 300MeV/c in p_t. All errors are statistical.

Appendix C

Various Spectra

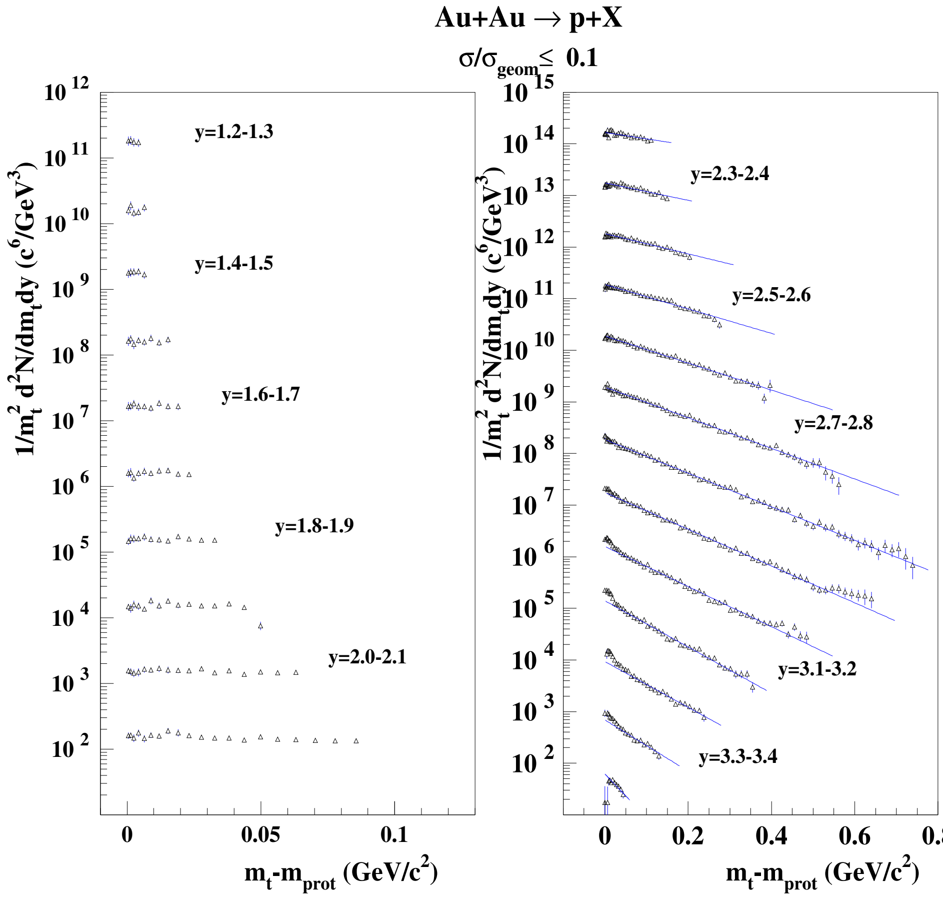

Figure C.1: Measured proton spectra in Au + Au collisions at 10.8 GeV/c and 10% inclusive centrality.

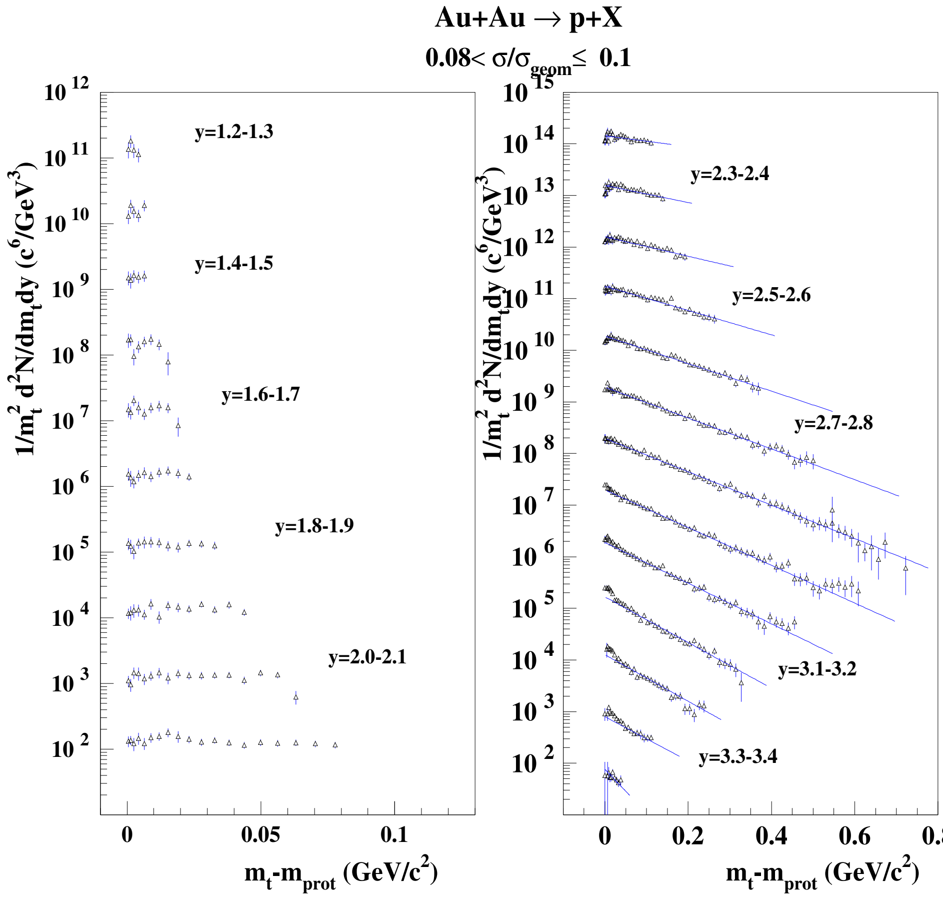

Figure C.2: Measured proton spectra in Au + Au collisions at 10.8 GeV/c and an exclusive centrality of 10-8%.

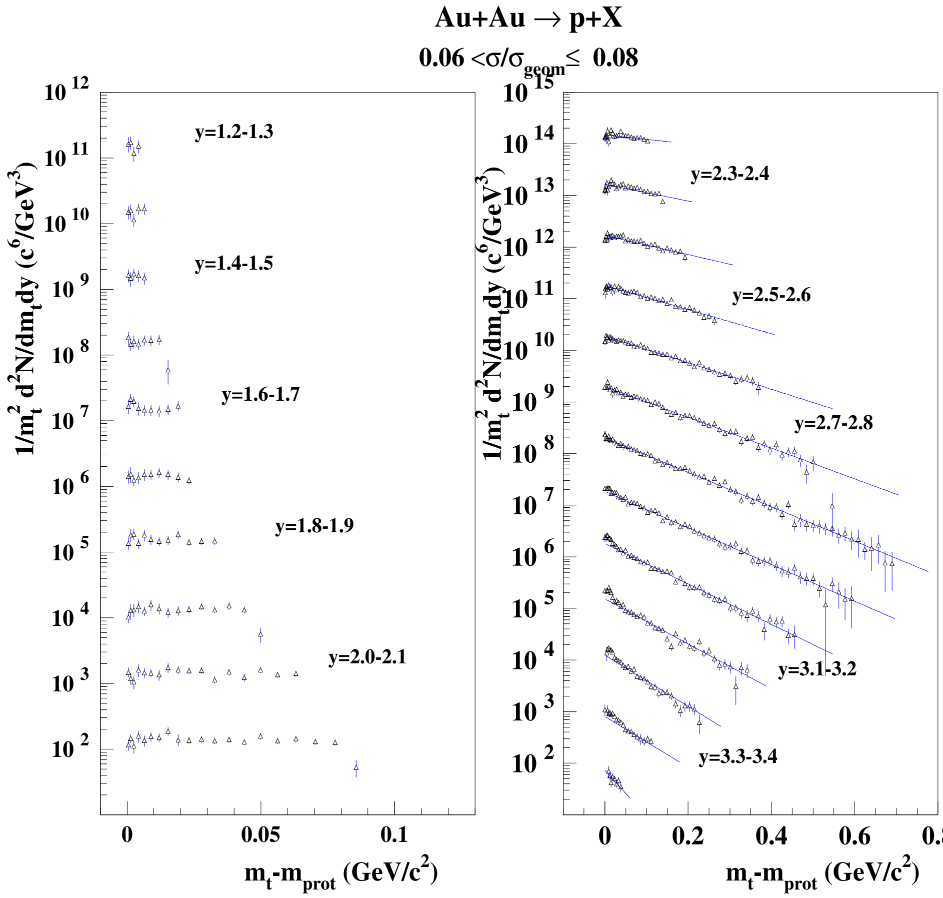

Figure C.3: Measured proton spectra in Au + Au collisions at 10.8 GeV/c and an exclusive centrality of 8-6%.

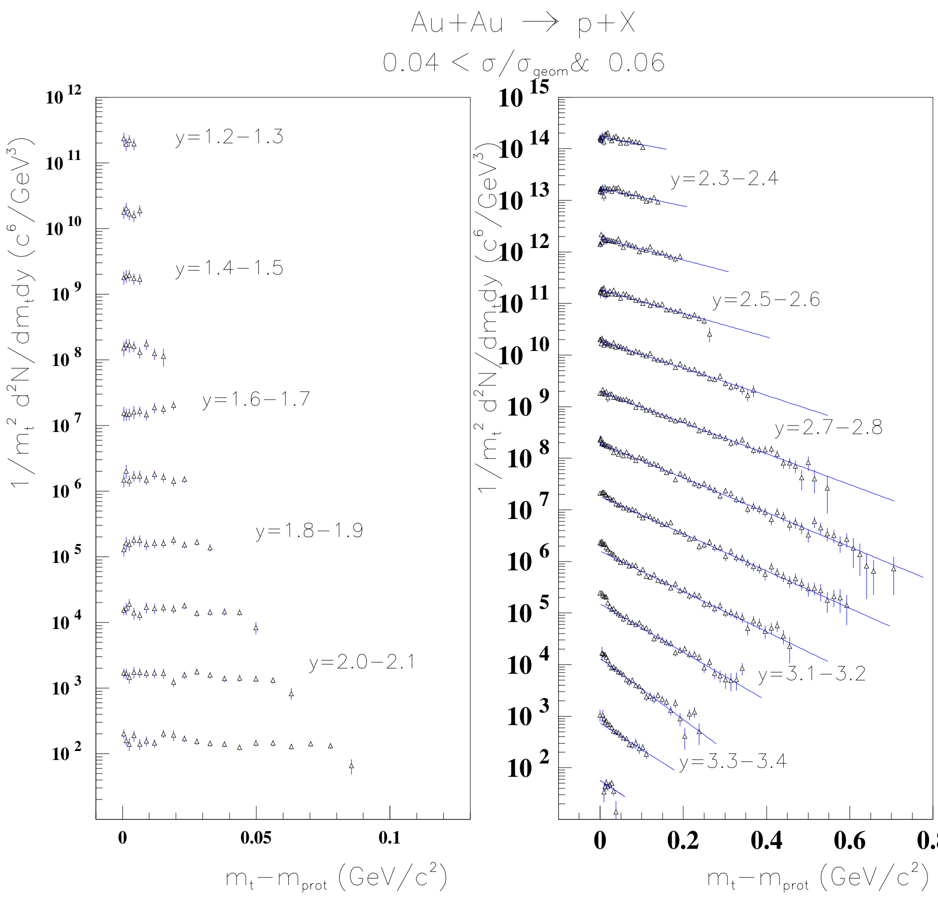

Figure C.4: Measured proton spectra in Au + Au collisions at 10.8 GeV/c and an exclusive centrality of 6-4%.

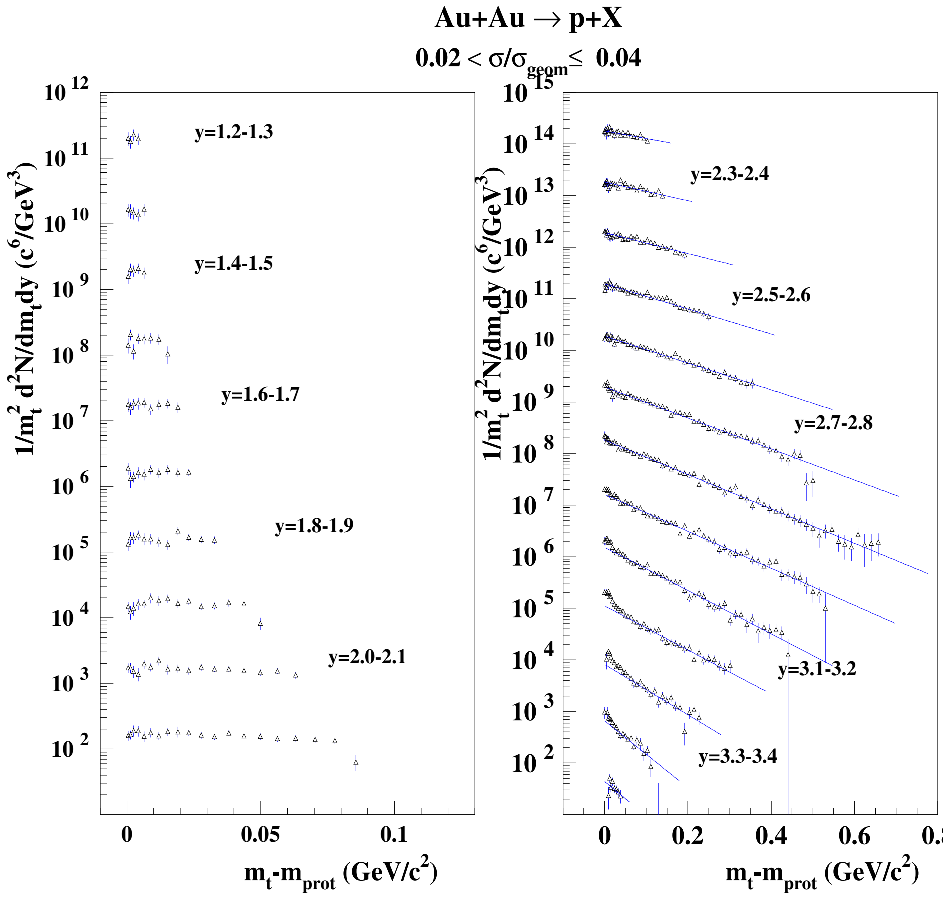

Figure C.5: Measured proton spectra in Au + Au collisions at 10.8 GeV/c and an exclusive centrality of 4-2%.

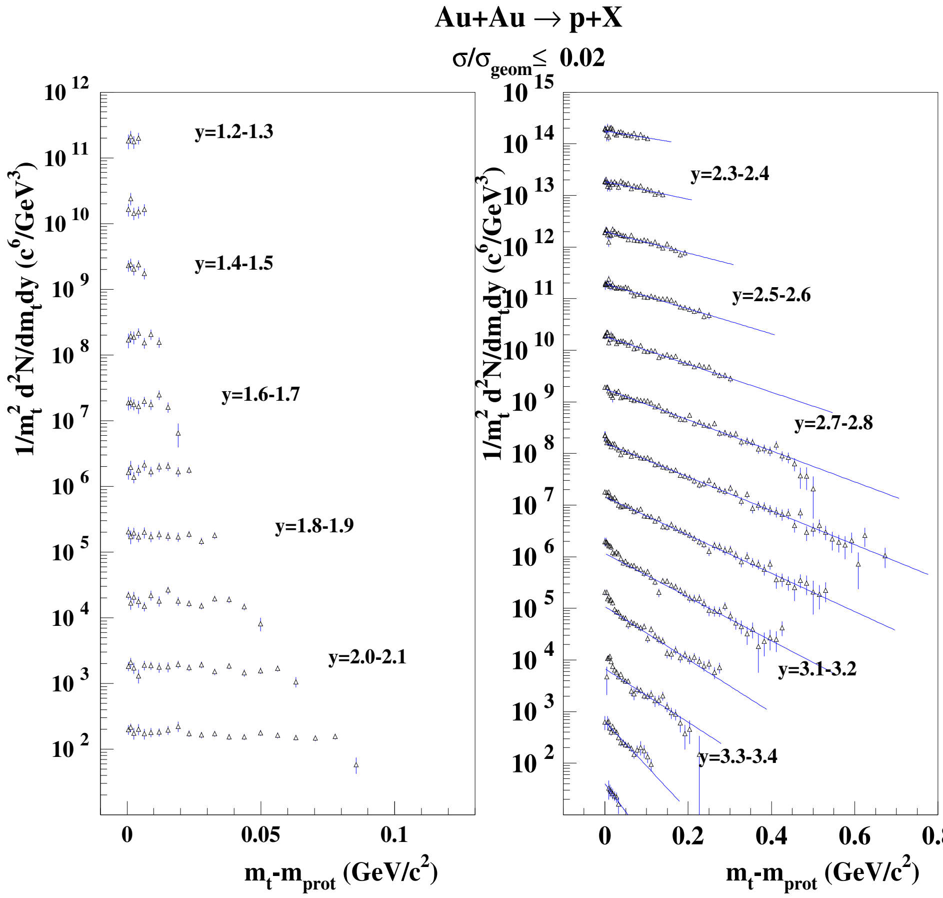

Figure C.6: Measured proton spectra in Au+Au collisions at 10.8 GeV/c and an inclusive centrality of 2%.

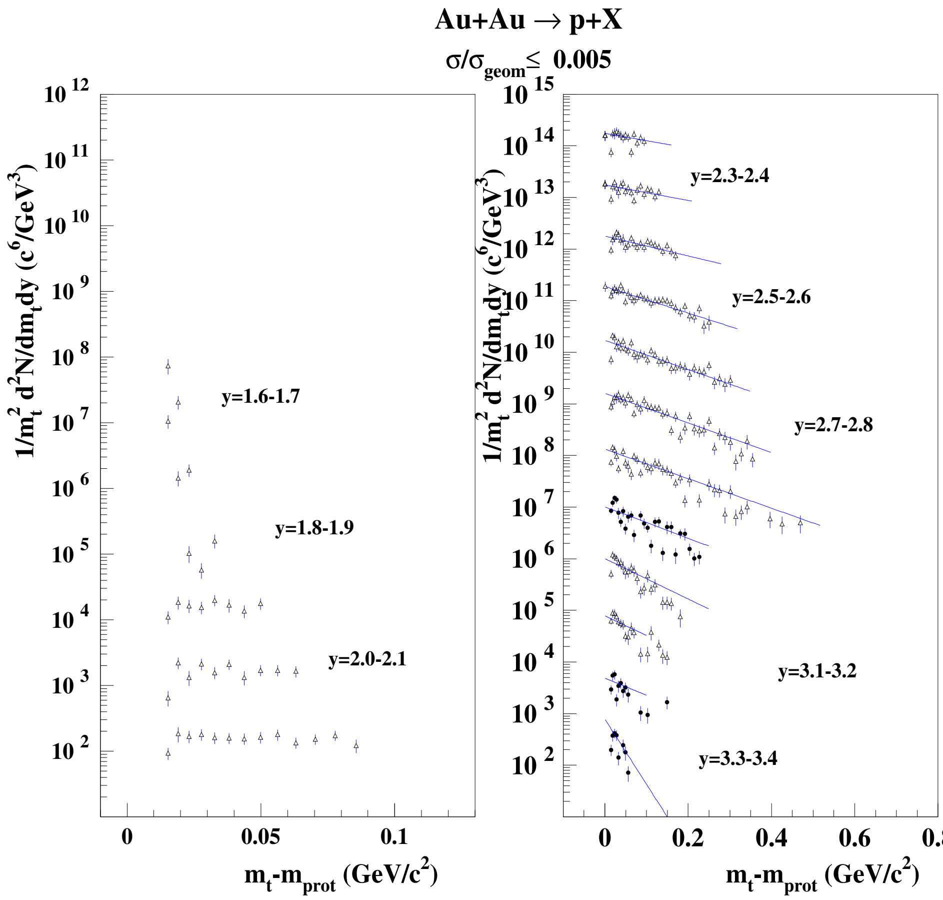

Figure C.7: Measured proton spectra in Au + Au collisions at 10.8 GeV/c and an inclusive centrality of 0.5%.

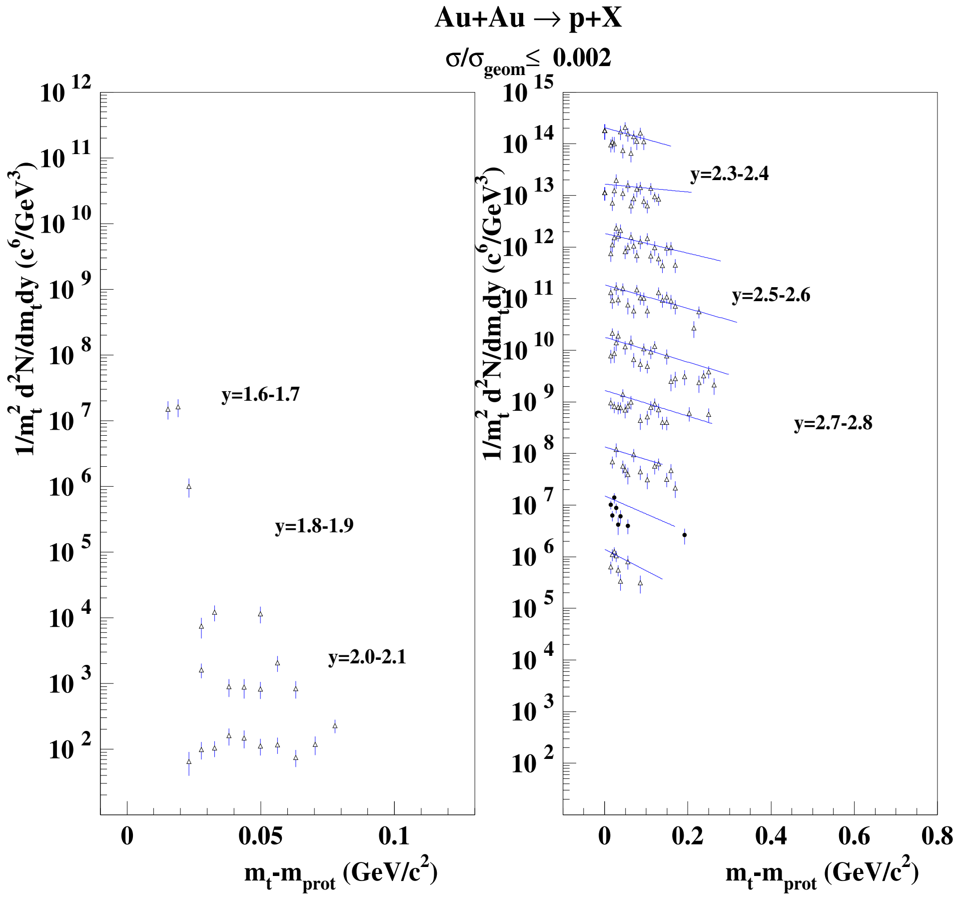

Figure C.8: Measured proton spectra in Au + Au collisions at 10.8 GeV/c and an inclusive centrality of 0.2%.

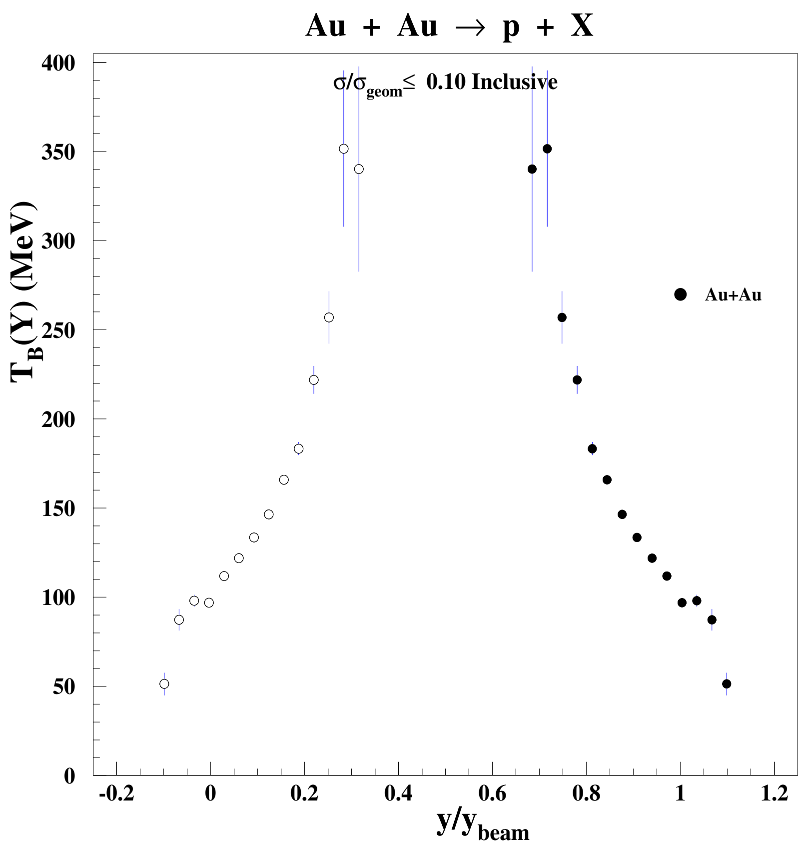

Figure C.9: Measured proton temperature parameters in Au + Au collisions at 10.8 GeV/c and 10% inclusive centrality.

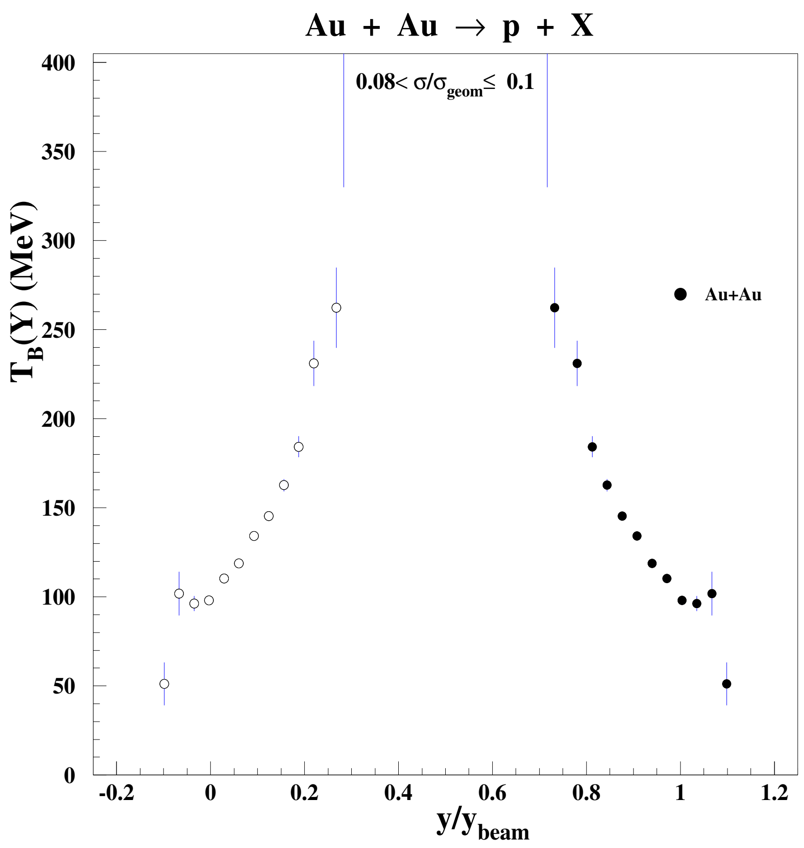

Figure C.10: Measured proton temperature parameters in Au + Au collisions at 10.8 GeV/c and an exclusive centrality of 10-8%.

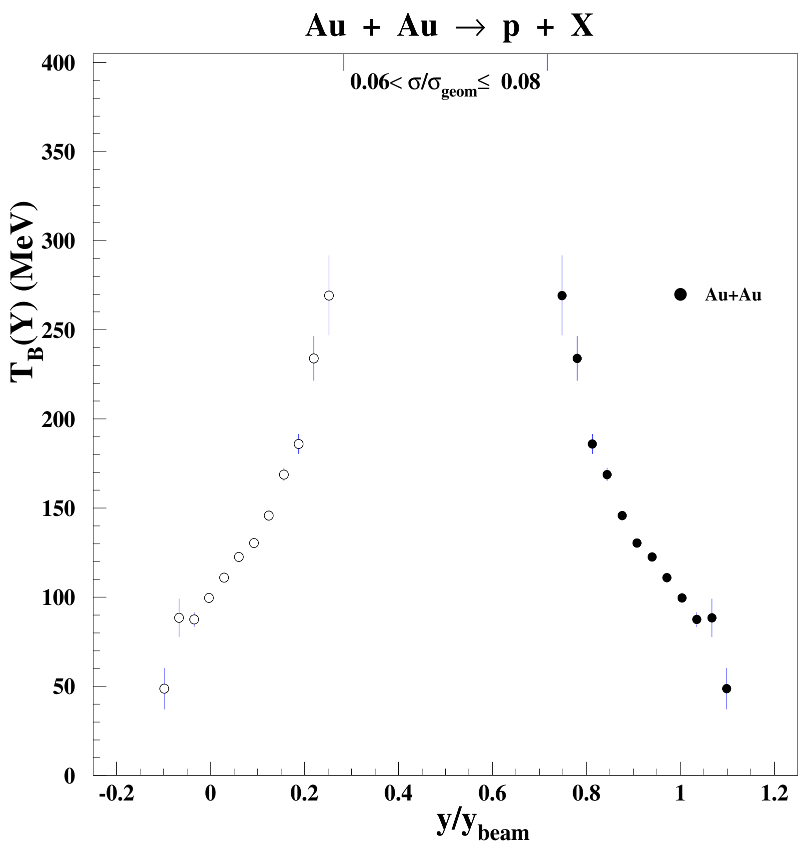

Figure C.11: Measured proton temperature parameters in Au + Au collisions at 10.8 GeV/c and an exclusive centrality of 8-6%.

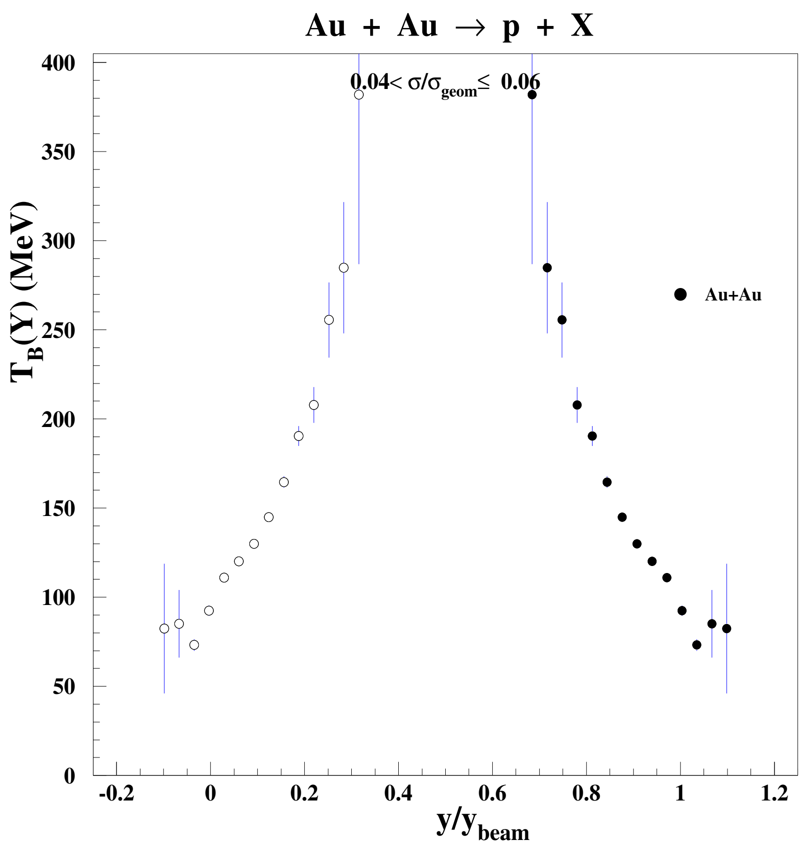

Figure C.12: Measured proton temperature parameters in Au + Au collisions at 10.8 GeV/c and an exclusive centrality of 6-4%.

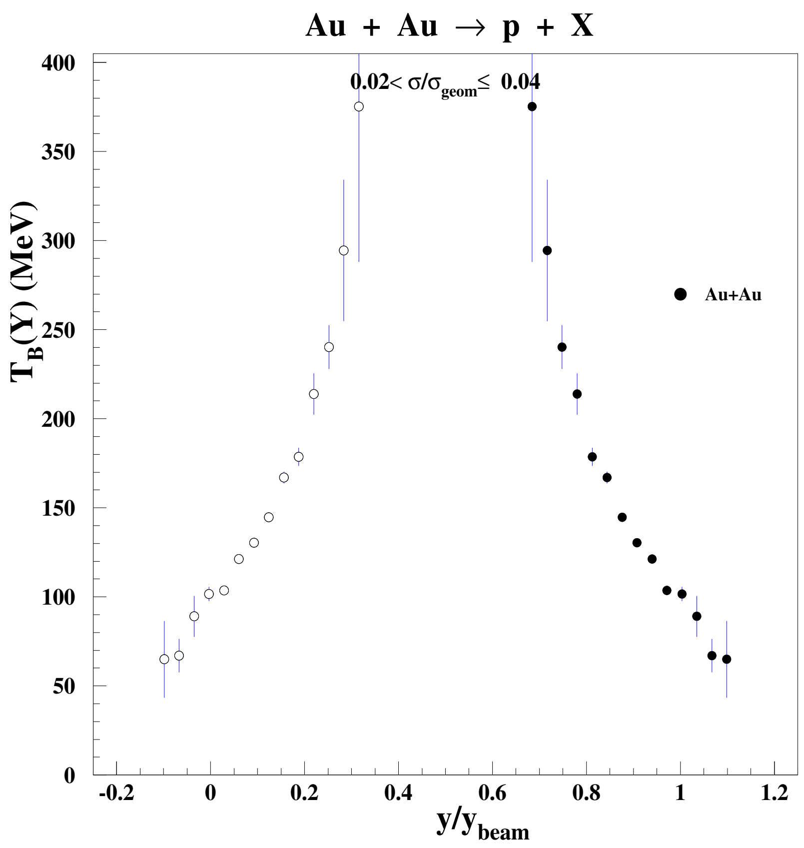

Figure C.13: Measured proton temperature parameters in Au + Au collisions at 10.8 GeV/c and an exclusive centrality of 4-2%.

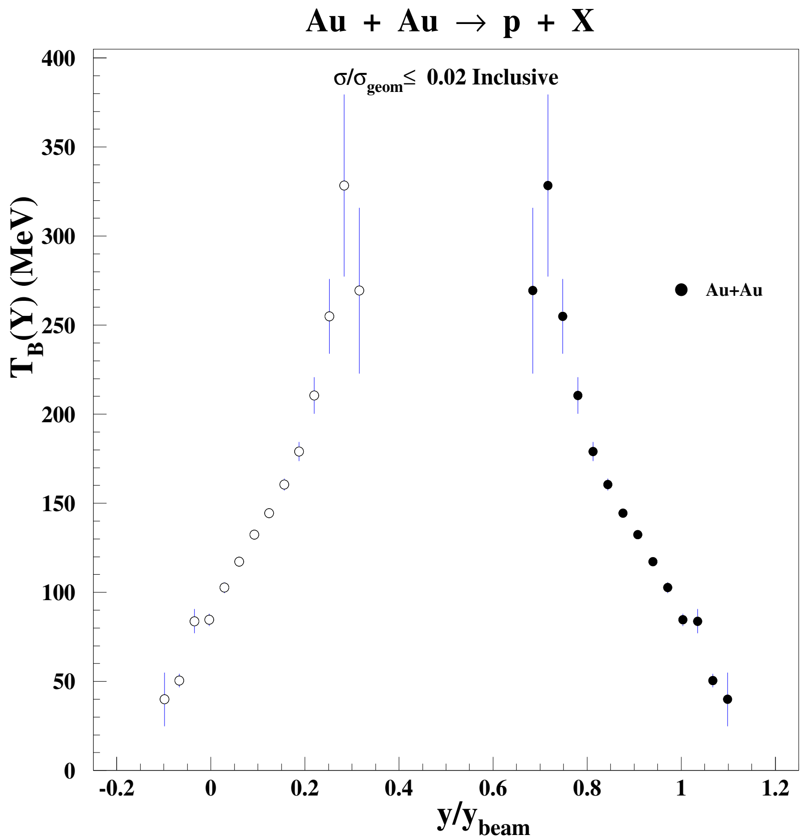

Figure C.14: Measured proton temperature parameters in Au + Au collisions at 10.8 GeV/c and an inclusive centrality of 2%.

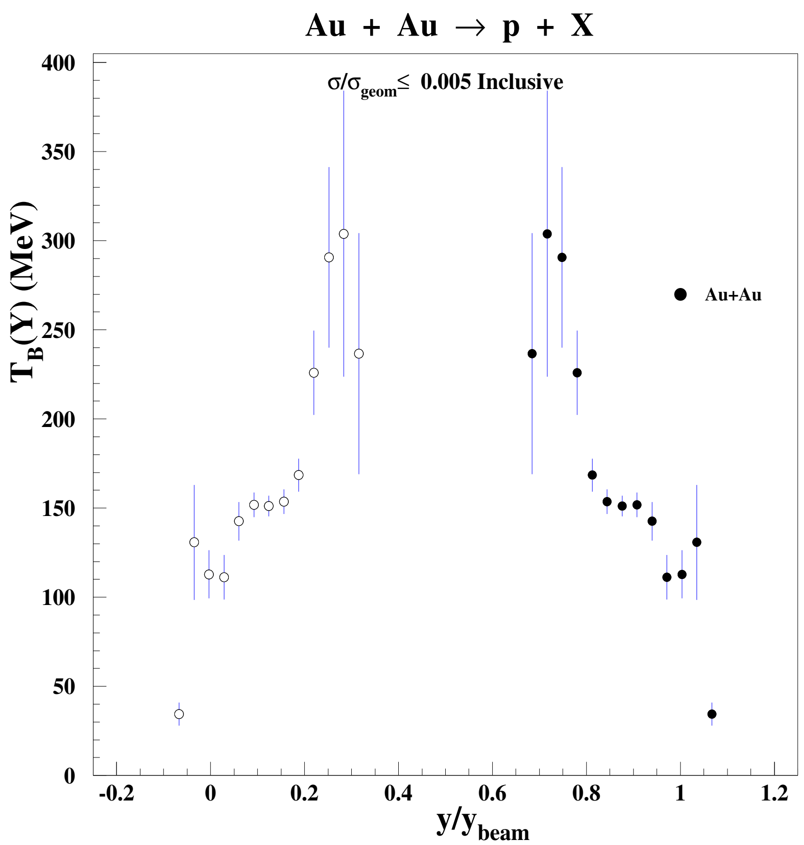

Figure C.15: Measured proton temperature parameters in Au + Au collisions at 10.8 GeV/c and an inclusive centrality of 0.5%.

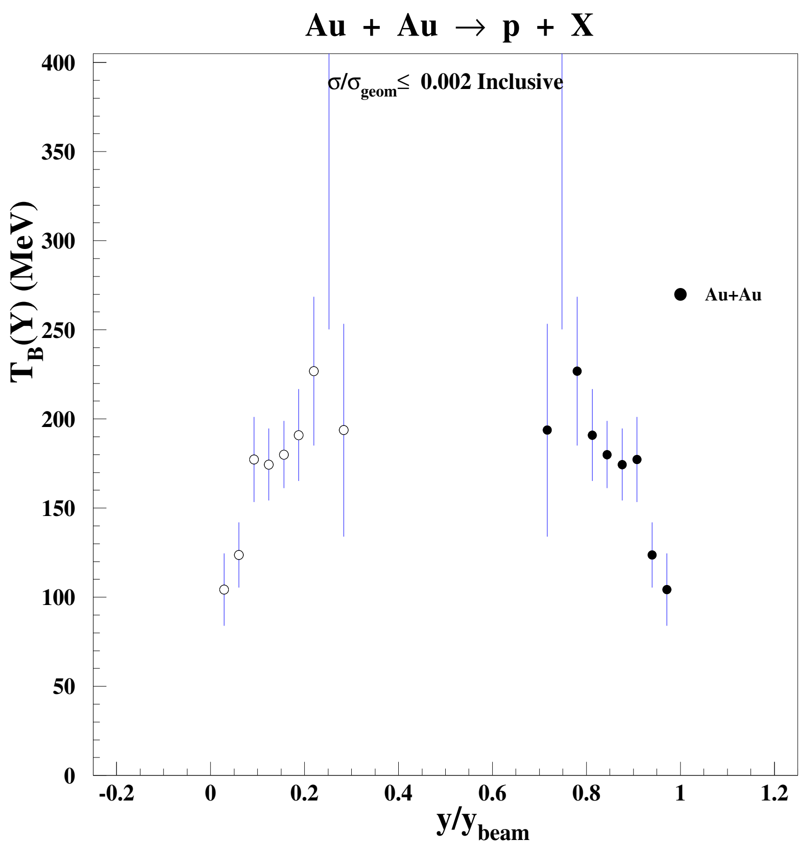

Figure C.16: Measured proton temperature parameters in Au + Au collisions at 10.8 GeV/c and an inclusive centrality of 0.2%.

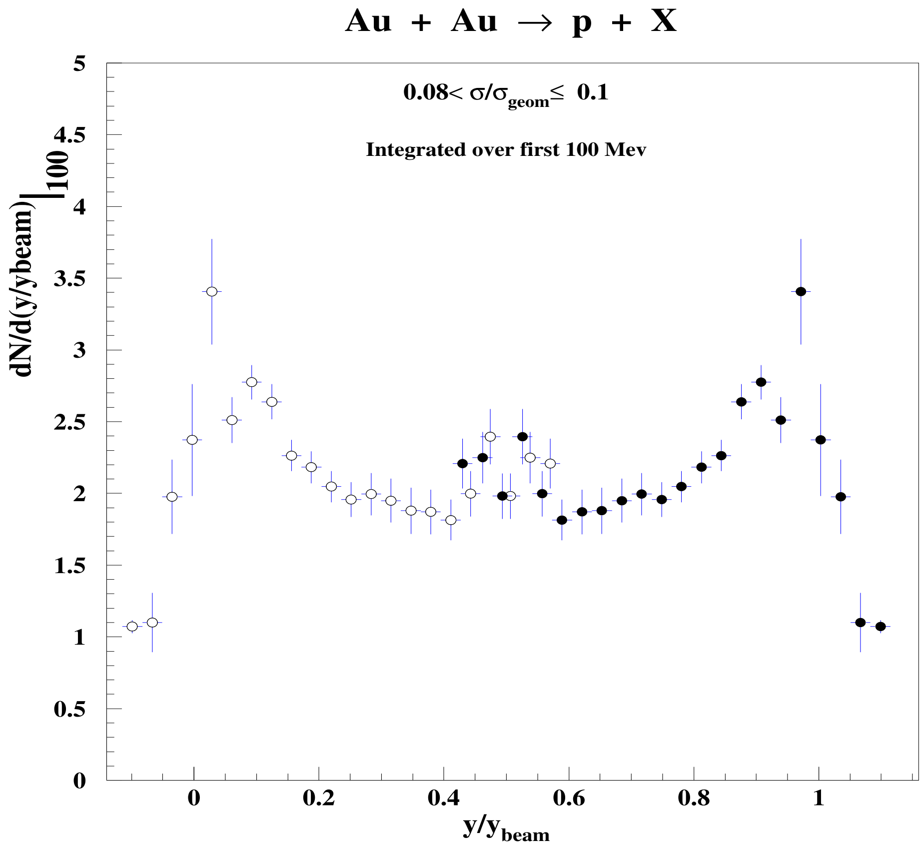

Figure C.17: Integration over the first 100 MeV/c in p_t for proton spectra , at a centrality of 10-8%, down to a rapidity of 1.4. Closed symbols are measurements, open symbols are the measurement's reflection.

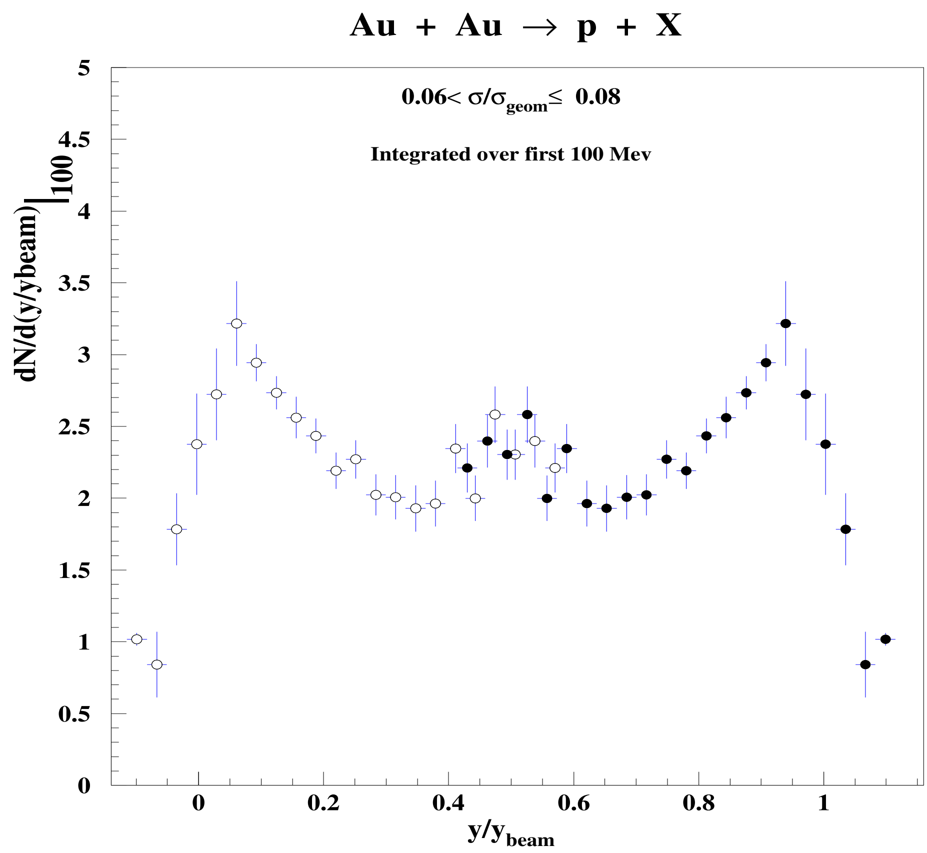

Figure C.18: Integration over the first 100 MeV/c in p_t for proton spectra , at a centrality of 8-6%, down to a rapidity of 1.4. Closed symbols are measurements, open symbols are the measurement's reflection.

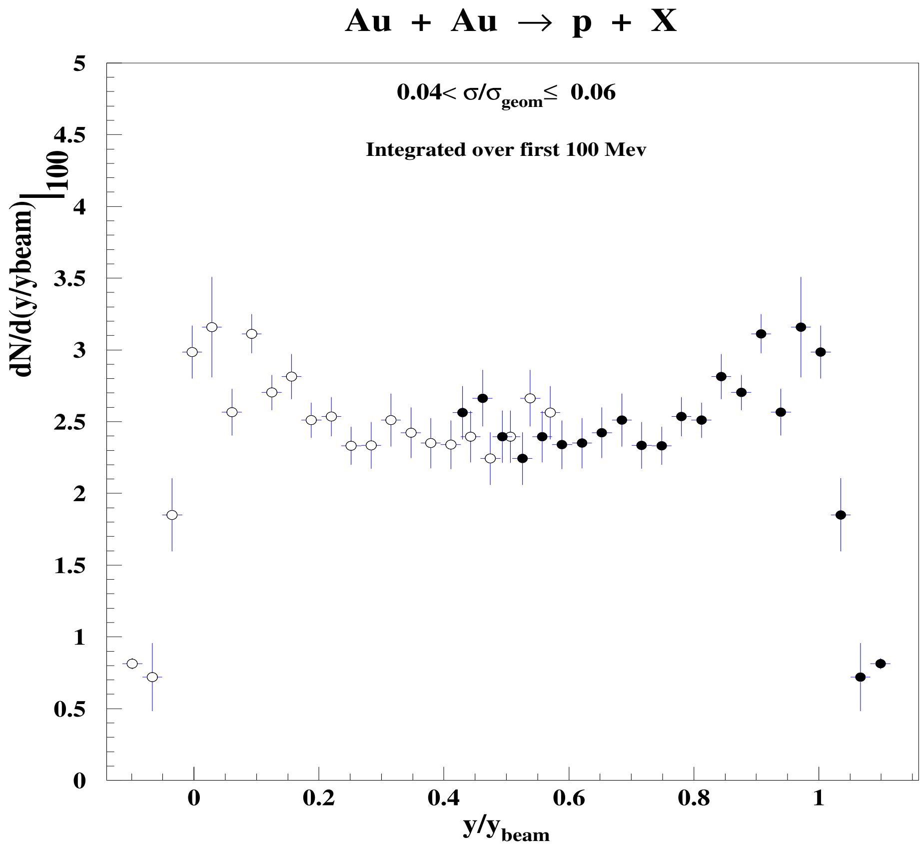

Figure C.19: Integration over the first 100 MeV/c in p_t for proton spectra , at a centrality of 6-4%, down to a rapidity of 1.4. Closed symbols are measurements, open symbols are the measurement's reflection.

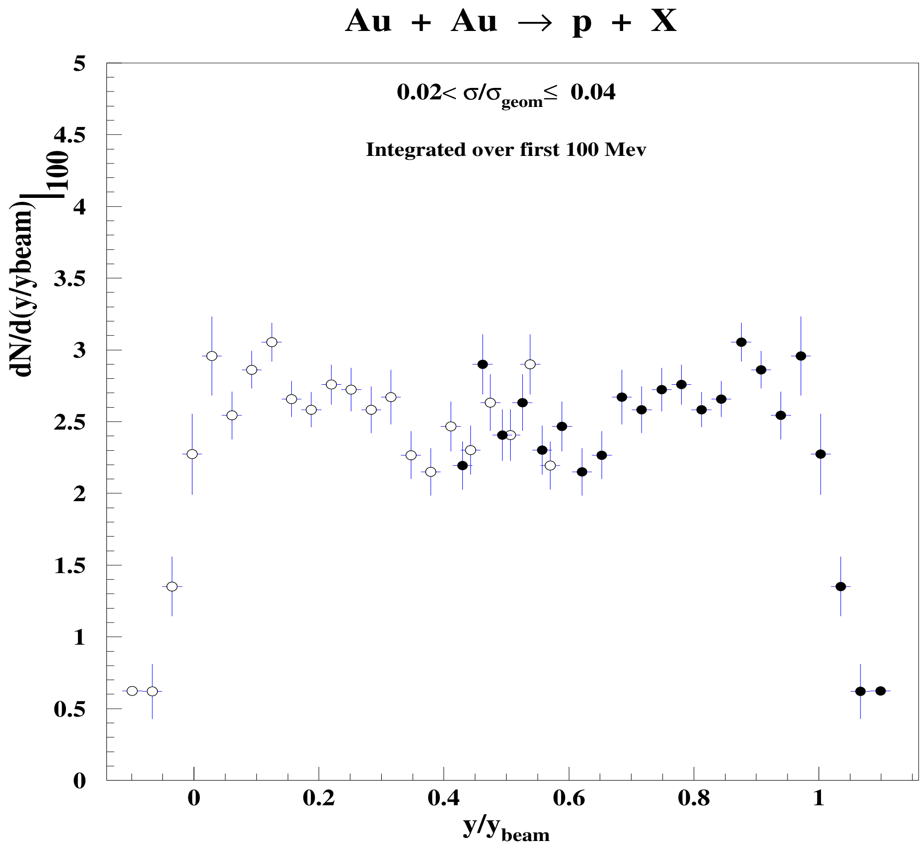

Figure C.20: Integration over the first 100 MeV/c in p_t for proton spectra , at a centrality of 6-2%, down to a rapidity of 1.4. Closed symbols are measurements, open symbols are the measurement's reflection.

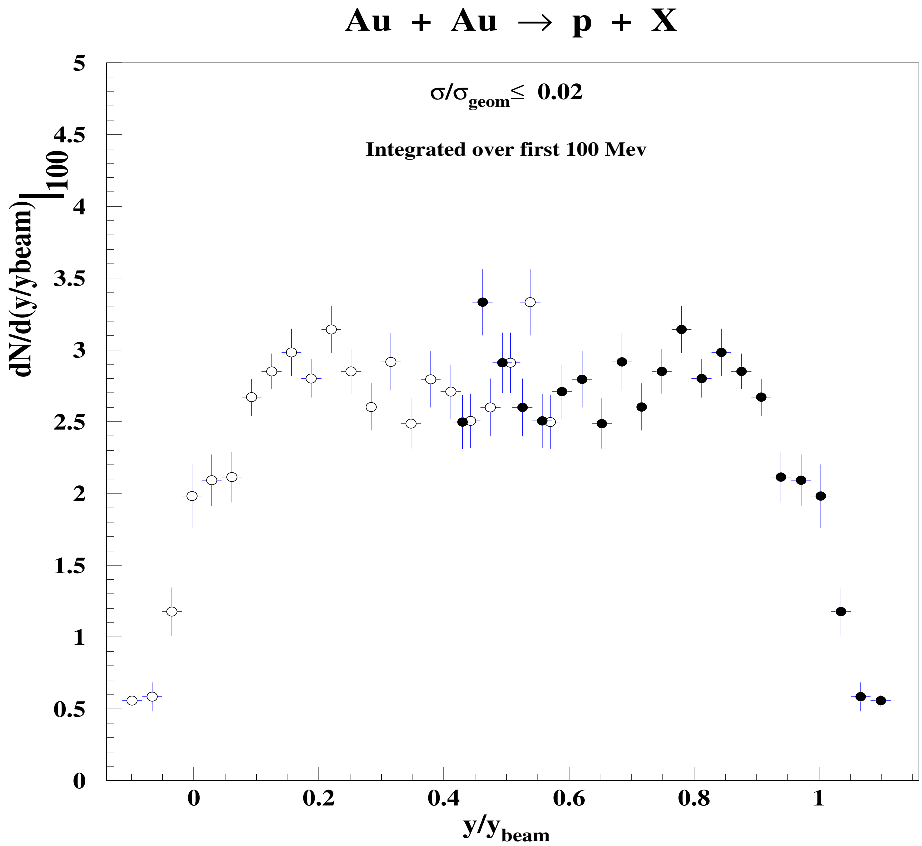

Figure C.21: Integration over the first 100 MeV/c in p_t for proton spectra , at 2% centrality, down to a rapidity of 1.4. Closed symbols are measurements, open symbols are the measurement's reflection.

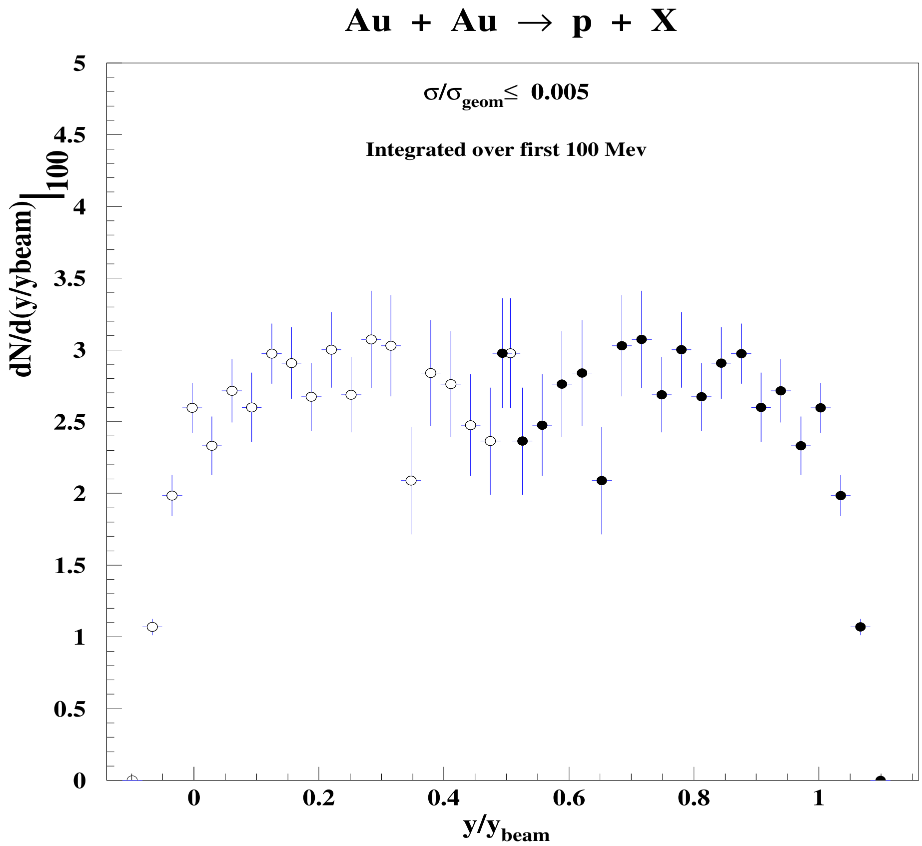

Figure C.22: Integration over the first 100 MeV/c in p_t for proton spectra , at 0.5% centrality, down to a rapidity of 1.4. Closed symbols are measurements, open symbols are the measurement's reflection.

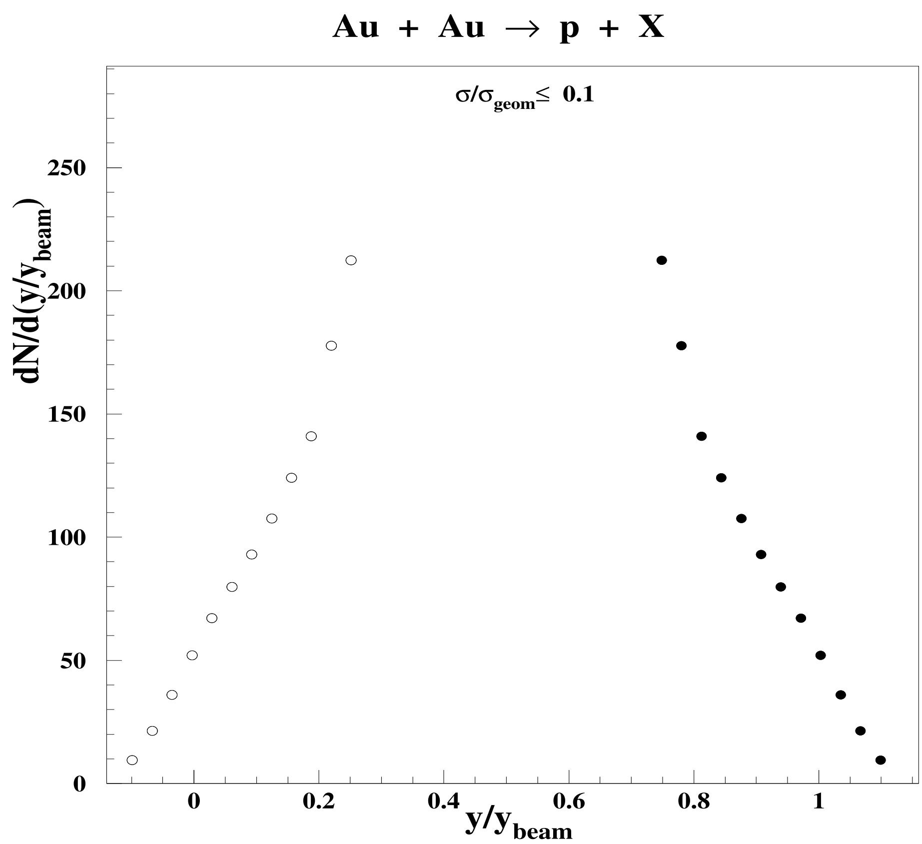

Figure C.23: Measured proton rapidity density in Au + Au collisions at 10.8 GeV/c and 10% inclusive centrality.

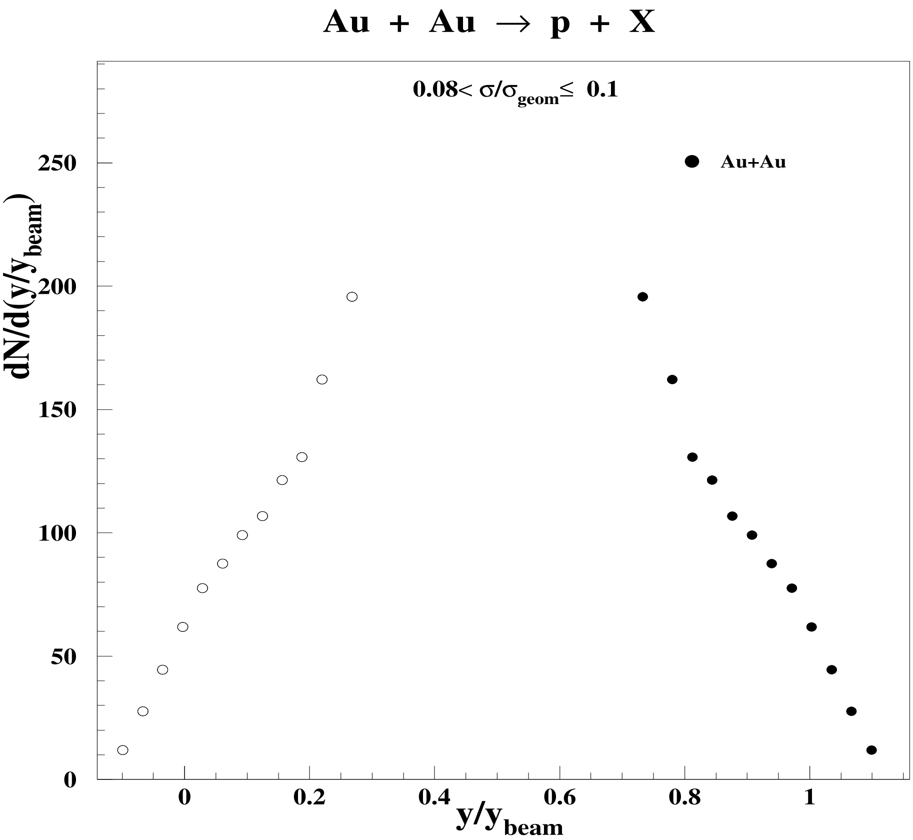

Figure C.24: Measured proton rapidity density in Au + Au collisions at 10.8 GeV/c and an exclusive centrality of 10-8%.

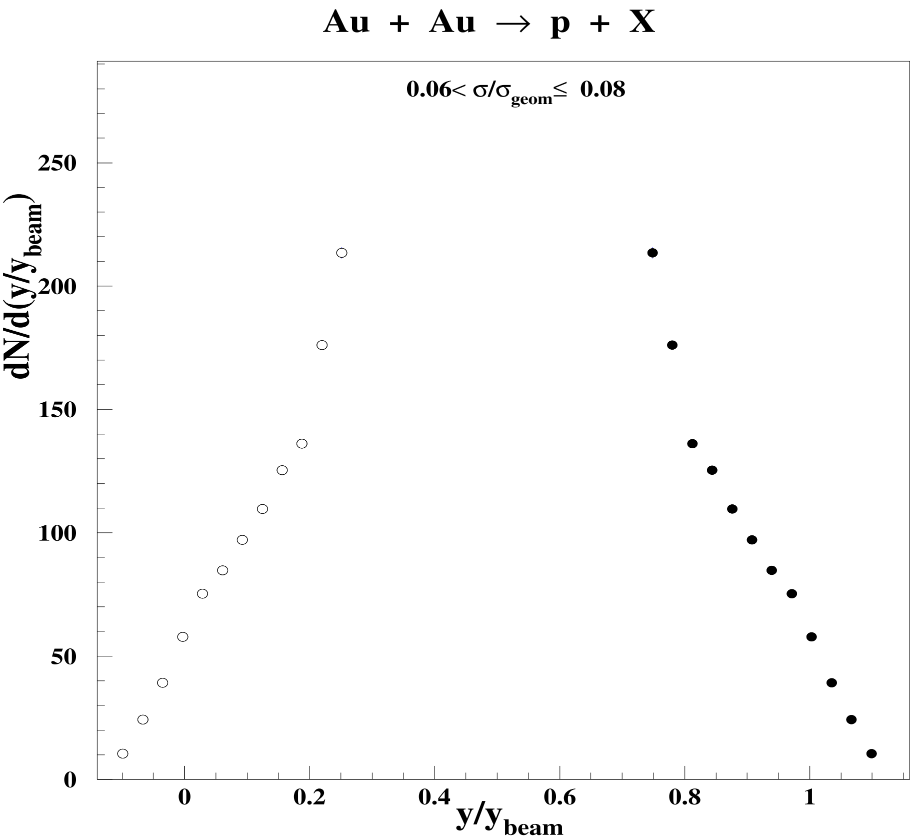

Figure C.25: Measured proton rapidity density in Au + Au collisions at 10.8 GeV/c and an exclusive centrality of 8-6%.

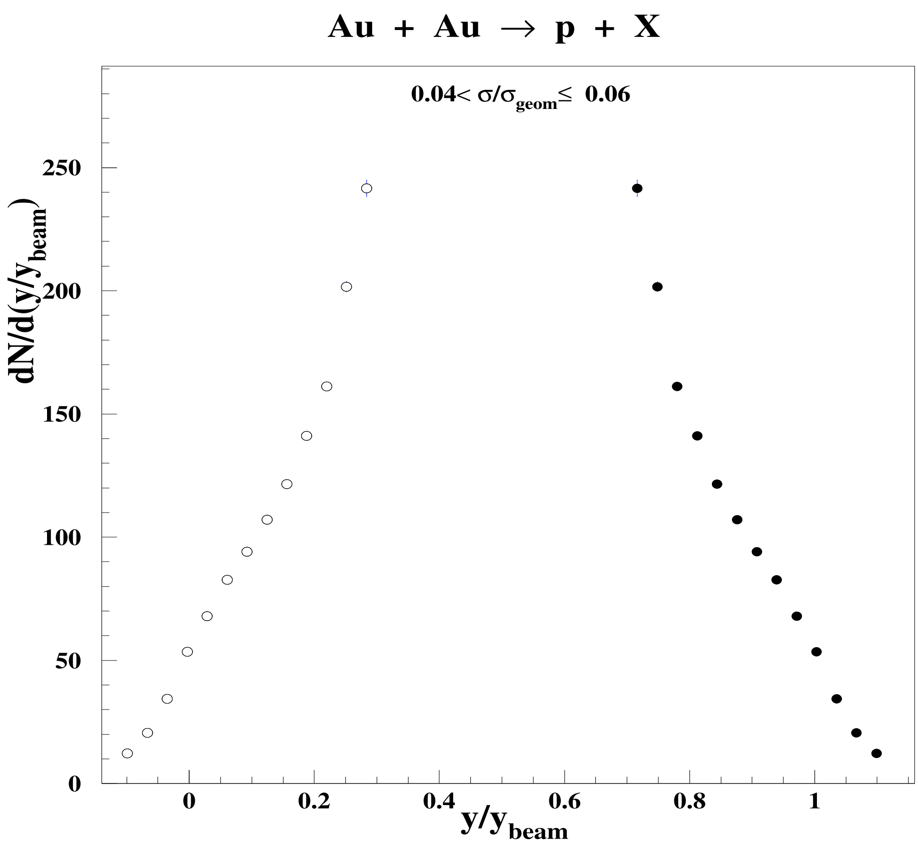

Figure C.26: Measured proton rapidity density in Au + Au collisions at 10.8 GeV/c and an exclusive centrality of 6-4%.

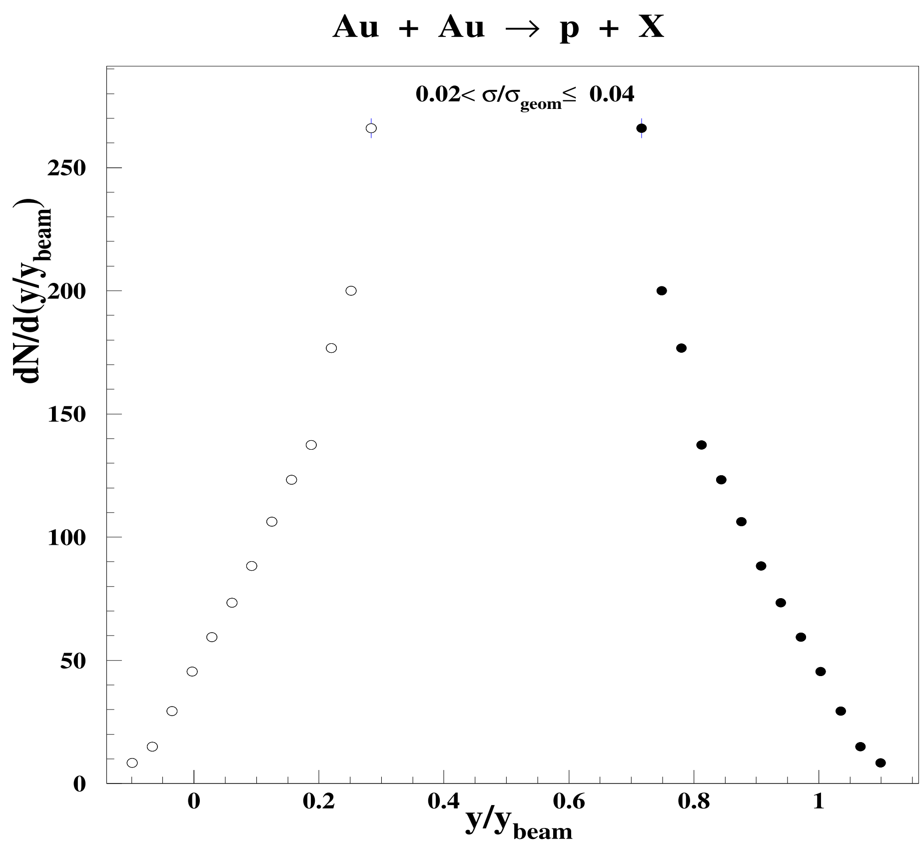

Figure C.27: Measured proton rapidity density in Au + Au collisions at 10.8 GeV/c and an exclusive centrality of 4-2%.

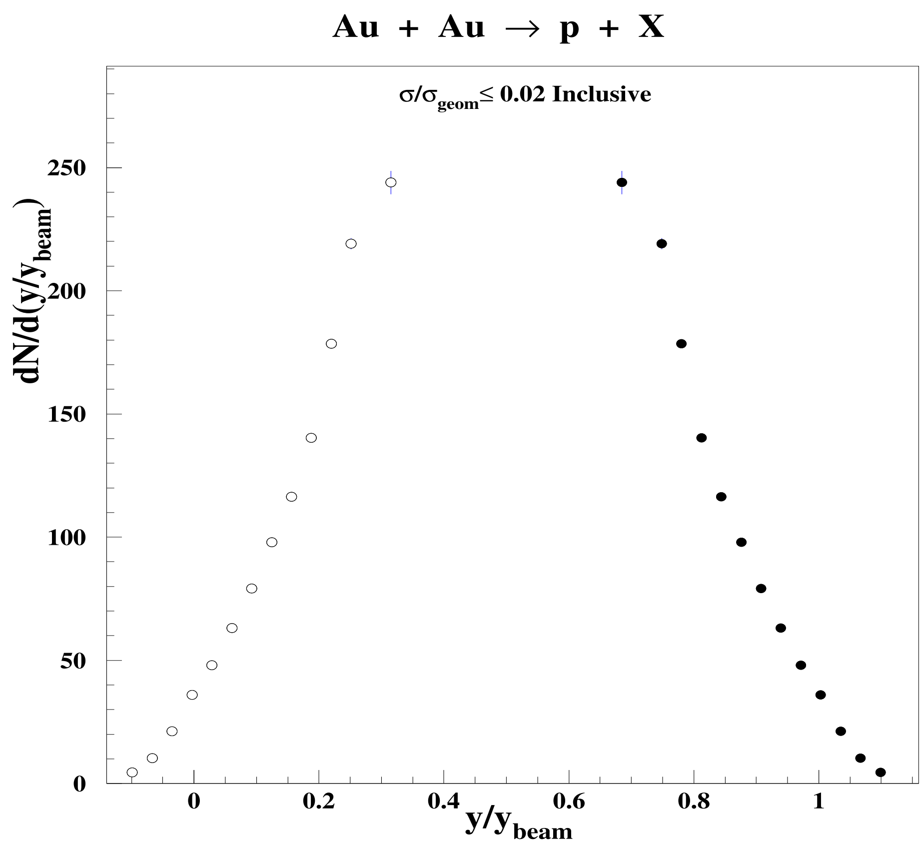

Figure C.28: Measured proton rapidity density in Au + Au collisions at 10.8 GeV/c and an inclusive centrality of 2%.

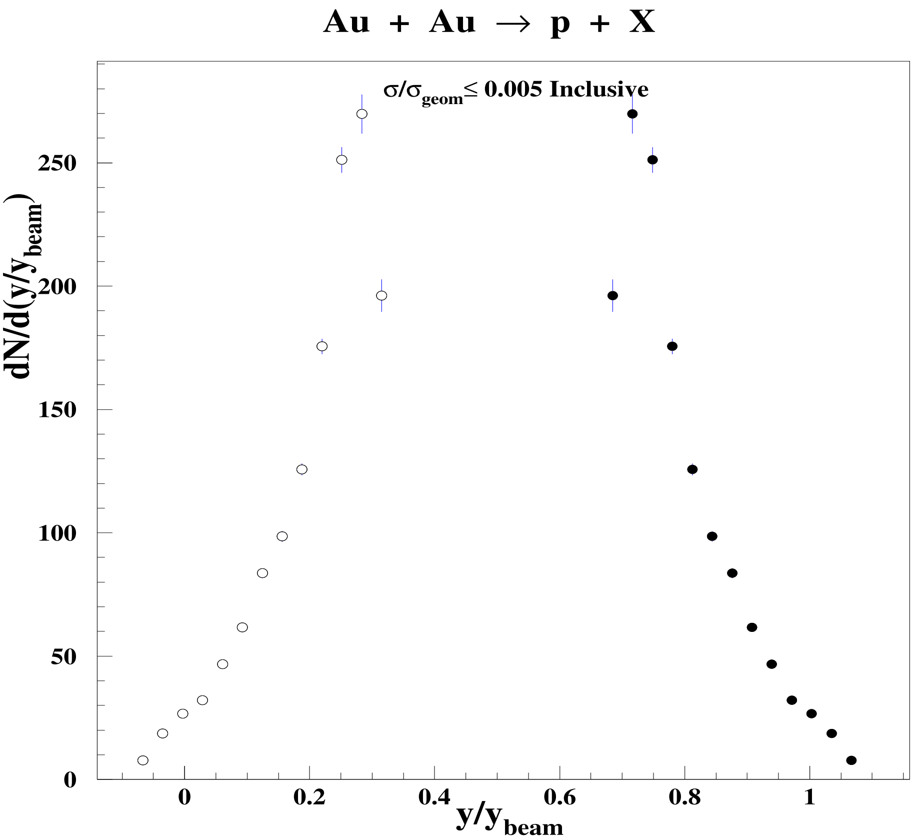

Figure C.29: Measured proton rapidity density in Au + Au collisions at 10.8 GeV/c and an inclusive centrality of 0.5%.

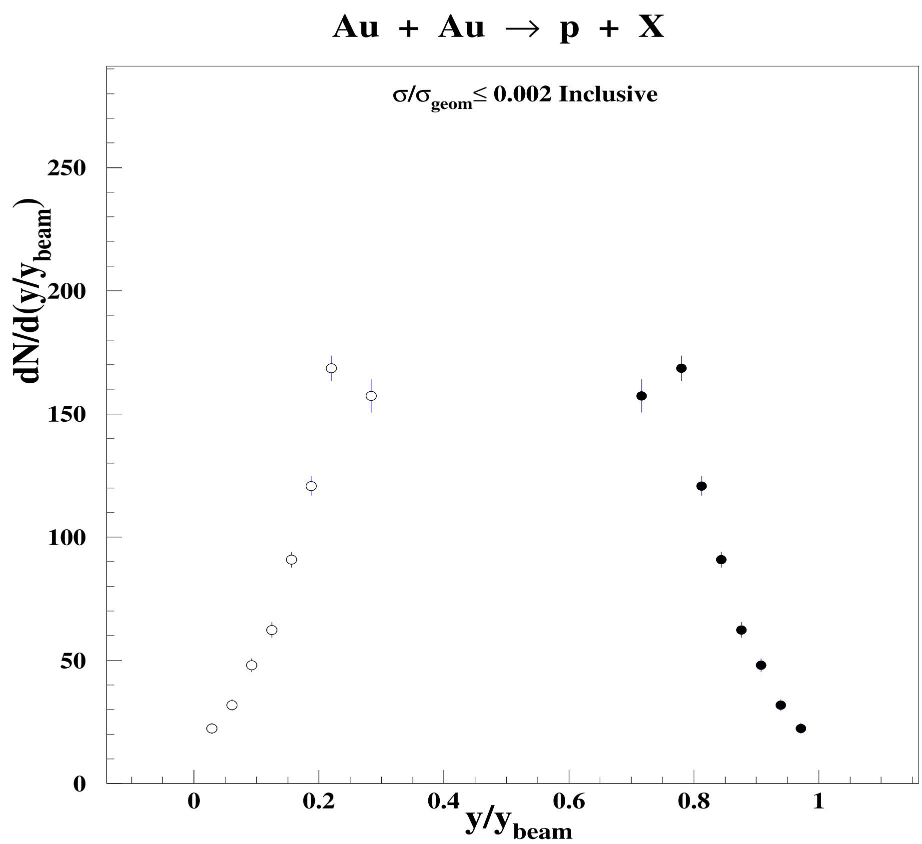

Figure C.30: Measured proton rapidity density in Au + Au collisions at 10.8 GeV/c and an inclusive centrality of 0.2%.

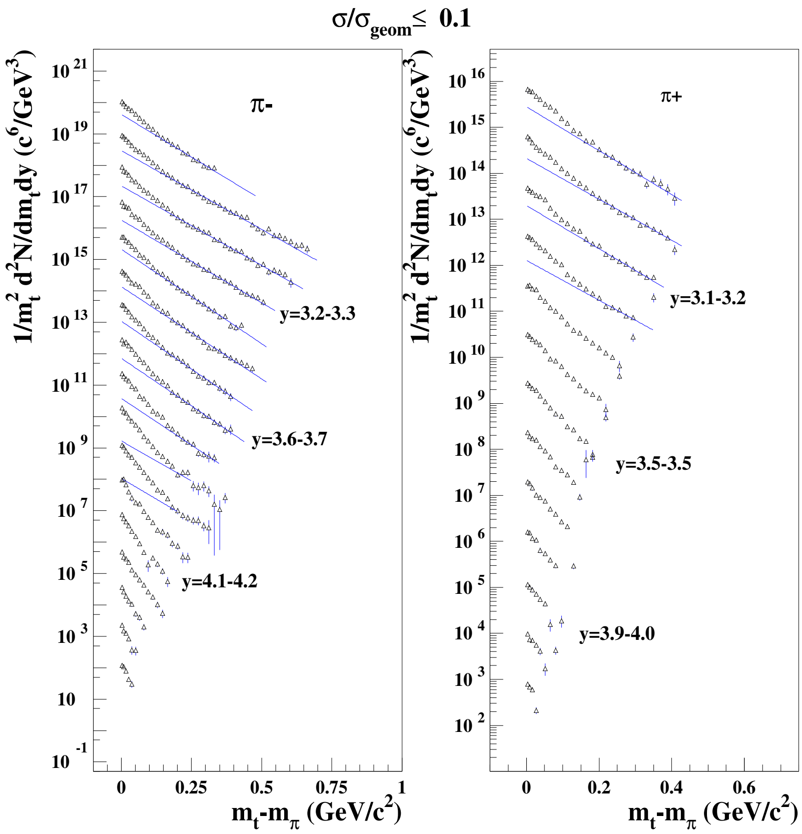

Figure C.31: Measured charged pion spectra in Au + Au collisions at 10.8 GeV/c and 10% inclusive centrality.

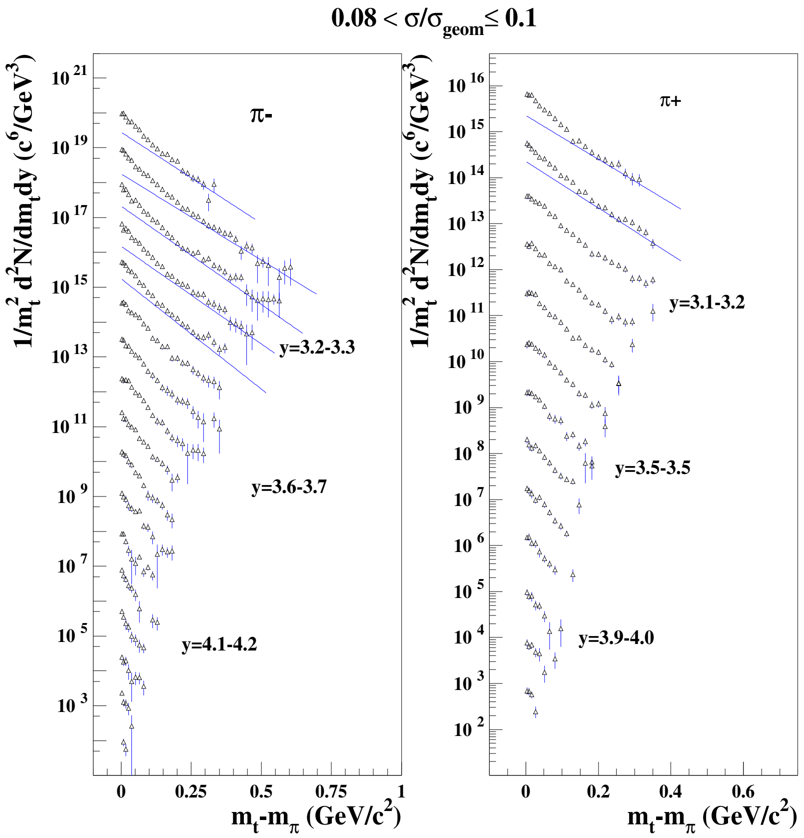

Figure C.32: Measured charged pion spectra in Au + Au collisions at 10.8 GeV/c and an exclusive centrality of 10-8%.

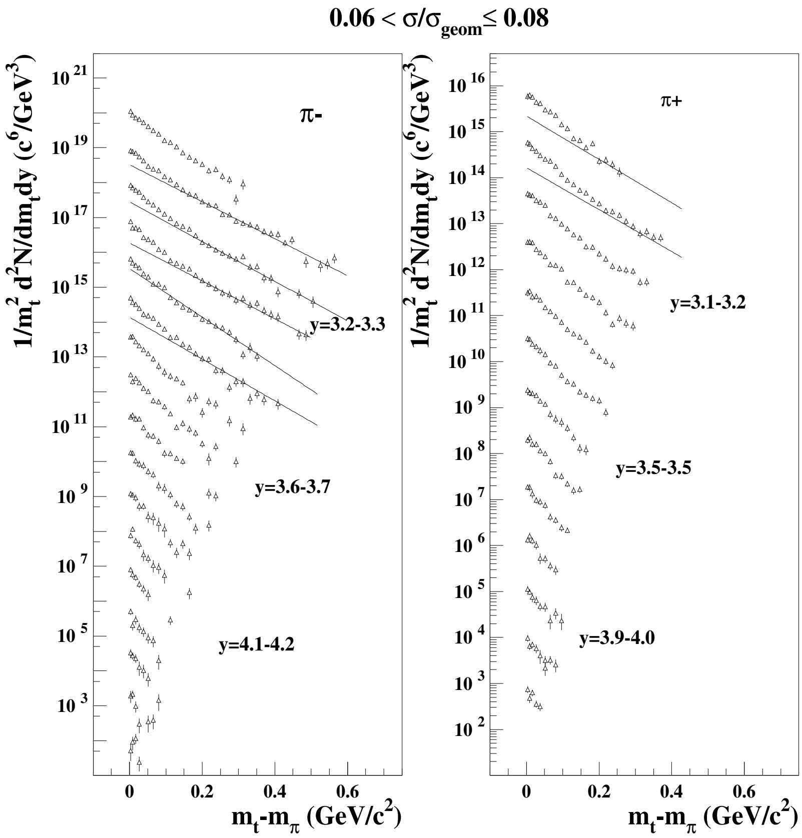

Figure C.33: Measured charged pion spectra in Au + Au collisions at 10.8 GeV/c and an exclusive centrality of 8-6%.

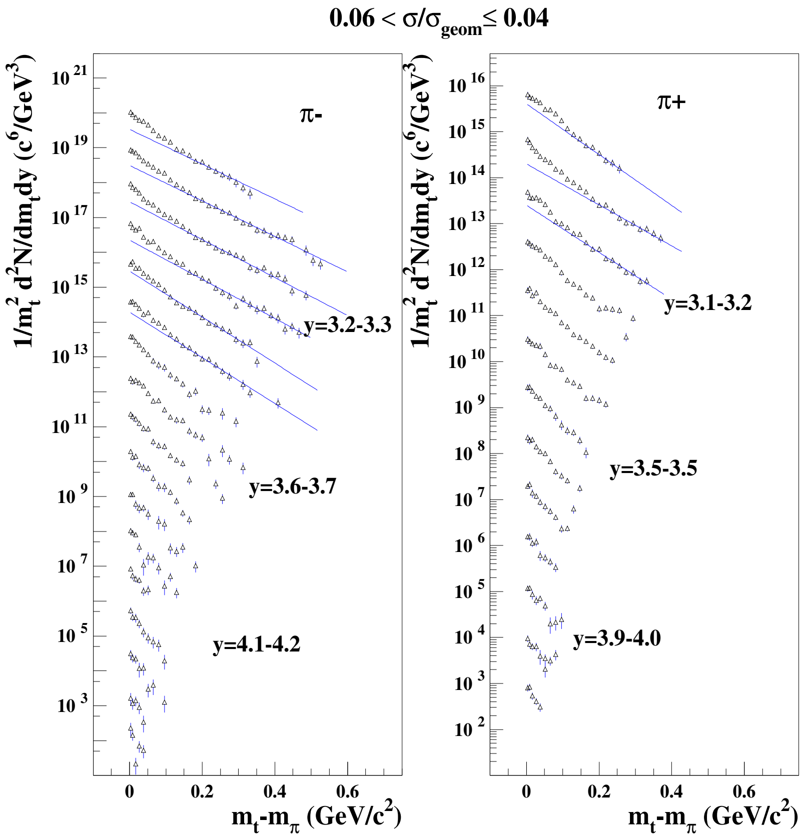

Figure C.34: Measured charged pion spectra in Au + Au collisions at 10.8 GeV/c and an exclusive centrality of 6-4%.

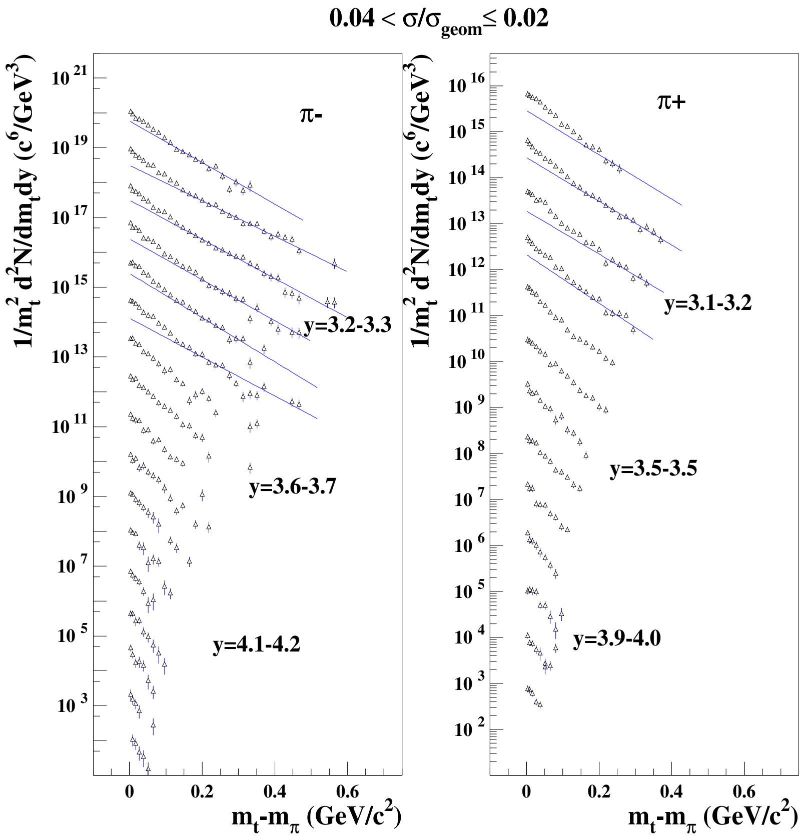

Figure C.35: Measured charged pion spectra in Au + Au collisions at 10.8 GeV/c and an exclusive centrality of 4-2%.

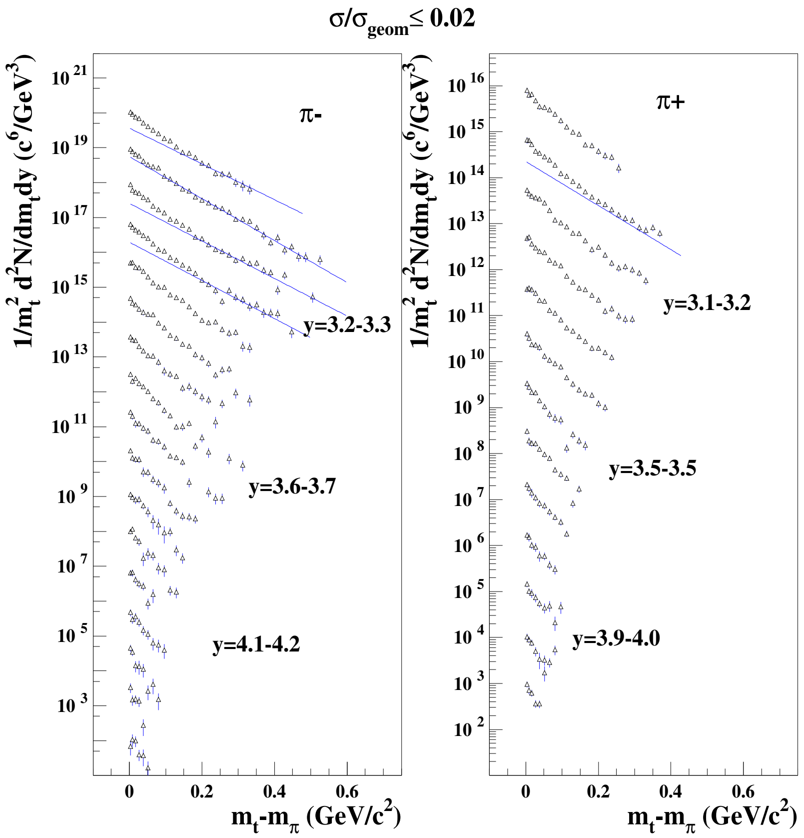

Figure C.36: Measured charged pion spectra in Au+Au collisions at 10.8 GeV/c and an inclusive centrality of 2%.